

Element-specific insights into rare-earth permanent magnets – an X-ray spectroscopy and 3D imaging approach

Der Fakultät für Physik der Universität Duisburg-Essen zur Erlangung des
akademischen Grades eines Doktors der Naturwissenschaften (Dr. rer. nat.)
vorgelegte Dissertation von

Damian Günzing
aus
Bottrop



1. Gutachter Prof. Dr. Heiko Wende
2. Gutachter Prof. Dr. Oliver Gutfleisch

Einreichung 05.10.2023
Verteidigung 08.12.2023

”Could anything at first sight seem more impractical than a body which is so small that its mass is an insignificant fraction of the mass of an atom of hydrogen? — which itself is so small that a crowd of these atoms equal in number to the population of the whole world would be too small to have been detected by any means then known to science.”

- J. J. Thompson about electrons, 1934

Acknowledgement

Throughout the different phases of experimentation, analysis, and the writing process of this thesis, I was fortunate to receive a lot of support from many remarkable individuals.

First, I would like to thank my supervisors Dr. Katharina Ollefs, Prof. Dr. Oliver Gutfleisch, and Prof. Dr. Heiko Wende, for supporting me over the recent years. They gave me the opportunity to work in a research field of high interest and high relevance for our modern society.

During this work, I had the opportunity to work with a lot of great people, measuring at many different synchrotron facilities. This is why I also thank Prof. Dr. Kristina Kvashnina for HERFD measurements at the ESRF in Grenoble. I thank Dr. Debora Motta-Meira for EXAFS measurements at the APS in Chicago. I thank Prof. Dr. Carolin Schmitz-Antoniak for the measurements at BESSY in Berlin. I want to thank Prof. Dr. Manuel Guizar-Sicairos and his team at the SLS in Villigen for the great beamline support during the ptychographic laminography measurements. For laying the groundstones in our group for this technique, I want to thank Dr. Claire Donnelly from the Max Planck Institute CPfS. I also want to thank Philipp Klassen, who did his Master's thesis with me and was helping a lot during beam time as well as analyzing the magnetic laminography data.

Special thanks go over the pond to the people at the Berkeley Lab, Dr. Alpha T. N'Diaye and Dr. Hendrik Ohldag, for the support and for giving me the great opportunity to conduct research at their excellent facility.

I want to thank all the people in the AG Wende at the University of Duisburg-Essen, who provided a lot of support and always an open ear to physical problems. A special thanks goes to Ulrich von Hörsten, whom to thank for the technical support and for providing his year-long knowledge. It was always a great pleasure to chat with you not only about physics but life and society in general. I want to express my gratitude to Christiane Leuchtenberger, our organizational wizard, for her exceptional management of travel requests, prompt handling of emergency sample deliveries, and adept equipment procurement. Moreover, her ability to provide a tranquil refuge from the daily hustle and bustle, where we can enjoy a cup of coffee, is truly appreciated.

I thank Georgia Gkouzia and Dr. Shalini Sharma for providing the RECo thin films and also for the long discussions. I want to thank Dr. Konstantin Skokov, Dr. Alex Aubert, Dr. Lukas Schäfer, and Dr. Fernando Maccari for the preparation of the Nd-Fe-B samples and additional discussions.

I want to thank for the financial support of the research framework of the DFG in the scientific framework *CRC270* by the *Deutsche Forschungsgesellschaft* and all the other Ph.D. candidates and students within the framework.

I extend my heartfelt thanks to Dr. Thomas Feggeler, Johanna Lill, Dr. Soma Salamon, Simon Rauls, Dr. Benedikt Eggert, and Dr. Alex Aubert for their valuable assistance with proofreading this thesis. Your thoughtful insights and careful feedback have significantly enriched the quality of this work.

I want to thank Dr. Irene Iglesias, Dr. Nico Rothenbach, and Dr. Samira Webers for providing emotional and sportive support, especially at the beginning of my Ph.D. journey.

Finally, my thank goes to my family, who never stopped believing in me.

Thank you!

Abstract

This thesis explores rare-earth permanent magnetic materials via synchrotron-based measurement techniques. The magnetic properties of RE–Co and Nd–Fe–B model systems are discussed. Advanced techniques used for characterization ranged from extended X-ray absorption fine structure over X-ray absorption near-edge spectroscopy and X-ray magnetic circular dichroism to X-ray imaging via magnetic ptychography.

The work demonstrates the coexistence of the SmCo_5 and $\text{Sm}_2\text{Co}_{17}$ phases in thin films stabilized by epitaxial strain energy as thin films. It shows how extended X-ray absorption fine structure analysis can be a powerful tool to quantify phases even in these complex lattices. Furthermore, it studies highly crystalline $\text{SmCo}_{5-x}\text{Cu}_x$ films grown via molecular beam epitaxy the decoupling of Sm and Co moments with increasing Cu content, using X-ray magnetic circular dichroism and X-ray excited optical luminescence detection technique. Monte Carlo simulations for sum rules give an insight into the complex behavior of the Sm magnetic dipole term $\langle T_z \rangle$.

This work also extends the knowledge of $(\text{Y}, \text{Ce})\text{Co}_5$ by X-ray absorption spectroscopy and how the electronic structure correlates to the magnetic structure using extended X-ray absorption fine structure analysis and X-ray absorption near-edge spectroscopy in the hard and soft X-ray region, as well as X-ray magnetic dichroism calculations.

This work expands the domain structure observations from the surface to the bulk, showcasing the utility of magnetic laminography in non-destructive domain studies in permanent magnetic samples. It demonstrates the reconstruction of the 3D magnetic structure in hot-deformed highly anisotropic $\text{Nd}_2\text{Fe}_{14}\text{B}$, with a spatial resolution of approximately 450 nm. Interaction domains along the c-axis exhibit a stripe-like alignment across grains, while other directions reveal intricate interconnected domains.

Kurzzusammenfassung

Diese Arbeit untersucht Dauermagnetmaterialien basierend auf seltenen Erden mithilfe von Synchrotron-basierten Messverfahren. Die magnetischen Eigenschaften der Modellsysteme RE–Co und Nd–Fe–B werden diskutiert. Fortgeschrittene Techniken zur Charakterisierung reichen von erweitertem Röntgenabsorptionsfeinstruktur über -absorption und -magnetischezirkulardichroismus bis hin zu Röntgenbildgebung mittels magnetischer Ptychographie.

Die Arbeit zeigt die Koexistenz der SmCo_5 - und $\text{Sm}_2\text{Co}_{17}$ -Phasen in dünnen Filmen, die durch epitaktische Dehnungsenergie in Dünnschichten stabilisiert sind. Sie zeigt, wie die Analyse der erweiterten Röntgenabsorptionsfeinstruktur ein leistungsstarkes Werkzeug zur Quantifizierung von diesen komplexen Phasen sein kann. Darüber hinaus untersucht sie hoch kristalline $\text{SmCo}_{5-x}\text{Cu}_x$ -Filme, die ebenfalls mittels Molekularstrahlepitaxie gewachsen sind, und die Entkopplung der Sm- und Co-Momente mit zunehmendem Cu-Gehalt unter Verwendung von Röntgenmagnetischem Zirkulardichroismus und der Technik der röntgenangeregten optischen Lumineszenzdetektion. Monte-Carlo-Simulationen für Summenregeln geben Einblick in das komplexe Verhalten des magnetischen Dipolterms $\langle T_z \rangle$ von Sm.

Diese Arbeit erweitert auch das Wissen über $(\text{Y, Ce})\text{Co}_5$ durch Röntgenabsorptionsspektroskopie und zeigt, wie die elektronische Struktur mit der magnetischen Struktur in Beziehung steht, unter Verwendung von erweiterter Röntgenabsorptionsfeinstrukturanalyse und Röntgenabsorption im weichen und harten Röntgenbereich sowie Berechnungen zum Röntgenmagnetischen Dichroismus.

Diese Arbeit erweitert ebenfalls die Beobachtungen der Domänenstruktur von der Oberfläche in den Volumen-Bereich und zeigt die Nützlichkeit der magnetischen Laminographie in nicht-destruktiven Domänenstudien an Permanentmagnetproben. Sie zeigt die Rekonstruktion der 3D-Magnetstruktur in heißverformtem, stark anisotropem $\text{Nd}_2\text{Fe}_{14}\text{B}$ mit einer räumlichen Auflösung von etwa 450 nm. Sogenannte Wechselwirkungsdomänen entlang der c-Achse zeigen eine streifenartige Ausrichtung über die Körner hinweg, während andere Richtungen komplexe miteinander verbundene Domänen offenbaren.

Contents

1. Introduction	1
1.1. Permanent magnetic materials and the clean energy transition	1
1.2. Scope and outline of the thesis	2
2. Magnetism fundamentals	5
2.1. The hysteresis loop: metrics of an excellent permanent magnet	5
2.2. Intrinsic magnetic properties	7
2.3. Extrinsic magnetic properties	10
2.4. Brown's paradox	14
3. Interaction of photons with matter and synchrotron-based methods	15
3.1. X-ray absorption near-edge spectroscopy	15
3.2. Extended X-ray absorption fine structure	17
3.3. X-ray magnetic circular dichroism	19
3.4. Magnetic laminography	22
4. Element-specific investigations of RE-Co systems	29
4.1. Sm-Co(-Cu) thin films	29
4.2. Electronic and magnetic structure of (Y, Ce)Co ₅	45
5. Interaction domains in Nd₂Fe₁₄B studied in three dimensions	51
5.1. Sample system and preparation	52
5.2. Experimental evaluation and data processing	61
5.3. 3D magnetic structure of the hot-deformed sample	65
6. Conclusion and outlook	77
6.1. Conclusion of this thesis	77
6.2. Outlook	78
Research Contributions	81
Appendices	85
A. Derivation of sum rules for 3<i>d</i> and 4<i>f</i> systems	87
B. Preparation by focussed ion beam	91
Bibliography	93
Selbständigkeitserklärung	107

1. Introduction

1.1. Permanent magnetic materials and the clean energy transition

The German word 'Energiewende'¹ describes the challenges the society will face during the following years and decades. At the center of this energy transition is the reduction of greenhouse gas emissions from fossil energy usage. Hidden between these changes towards cleaner energy production is the need for more innovative materials to drive this transition. This is especially true for permanent magnetic materials. For example, renewable energy sources such as wind need turbines. Wind turbines require about 700 kg of magnetic material per device [1]. Since wind turbines only have a limited time load during the day, generating the same power as conventional power plants (such as coal and natural gas), more wind turbines are required and, therefore, even more magnetic material.

Rare-earth/transition-metal (RE-TM) permanent magnets are technologically the most attractive magnets nowadays, with $\text{Nd}_2\text{Fe}_{14}\text{B}$ and SmCo_5 being on top of the list. These magnets combine a large energy density and high Curie temperature T_C , provided by the high TM sublattice magnetization and the high magnetocrystalline anisotropy provided by the RE.

But utilizing RE introduces downsides, too. It is crucial to acknowledge that the significance of rare-earth elements is a pressing concern, and this concern is not rooted in the perceived scarcity implied by their name. The extraction of the most rare-earth metals from the earth goes hand in hand with significant environmental impacts [2, 3]. In addition, from a geopolitical point of view, China is controlling most of the rare-earth mining and processing [4].

The research goal nowadays is to move towards permanent magnetic materials from more abundant elements [5]. However, the search for new energy materials implies a deep understanding of how permanent magnets work and which forces will lead to an efficient permanent magnet. Some parameters and characteristics are required to judge a sufficient permanent magnet material. Most fundamentally, a candidate material should have three significant properties:

1. high magnetic ordering temperature (called the *Curie temperature* T_C), below which the material is spontaneously magnetic
2. large remanent magnetization (M_r) maintained in the absence of an external magnetic field
3. strong resistance to demagnetization (expressed by *coercivity* H_C)

But how these macroscopic characteristics are fundamentally formed is still a riddle to solve. The main driver and question is how to overcome the so-called Brown's

¹german for 'energy transition'

paradox, which links the intrinsic properties (shortly described in section 2.2) to the extrinsic properties (shortly described in section 2.3). It formulates the limit of the macroscopic magnetic properties. Section 2.4 gives a summary of Brown's paradox.

1.2. Scope and outline of the thesis

It is worth noticing that the work as a Ph.D. candidate was anchored within the scientific framework CRC/TRR 270 supported by the *Deutsche Forschungsgesellschaft*. Besides the here-discussed rare-earth model systems, the framework also focuses on the exploration and development of rare-earth-free functional magnetic systems. Working in the framework allowed me to explore a diverse parameter space not only from the techniques and methods that were presented in this thesis but also from materials, ranging from Heusler compounds [6] over MAX phases [7] to magnetocaloric materials [8] and also super-conducting materials [9].

This thesis uses X-ray-based techniques to unravel the complex magnetic interplay and structures in permanent magnet materials using well-known RE-Co and Nd-Fe-B compounds as model systems for pinning and nucleation-type magnets to deepen the understanding of these well-known and tested magnets. This first chapter gives an introduction and the motivation, as well as a short overview.

Chapter 2 explains the basics of magnetism. This is done by introducing the fundamentals of magnetism and giving literature references for further reading for everything that can not be covered. This chapter starts with section 2.1 about the magnetic hysteresis loop and its importance as a figure of merit for permanent magnets. The following sections focus on the underlying mechanisms involved in magnetic hysteresis: intrinsic and extrinsic magnetic properties. The last section of the chapter explains Brown's paradox, which describes the discrepancy in the interplay of intrinsic and extrinsic magnetic properties.

Chapter 3 introduces most of the techniques used in this thesis. All main techniques are synchrotron-based methods. With the consideration of X-rays' interaction with matter and magnetic matter, these methods will be described. It starts with a section about X-ray absorption near-edge spectroscopy (XANES or XAS). In the following section, extended X-ray absorption fine structure (EXAFS), which gives the local ordering in an element-specific matter, will be explained. In the next section, circular polarization will be added to the previously discussed technique, which leads to the effect of X-ray magnetic circular dichroism (XMCD), which will be utilized as a spectroscopy technique. This technique unravels, element-specifically, the orbital and spin contributions to the total magnetic moment per atom. The last section of the methods chapter introduces magnetic laminography, which is a novel ptychography-based technique utilizing the XMCD effect.

The results chapter 4 evaluates RE-Co systems as thin films and bulk materials. This chapter utilizes EXAFS, XANES, and XMCD to unravel the crystallographic, electronic, and magnetic properties of SmCo_5 and $(\text{Y}, \text{Ce})\text{Co}_5$ compounds as magnetic thin films. Bulk materials are explored for $(\text{Y}, \text{Ce})\text{Co}_5$ as well.

Chapter 5 describes the analysis of a high-textured Nd-Fe-B sample. In these samples, so-called interaction domains are crucial: magnetic domains larger than the underlying crystallographic grain structure. This chapter discusses the macroscopic behavior of multiple similar samples for comparison. The main focus of this chapter lies in the analysis of the 3D magnetic structure of a high-textured sample, explored

by magnetic X-ray laminography, a novel technique to unravel the 3D magnetic structure in a non-destructive way.

The last chapter 6 summarizes the work and provides an outlook on how the work could proceed in the upcoming years.

2. Magnetism fundamentals

Magnetism was first discovered in ancient times when people observed the intriguing attraction between naturally occurring lodestones [10]. These early encounters with the magnetic force marked the inception of humanity's fascination with this phenomenon. In the Middle Ages, magnetic compasses revolutionized navigation. Later, in the 16th century, pivotal contributions of individuals like William Gilbert laid the foundation for our scientific understanding of magnetism. In the 19th century, Hans Christian Oersted revealed the profound link between electricity and magnetism; exploring this mysterious force has woven a tapestry of curiosity, experimentation, and innovation.

This chapter summarizes the modern understanding of the fundamentals of magnetism with a focus on permanent magnetic materials and methods used in this thesis. The chapter is kept short on purpose. As we follow along the sections, more literature for further reading and understanding will be introduced. The first section 2.1 covers the metrics and the critical measurement of permanent materials. In the following sections, the intrinsic (see section 2.2) and extrinsic (see section 2.3) magnetic properties will be explained. Understanding its differences and interplay is essential for the scope of this thesis. With the X-ray-based measurement techniques used in this work, both properties can be probed and measured.

2.1. The hysteresis loop: metrics of an excellent permanent magnet

From a fundamental standpoint, a good permanent magnet must have a high magnetic stray field that does not degrade at ambient magnetic fields or elevated temperatures over time. Additionally, a desired appeal should be low-cost and corrosion-resistant in ambient conditions. The measured 'hysteresis loop' of the permanent (ferro-)magnet at a fixed temperature is crucial to gain information about magnetization and resilience in magnetic fields. This measurement shows the magnetic reversal of the measured (permanent) magnetic material. Hysteresis loops are one of the most common measurements in magnetic research. The measurement works as follows: during the change of the applied magnetic field, the (macroscopic) magnetic moment of the sample is recorded. This is usually performed loop-like: one starts at a positive or negative maximum field of the measurement, ramps up or down to the desired opposite field value, and loops back to the starting point. To record the first magnetization curve, the magnetic moment is additionally recorded during the ramp-up from 0 T to the maximum field.

In figure 2.1, a schematic hysteresis loop is shown¹. On the x-axis, the external applied magnetic field is depicted. On the y-axis, the resulting sample magnetization

¹python code snippet to recreate figure (free, public domain): <https://gist.github.com/gnzng/f5aba0fd146a429b30311d8e0f047333>

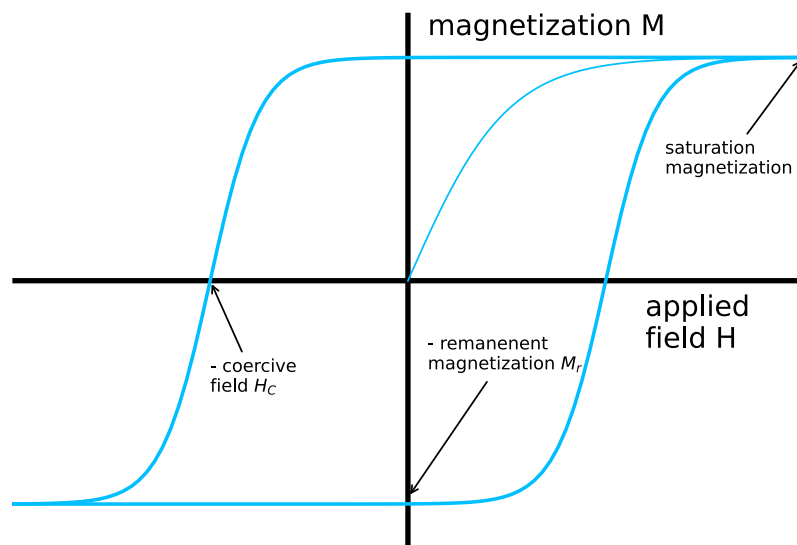


Figure 2.1.: The thin blue line starting at the point of origin depicts the first magnetization curve, while the thicker blue line depicts a whole loop.

is shown. Increasing the externally applied field to values greater than zero will magnetize the sample. At a given applied magnetic field, the sample's magnetization no longer changes; the measured material is magnetically saturated. The thin blue line starting at the point of origin depicts this initial magnetization curve. The initial magnetization curve already indicates the underlying magnetic structure and magnetization mechanisms, which you can find more about in section 2.3. In this process on the microscopic scale, the magnetic moments in the individual magnetic domains align from totally random (starting point) to all aligned (saturated state). If the externally applied magnetic field is decreased again, the measured specimen remains magnetized even at zero applied fields. The remaining magnetization M_r is called remanent magnetization or remanence, and the sample's magnetization vanishes at the coercive field H_C .

In general, ferromagnetism and the existence of a hysteresis loop are induced by smaller regions. These so-called magnetic domains can expand or shrink in size depending on the direction of the applied field. In a magnetic domain, all atomistic spins point in almost the same direction and have nearly the same magnitude. Magnetic domains are separated by regions of changing magnetization, so-called domain walls, which are much thinner than the magnetic domains in permanent magnetic materials due to the high anisotropy of the magnetic material. The volumetric change of these domains will influence the overall macroscopic magnetic appearance of the sample material. However, how this characteristic hysteresis forms and develops in detail is a complex interplay between the intrinsic and extrinsic properties, which will be covered and explained in more detail in the next sections.

The figures of merit of the hysteresis curves can be combined in a scalar, the maximum energy product $(BH)_{\max}$, which is defined as the maximum area of a rectangle below the hysteresis curve in the second quadrant given by equation (2.1).

$$(BH)_{\max} \equiv \max(-B \cdot H) \quad (2.1)$$

The largest rectangle fitting below the hysteresis curve is shown in figure 2.2. Physically, it represents the maximum energy stored per unit volume of the magnetic material. It quantifies how much magnetic energy can be stored in a given amount of a magnetic material.

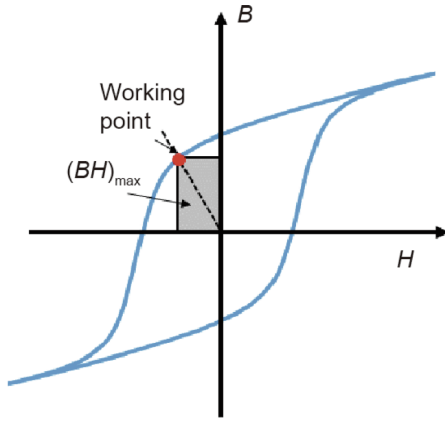


Figure 2.2: The shaded rectangle highlights the maximum energy product $(BH)_{\max}$. Adapted from reference [11]

An excellent permanent magnet is considered to keep its magnetization until ca. 600 K (Curie temperature T_C) and has a $(BH)_{\max}$ beyond ca. 260 kJ/m³ [12].

2.2. Intrinsic magnetic properties

The concept of intrinsic magnetic properties is essential for understanding magnetic hysteresis phenomena. Usually, intrinsic magnetic properties are referred to as the phenomena evolving from the electronic and atomic origin of the material, being directly correlated to the following properties: Curie temperature T_C , saturation magnetization M_S , and the anisotropy field H_A . The Curie temperature T_C is the temperature at which a material undergoes a phase transition from a ferromagnetic or ferrimagnetic state to a magnetically unordered state. The saturation magnetization represents the point at which the domains of the magnetic material are fully aligned in the direction of the external field. The anisotropy field H_A is the external magnetic field required to overcome the preferred alignment (in permanent magnets along a uniaxial easy axis) and induce a significant change in the magnetization direction.

The intrinsic properties are strongly dependent on the crystal structure and elements. This section will focus on the electrons' spin- and orbital magnetic moments, their coupling, and magnetocrystalline anisotropy. It will concentrate on electrons because they contribute most to an atom or ion's net magnetic moment due to their significant intrinsic magnetic moment. A good overview and a more detailed discussion about all intrinsic magnetic properties can be found in the following textbooks indicated by references [12–14].

Orbital and spin magnetic moment and spin-orbit coupling

One of the most important intrinsic properties is the atom's magnetic moment. The magnetic moment consists of the spin and orbital magnetic moments, which add up to the total magnetic moment. The atoms' magnetic moment is almost completely composed of the electrons' magnetic moments [12, 15].

In this thesis, X-ray magnetic circular dichroism (XMCD) is used as an element-specific and non-destructive measurement technique, which gives information on the magnetic moment per atom and can further separate spin and orbital magnetic contributions. See the section 3.3 for an explanation of the XMCD effect and the results in chapters 4 and 5 for the utilization of this effect within the framework of this thesis to study real-world permanent magnetic materials.

Orbital moment

The orbital moment of an atom can be understood and interpreted in a classical picture as a moment arising from the electrons' circular motion around a Coulomb potential of the atom nucleus. We can describe the orbital magnetic moment μ_L as follows as an angular momentum:

$$\vec{\mu}_L = -\frac{g_L \mu_B}{\hbar} \vec{L}, \quad (2.2)$$

where \vec{L} is the orbital momentum vector, the orbital g-factor g_L is exactly one and $\mu_B = \frac{e\hbar}{2m_e}$ being the Bohr magneton. \hbar is the reduced Planck constant.

Spin moment

In a simple picture, the magnetic spin moment can be understood as the intrinsic angular momentum of an electron or particle. The spin magnetic moment of electrons can be calculated and expressed as follows:

$$\vec{\mu}_S = \frac{g_S \mu_B}{\hbar} \vec{S}, \quad (2.3)$$

where \vec{S} is the spin moment vector, and g_S is a dimensionless number called the spin g-factor with a value of approximately 2.00232 for electrons [16].

In transition metals (TM), the spin moment is usually much larger and provides a more significant amount to the total magnetic moment. Even in a free $3d$ state ion, the angular momentum is quenched due to rotational symmetry. The orbital moments of RE $4f$ systems are relatively robust and less affected by electron-electron interactions and crystal field effects compared to $3d$ systems.

Spin-orbit coupling

Spin-orbit coupling (or spin-orbit interaction, spin-orbit effect) describes the phenomenon in quantum mechanics where the previously discussed spin of a particle is coupled with its orbital moment. In a simple picture, one can understand that spin represents a particle's intrinsic angular momentum, and orbital motion represents its path moving around a central electric charge (the atomic core). This interaction

leads to splitting the initial energy level into two levels. The study of this splitting and, therefore, the coupling becomes essential when looking at atoms and molecules, as it is known to influence the magnetic and electronic properties significantly.

There are two commonly used systems for describing the coupling of the orbital angular momentum (L) and the spin angular momentum (S) of an atom or ion called LS coupling and JJ coupling. The assumption in LS coupling is that the coupling of L and S is much stronger than the coupling of single electrons in the described system. In this case, an atom or ion's total angular momentum (J) is obtained by vectorially adding L and S. It is a convention to use lowercase letters for single electrons and capital letters for multiple electron systems like atoms or ions. In a simple picture in multiple electron systems, two ways are possible for the summation of all the moments:

$$\vec{J} = \sum_i^N \vec{\ell}_i + \sum_i^N \vec{s}_i. \quad (2.4)$$

Describing magnetic systems by JJ coupling assumes that the coupling of individual electrons is stronger than the coupling between the individual L and S. In this case, J of an atom or ion is calculated by vectorially adding the angular momenta of each electron:

$$\vec{J} = \sum_i^N \vec{j}_i = \sum_i^N (\vec{\ell}_i + \vec{s}_i). \quad (2.5)$$

Based on electronic structure calculations, spin-orbit interaction has the most significant influence on magnetocrystalline anisotropy. Van Vleck was the first to propose that magnetocrystalline anisotropy arises from spin-orbit interaction coupling the isotropic spins to the crystal lattice [17]. Bruno showed that the discussed orbital moment dramatically contributes to the magnetocrystalline anisotropy [18] and, therefore, to the anisotropy field H_A , which defines a hypothetical field, where all moments would be aligned along the hard axis. Magnetocrystalline anisotropy will be explained in the following paragraphs.

Magnetocrystalline anisotropy

In general, magnetocrystalline anisotropy describes phenomena in which a crystalline bulk magnetic material requires different amounts of energy (applied through an external magnetic field) to magnetize the sample in different directions. This behavior is purely attributed to the crystal structure being strongly coupled to the spin-orbit interaction described in the previous paragraph.

The intrinsic property of the high magnetic anisotropy can generally lead to the macroscopic behavior of high coercive fields [19]. The RE elements are alloyed for their anisotropic behavior in TM-RE permanent magnets. The 4f electron distribution possibility is usually not spherical in RE systems. The asymmetric electron clouds interact with the electrostatic field of the environment. This pins the anisotropic one-atom magnetic moment to the surrounding lattice and gives the overall magnetic moment a strong preferred orientation in some RE elements [20–22].

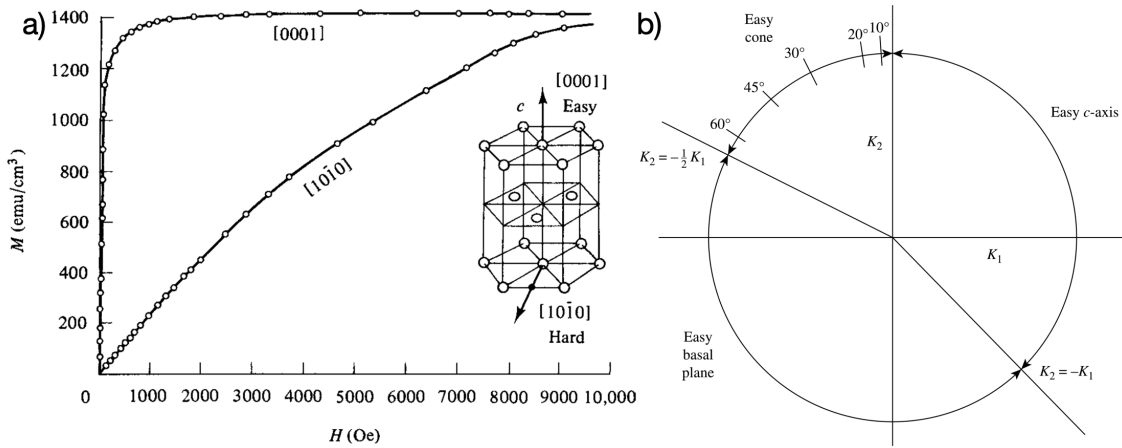


Figure 2.3.: Schematic figure of a) the magnetization behavior along the easy and hard magnetic axis with increasing applied field and b) different preferred easy axis or plane orientation for different anisotropy constants K_1 and K_2 . Figures a) and b) from reference [23].

Magnetocrystalline anisotropy in hexagonal systems will now be discussed. This includes the permanent magnetic systems like 1:5 (e.g., SmCo_5). $\text{Nd}_2\text{Fe}_{14}\text{B}$ is rhombohedral with a K_1 of 4.3 MJ/m^3 and K_2 of 0.65 MJ/m^3 at room temperature. An anisotropy constant of $K_1 = 17 \text{ MJ/m}^3$ for SmCo_5 [24].

Including all contributions up to the third term, the anisotropy energy per unit volume in a sixfold symmetry can be written as:

$$E/V = K_1 \sin^2 \theta + K_2 \sin^4 \theta + K_3 \sin^6 \theta \cos 6\phi, \quad (2.6)$$

with θ being the polar angle and ϕ the azimuthal angle. K_i are the anisotropy constants. The requirement for a permanent magnet is that the only preferred magnetic axis is the easy axis. The magnetization for such a magnetic material is depicted in figure 2.3 a). This sets the condition for $K_1 > 0$ and $K_2 > -K_1$. Then, the easy axis lies within the axis of the highest symmetry. For all other values for K_1 and K_2 , only basal plane or easy cone anisotropy will be achieved (see figure 2.3 b)).

As an overview over the intrinsic properties SmCo_5 and $\text{Nd}_2\text{Fe}_{14}\text{B}$, we find a Curie temperature of 1003 K and 586 K, saturation magnetization of 1.23 T and 1.6 T, an anisotropy field of 40 T and 6.7 to 8 T [5, 12, 24, 25].

2.3. Extrinsic magnetic properties

Extrinsic properties mostly dominate the shape of the hysteresis curve. It is therefore considered a 'micromagnetic phenomenon'. This term is also a little misleading since the critical phenomena mostly play roles on nano-structural length scales [13]. Since all intrinsic magnetic properties discussed in the previous section 2.2 influence the structure locally, they also affect the hysteresis curve's overall shape and the extrinsic magnetic properties. The extrinsic properties include the remanence M_r and the coercive field H_C . The remanence or remanent magnetization M_r is the magnetization or field remaining after the external applied field was removed. The

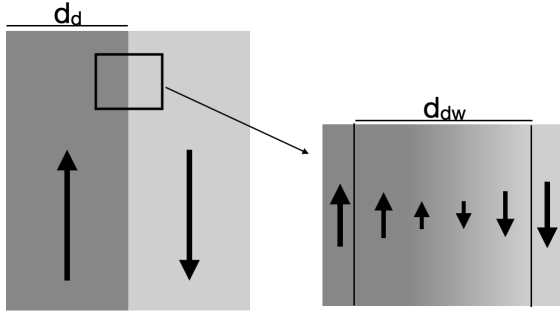


Figure 2.4: Schematic of a domain and a domain wall, with domain width d_d and domain wall width d_{dw}

coercive field H_C is the field at which the samples' magnetic moment vanishes upon the magnetization reversal process (both properties are also indicated in figure 2.1).

Magnetic domains and domain walls

For very small ferro- or ferrimagnetic particles (e.g., nanoparticles below the single-domain threshold), the Stoner-Wohlfarth assumption is true that the magnetization is roughly uniform through the whole magnet. If the particle is larger than a certain threshold (the mentioned single-domain threshold), the larger domain will divide into multiple smaller domains to reduce the overall magnetostatic energy [15]. A simple schematic of the domains of a ferromagnet is depicted in figure 2.4, with the characteristic domain width d_d and domain wall width d_{dw} , which is determined by balancing exchange energy and magnetic anisotropy.

Figure 2.5 depicts two common domain walls. Figure a) shows a Bloch wall, and figure b) a Néel wall. In the Bloch wall, the magnetization gradually rotates as you move across the wall. This rotation typically occurs in a spiral pattern, with the magnetization changing direction smoothly from one domain to another. The magnetization direction in the Néel wall flips in the moving direction by 180° as you cross the wall.

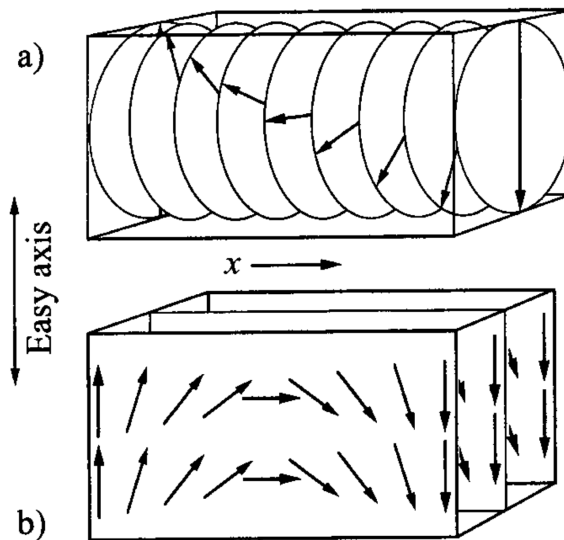


Figure 2.5: Two different domain walls: (a) Bloch wall or (b) a Néel wall in a planar film where the magnetization in the domain is parallel to the film plane. From reference [26].

The width of a magnetic domain wall can be estimated via:

$$d_{dw} \approx \pi \sqrt{\frac{A}{K}}, \quad (2.7)$$

where A is the exchange stiffness and K the most influential anisotropy constant. Please notice that A is proportional to the exchange integral J_{ex} , which describes the quantum mechanical effect between identical particles. More about domain patterns and their calculation can be found in the references [12, 27, 28].

Nucleation and pinning: magnetic reversal mechanisms

In this section, we introduce two main causes of magnetic reversal mechanisms. Hysteresis only exists if the magnet is held in a metastable state. Every real magnetic material is non-homogenous, leading to chances of locking or vanishing these meta-stable states. This gives rise to small nucleation (or pinning) points, which act as domain walls' starting (or decelerating) points during magnetic reversal mechanisms. So-called pinning centers hinder the domain wall motion during the magnetic reversal and pin the magnetic domains in the given state. The nucleation process is depicted in figure 2.6 a) as well as the pinning process.

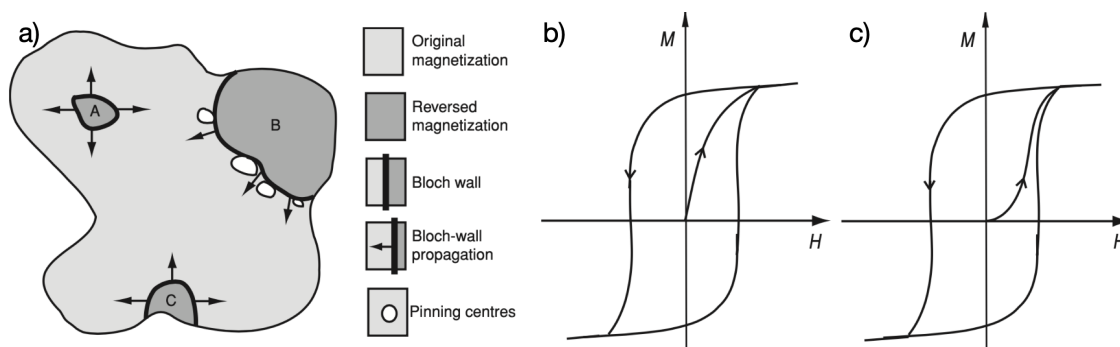


Figure 2.6.: Schematic of a) magnetic reversal mechanism, hysteresis loops, and first magnetization curves for either b) nucleation or c) pinning type magnetic material and reversal behavior. Adapted from [12].

During the initial magnetization curve in a magnetometry measurement, it is possible to observe which effect, either nucleation or pinning, exerts a dominant influence. In figure 2.6 b), the dominating nucleation mechanism is schematically shown during the first magnetization curve, and in figure 2.6 c), the dominating pinning process is shown. During the first magnetization with a dominating nucleation mechanism, the magnetization of the specimen increases relatively rapidly since a dominating amount of nucleation centers will give rise to a high amount of domain wall motion with a smaller amount of energy applied through the external magnetic field H . The opposite is observed within the dominating pinning contribution. More energy must be used via the externally applied magnetic field H to increase the domain wall motion, leading to the magnetization reversal and finally achieving saturation magnetization. Once the sample is magnetized, it is much more challenging to interpret the mechanism based on the hysteresis loop alone. The information about the dominating factor can only be obtained by measuring the first magnetization curve [29–37].

Interaction of domain (walls) with paramagnetic inclusions

When a domain wall meets a non-magnetic inclusion, like a trapped particle or a hole, its energy decreases by a proportionate value linked to the inclusion's cross-sectional area. A schematic of the magnetization reversal process regarding a paramagnetic inclusion and a domain wall can be found in figure 2.7. The domain walls have a significantly smaller width than the inclusion radius, an essential factor for the dynamics' behavior.

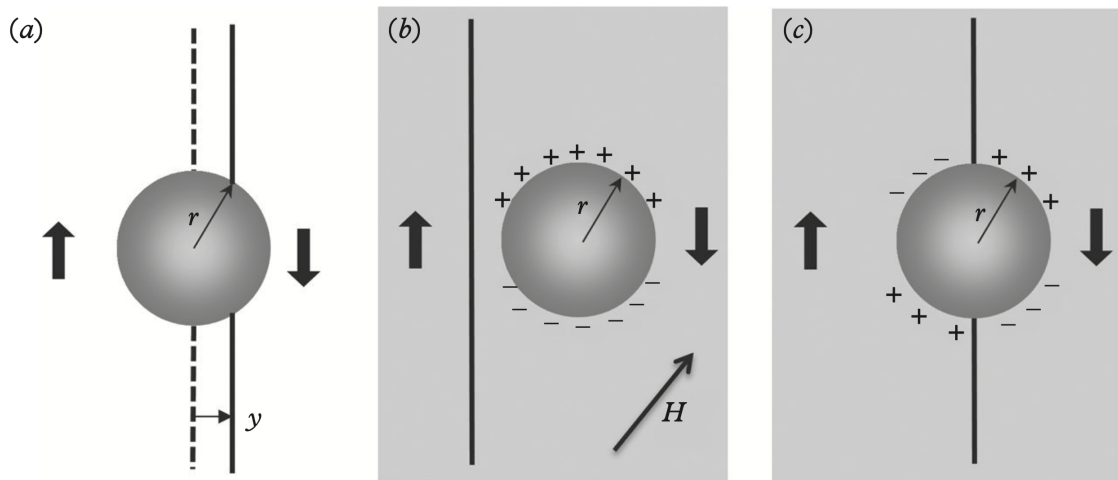


Figure 2.7.: Schematic of paramagnetic inclusion trapped within the magnetic material with a) showing the domain wall passing, b) being trapped in only one domain, and c) with the domain wall going through the inclusion. Adapted from [14].

The interaction of domain walls with inclusions depends on the size and shape of the inclusion and their magnetic susceptibility. Whenever an external magnetic field is applied, domain walls will move toward areas with higher susceptibility. The applied field induces a moment within the paramagnetic inclusions. This induced local field can attract or repulse magnetic domains. If the inclusions are large enough compared to the domains, they can act as pinning sites, significantly reducing the domain walls' mobility. This so-called domain wall pinning is one of the main mechanisms involved in coercivity, as discussed in the previous section. Therefore, the shape of the inclusions can also define the direction of the domain wall within the magnetized sample. The most significant hindering effects occur when the inclusions are approximately the same size as the wall thickness. Chapter 7.7 of reference [14] provides more information about the domain wall interaction with inclusions.

Magnetic shape anisotropy

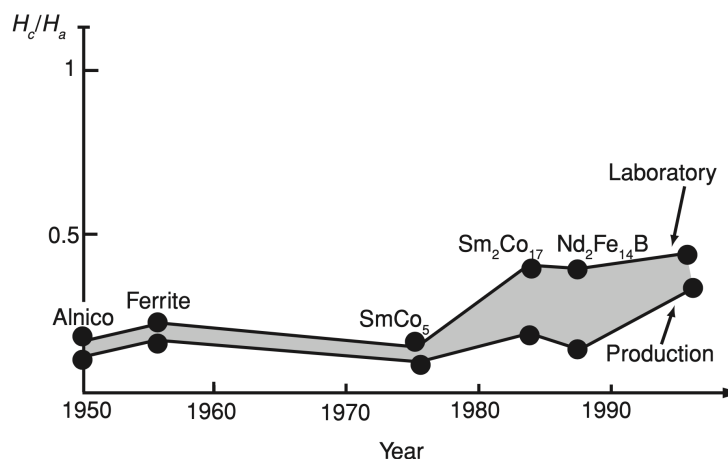
Shape (or magnetostatic) anisotropy arises from discontinuities or divergences at the boundaries of all real-world samples. This creates an additional demagnetization field. The shape anisotropy reduces the overall magnetic moment of the sample [14]. Magnetic shape anisotropy in thin films is a type of magnetic anisotropy that arises due to the flat shape of the magnetic thin film. The shape of the thin film can be treated as a plate-like structure. In thin films, the shape anisotropy can dominate over other types of anisotropy. When the shape anisotropy dominates in thin

films, one finds the films' easy axis parallel to the film's surface because the overall energy in the system can be minimized. Therefore, one can conclude that any anisotropy arising perpendicular to the surface can only come from the deposited sample material and crystal lattice.

2.4. Brown's paradox

William F. Brown proved that the coercive field H_C for a homogeneous, uniformly magnetized ellipsoid is always greater equal than $(2K_1/\mu_0 M_S) - NM_S$, where K_1 is the anisotropy constant, M_S the saturation magnetization and N the demagnetization factor. This inequality is called Brown's theorem. Figure 2.8 describes how H_C/H_A developed over the recent years. One can see that there is still a large gap between the values suggested by Brown's theorem and the materials developed over the years. Some intrinsic and extrinsic magnetic properties were shown and described in the following sections. Their interplay can lead to complex phenomena in the resulting macroscopically measured hysteresis curve. The gap of around 70 % between the theoretical limit and real magnetic materials underlines Brown's paradox [29].

Figure 2.8: Brown's paradox: development of H_C/H_A for different magnetic materials over several years. From reference [12].



In conclusion, this chapter emphasizes the significance of comprehending the underlying mechanisms responsible for Brown's paradox, as it holds crucial implications for gaining a comprehensive understanding of state-of-the-art permanent magnets and advancing the field of magnetic materials.

3. Interaction of photons with matter and synchrotron-based methods

Synchrotron radiation was discovered in 1947 at a General Electric electron synchrotron. "Synchrotron radiation" refers to a broad range of electromagnetic radiation. Energies range from infrared, visible, UV, and over X-ray radiation. First-generation synchrotron sources were created in the 1970s using high-energy physics accelerators without considering X-ray radiation. Dedicated second-generation synchrotron sources followed in the 1980s while keeping X-rays in consideration. The improvement went rapidly, and third-generation synchrotrons came around in the 1990s using focused electron beams and special insertion devices [38–42].

Synchrotron radiation facilities are used for various research fields, from material science to biology. In a synchrotron, electrons are generated and accelerated before being guided into the so-called storage ring, where they continue their journey with an almost constant velocity close to the speed of light. X-ray radiation is formed when electrons change direction within a bending magnet, with a broad spectrum of radiation being emitted along the direction of the traveling electron. In the storage ring, the charged particles are accelerated by a magnetic field towards the center, keeping them in circular motion but losing small amounts of kinetic energy. Radio-frequency cavities make up for the slight energy loss of the electrons. Radiation coming from bending magnets has a wide range of wavelengths or energies, from X-rays to infrared radiation. It is highly intense, making the light ideal for experiments. So-called wigglers and undulators can produce more appropriate radiation than bending magnets. The result is a broad range of usable X-rays for experiments. In this thesis, multiple techniques are utilized, which would not be possible without synchrotron radiation facilities. The techniques used will be described in more detail on the following pages.

3.1. X-ray absorption near-edge spectroscopy

X-ray absorption near-edge structure (XANES) or X-ray absorption spectroscopy (XAS) describes, in general, a measurement technique of varying the incoming photon energy and measuring the absorbance of a given sample around the absorption edge. In the previous section about EXAFS, we focussed on the region far behind the absorption edge, which will give insights into the surroundings. In XANES, we observe the direct influences of the photon absorption of the absorbing atom. With this technique, it is possible to measure the states above the Fermi level. The probed atom's chemical state and local electronic structure can be revealed by targeting this energy region. XANES is sensitive to the energy levels and the density of states of the absorbing atom. It gives a rich insight into the details of electronic

structure. All elements in the periodic table can be used due to the dependence on core-level electrons excited into unoccupied states. One can also use the technique in a surface-sensitive way, for example, by measuring the photoelectron current of the sample as a proxy. However, the measured intensity $I(E, z)$ of a transmission experiment is described by the Lambert-Beer law, which is given by

$$I(E, z) = I_0(E) \cdot e^{-\mu(E) \cdot z}, \quad (3.1)$$

where $I_0(E)$ is the incoming intensity at energy E , z the thickness and $\mu(E)$ the absorption coefficient at energy E .

The measured near-edge spectrum is usually split into two energy regions: pre- and post-edge. The pre-edge region, located just before the absorption edge, is characterized by a series of weak absorption peaks. The symmetry of the local environment strongly influences these peaks.

Two assumptions or approximations regarding the density-of-states (DOS) are made in XANES. First, the ground state can be calculated, so extra valence electrons do not affect the overall DOS. Secondly, the core hole does not affect the DOS.

With Fermi's golden rule (see equation 3.2) one can describe the transition probabilities $\Gamma_{i \rightarrow f}$ from the initial electron state $|i\rangle$ to the final electron state $|f\rangle$:

$$\Gamma_{i \rightarrow f} = \frac{2\pi}{\hbar} |\langle f | H' | i \rangle|^2 \rho(E_f), \quad (3.2)$$

here, the transition rate is described by the squared matrix element with the perturbation Hamiltonian H' and $\rho(E_f)$ is the DOS at energy E_f of the final state $|f\rangle$.

Transition probabilities

Using Fermi's golden rule (see equation (3.2)) and the dipole transition operator, one can write the X-ray absorption transition probability per unit of time like

$$W_{fi} = f(\Omega^3, n) |\langle \Phi_f | \mathbf{r} | \Phi_i \rangle|^2 \delta(E_f - E_i - \hbar\Omega), \quad (3.3)$$

where Ω is the excitation energy and n is the number of photons per unit of time. This means only electronic orbital transitions from $s \rightarrow p$, $p \rightarrow d$, and $d \rightarrow f$ are preferred. This limitation is a subset of the dipole selection rules.

Increasing resolution using HERFD

Usually, the XAS measurement resolution is limited by the core hole lifetime. This shows up through a broadening of the discrete transitions within the spectrum. This can be improved using a usually photon-in-photon-out measurement technique. To use high-energy resolution fluorescence detection (HERFD) in XAS, it is essential to measure the fluorescence lines using an instrumental energy bandwidth equal to or lower than the core-hole lifetime broadening of the absorption edge, similar to X-ray emission spectroscopy. In a HERFD-XAS experiment, the intensity of the

fluorescence line is measured as a function of the incident energy using fluorescence-detected XAS, a secondary process detection method. This approach can yield spectral features with line broadenings smaller than the lifetime broadening of the core hole excited state of absorption. It is important to understand that HERFD should be viewed within the Resonant X-ray Emission Spectroscopy (RXES) context. A HERFD-XAS spectrum may provide a good approximation to the absorption cross-section while reducing lifetime broadening within the measured spectrum.

3.2. Extended X-ray absorption fine structure

Extended X-ray absorption fine structure (EXAFS) is a powerful tool to study the local structures of an atom in an element-specific way. EXAFS uses up to several hundreds of eV higher than the absorption edge. The measurement technique will give distances to the following atomic neighbors, coordination numbers, and species of neighbors [40, 42]. Sayers et al. first presented the measurement, interpretation, and analysis of an EXAFS signal in 1971 (see Ref. [43]). This section demonstrates the basic concept of this method and the concepts of analyzing the absorption edge region itself. Section 3.1 will describe the so-called x-ray absorption near-edge spectroscopy (XANES).

An EXAFS spectrum is measured by shining X-rays onto the sample and measuring the absorption or any other proxy for the absorption. The energy will be changed from a few eV before the absorption edge to multiple hundreds of eV. Absorption and incoming beam (the monitor signal) will be recorded to normalize the measured signal properly.

The origin of the measured EXAFS signal is sketched in figure 3.1. The incoming X-ray photon can excite an electron; this electron in the vacuum will then interfere with itself. This interference changes the absorption at a given incoming X-ray energy, which is depicted in figure 3.1 b). The sample's absorption can be detected by multiple techniques in transmission (collecting the transmitted photon) or in fluorescence (recording photons coming from secondary effects from the sample material).

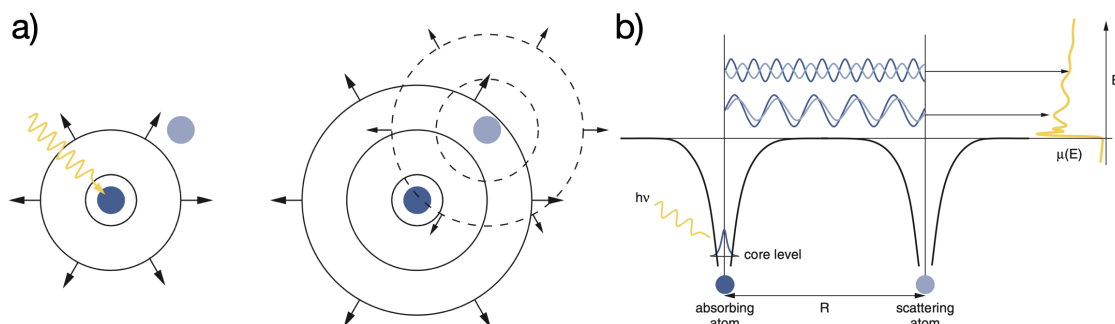


Figure 3.1.: Origin of the EXAFS measurement signal. a) in a simple picture, the excited photon creates a standing electron wave between the nucleus potentials, and b) the difference in interference patterns at different energies leads to a characteristic absorption profile. a) and b) adapted from reference [40].

It is useful to convert the measurement for further analysis into units of the wave number k using,

$$k = \sqrt{\frac{2m_e(E - E_0)}{\hbar^2}}, \quad (3.4)$$

where m_e is the electron mass and E_0 is the energy of the absorption edge.

The following formula can describe an EXAFS measurement:

$$\chi(k) = S_0^2 \sum_j \frac{N_j f_j(k) e^{-2R_j/\lambda(k)} e^{-2\sigma_j^2 k^2}}{k R_j^2} \sin\left(2kR_j + \phi_j(k) - \frac{4}{3}C_{3,j}(T)k^3\right), \quad (3.5)$$

here, $\chi(k)$ is the background spline corrected measured spectrum, S_0^2 the amplitude reduction factor, j is the index for the scattering path, N_j is the number of paths in the neighboring shell at distance R_j , $f_j(k)$ is the backscattering amplitude of the j th atom at wavenumber k , $\lambda(k)$ is the mean free path of photoelectrons at k , σ_j^2 is the mean displacement squared of the j th path, $\phi_j(k)$ is the phase shift by backscattering at atom j . The third cumulant, denoted as $C_3(T)$, characterizes the presence of anharmonic lattice vibrations that manifest at higher temperatures [44]. One can see that one measurement is a superposition consisting of multiple so-called scattering paths. The scattering paths are different electron interferences with different atoms in the absorbed atoms' environment. The method to decipher these paths will be described in the following.

Analysis of measured spectra

After the spectrum is measured, information can be extracted by comparing it to a reference. One can already estimate the environmental difference through the frequency and amplitude of the measured signal. Combining the measured results with simulations can significantly increase the information density. Simulations correlate the measured spectra with the positions of the atom within the crystal structure. Reliable software packages for this type of analysis are *FEFF* [45], *IFEFFIT* [46], and *xraylarch* [47]. These packages utilize the expected crystal structure of the measurement and calculate a spectrum. Specific physical quantities can remain unresolved and susceptible to fitting procedures.

Figure 3.2 shows this analysis procedure by an EXAFS measurement of Nb_3Sn at the Nb K-edge. In this case, the fluorescence lines of Nb were used as a detection mechanism. In a), the measurement is shown (black solid line), together with the so-called background spline (grey dashed line), to subtract from the measurement to remove contributions from excitations of the electrons to the vacuum. In b), the background-corrected and k^2 -weighted spectrum is shown in units of the wavenumber (black solid line). Multiple next-neighbor scattering paths were used to reproduce the measured spectrum based on a crystallographic structure (grey dashed line). A window function (green dashed line) is used for the Fast Fourier Transform (FFT) depicted in c) to reduce the contribution of high-frequency noise. Additionally, in c), the FFT of the measurement is shown (black solid line), and the FFT of the calculated spectrum (grey dashed line). One can see good agreement for the first three scattering shells. The phase shift from equation 3.5 is not included in

the FFT. Therefore, the emerging peaks tend to be shifted towards lower R-values than the actual bond lengths between the absorbing atom and the scattering shell.

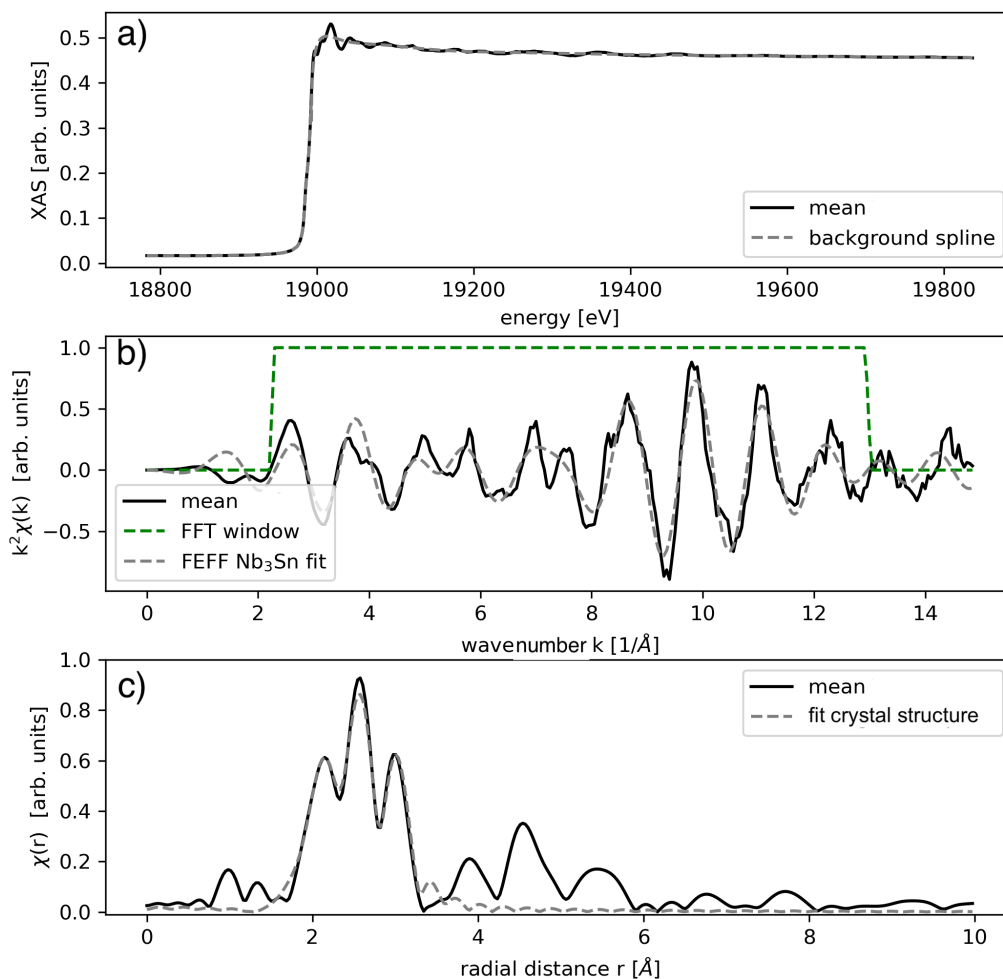


Figure 3.2.: Example of an EXAFS analysis process. a) measurement and background spline. b) to wave number converted and k^2 weighted spectrum with the fit. c) FFT of data from plot b). Data published in reference [9]

The fitting procedure will be expanded in section 4.1, where the multipath and degeneracy approach is used to quantify the phases of a Sm-Co thin film. Using EXAFS measurements is, therefore, a valuable tool to study the local environment of an element.

3.3. X-ray magnetic circular dichroism

Dichroism is derived from the Greek word *dikhroos*, which originally translates to "two colors". Magnetic circular dichroism refers to the phenomenon where the absorption coefficient of a magnetic material depends on the photons' polarization and orientation of the external applied magnetic field.

Erskine and Stern first described the so-called XMCD effect [48]. Experimentally proven about 12 years later by G. Schütz et al. [49] in iron and later in other metals [50]. The discovery of magnetic dichroism in core-level X-ray spectroscopy

has paved the way for element-specific magnetization measurements and magnetic domain imaging.

An additional advantage of XMCD is the possibility to distinguish between orbital and spin magnetic contributions to the net magnetic moment of an atom. Magneto-optical sum rules exploit this quantitatively; this will be described on page 21.

In figure 3.3, the XMCD is shown schematically. The XMCD effect can be described and understood in a *two-step* process (further reading recommendation: section 9.6 of reference [51]).

Step one, the incoming X-ray photon transfers its angular momentum to the excited photoelectron due to the conservation of angular momentum. If the probed state exhibits a spin-orbit split ground state (for example, for electronic $2p$ states, see equation (3.6)), parts of the photon's momentum can be transferred to the spin through spin-orbit coupling (see section 2.2 'Spin-orbit coupling'). The excited electrons are spin-polarized. The sign of polarization is the opposite for left and right circular polarized X-rays.

In *step two*, the valence shell acts like a spin detector, which has the optimum detection if the axis of the valence shell spin is aligned parallel with the photoelectron spin quantization axis.

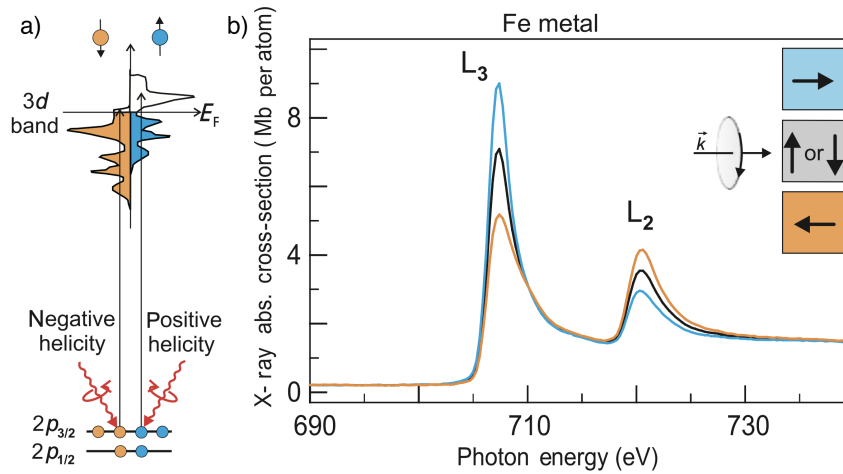


Figure 3.3.: Schematic of representation of a) spin-up and spin-down states in Fe, and b) measured spectra with differently polarized photons and preferred magnetization directions. Adapted from reference [51].

The energy shift ΔE within the spin-orbit coupled ground states can be calculated as follows:

$$\Delta E = \frac{\beta(n, \ell)}{2} (j(j+1) - \ell(\ell+1) - s(s+1)) \quad (3.6)$$

where:

$$\beta(n, \ell) = Z^4 \frac{\mu_0}{4\pi} g_s \mu_B^2 \frac{1}{n^3 a_0^3 \ell(\ell+1/2)(\ell+1)}$$

here, Z is the number of protons within the nucleus, and n is the principal quantum number. With Z^4 , the spin-orbit energy increases rapidly with increasing atomic number.

Hard XMCD

In the hard X-ray region (above ca. 4000 eV), usually, the directly probed electronic states do not exhibit a magnetic moment because the probed states are the p (for TM) or d (for RE) orbitals (in dipole approximation). These shells are either filled or empty. However, due to hybridization and polarization through the half-filled magnetic shells, the final p and d states can exhibit a small magnetic moment. Additionally, quadrupolar transitions can exhibit a contribution to the measured signal. These are transitions from $s \rightarrow d$ or $p \rightarrow f$. Additionally, no spin-orbit splitting of core states is present. However, this results in a ca. 100 times smaller XMCD signal at the edges of the hard X-ray region for most TM and RE.

Magneto-optical sum rules

The magneto-optical sum rules have been derived in the ground laying work by Thole, Carra, König, and Sette [52–54]. They are most used within the soft X-ray region (below 2000 eV). This is because in this range for the $3d$ and $4f$ systems, the relevant dipolar transitions will be probed. Chen et al. [55] verified the sum rules by measuring and calculating the $3d$ moments of Cobalt. The complete set of sum rules and the derivation for the $3d$ and $4f$ systems can be found in appendix A.

Although magneto-optical sum rules give a reasonable estimation of the magnetic moment per atom, the largest contribution of inaccuracy follows from including $l \rightarrow l - 1$ dipole transitions only, which neglects the overall quadrupolar transitions [56–58]. However, applying sum rules is, up to now, the only direct tool to separate spin and orbital contribution from transition metals up to actinides also in small concentrations [59].

We can conclude and summarize that the dependencies of the intensity of the measured XMCD signal I_{XMCD} can be described by:

$$I_{\text{XMCD}} \propto P_{\pm} |\vec{m}| \cdot \cos \Theta, \quad (3.7)$$

where P_{\pm} is the ratio of polarized light within the X-ray beam, $|\vec{m}|$ the magnetization of the atom, and Θ the angle between the magnetization and the incoming wave vector.

X-ray excited optical luminescence

The thin films measured at beamline 6.3.1 at the Advanced Light Source (ALS) were measured in X-ray excited optical luminescence (XEOL) mode. This provides the benefit of a real transmission experiment in the soft X-ray region. Therefore, one has no electronic saturation effects from the sample’s surface as in total electron yield detection methods [60, 61]. In grazing incidence, a reduction of the edge, which is smaller in energy, could be observed in the overall XMCD signal. This generally leads to underestimating the orbital contribution to the net magnetic moment of the measured atom, which can be corrected for [62].

When an insulator absorbs X-rays, they generate high-energy electrons. These electrons create additional conduction electrons and valence holes through electron-electron scattering. Some of these created electron-hole pairs then emit luminescence

as they recombine through defect states [63]. In Al_2O_3 , the Cr^{3+} impurities are responsible for the luminescence, which is very sharp signal. [64]. This luminescent behavior comes from the ${}^2\text{E} \rightarrow {}^4\text{A}_2$ transition in an octahedral environment (the R1 and R2 doublet) [65].

3.4. Magnetic laminography

Magnetic laminography is a relatively new ptychography-based imaging technique that has recently gained significant attention [66, 67]. Ptychography is a computational imaging technique used in microscopy. This method creates images by analyzing numerous coherent interference patterns produced when X-rays scatter from an object of interest. The advantage of using ptychography in the angled setup (laminography) is that one can utilize only one rotation axis to collect all the information necessary and enough data sets to reconstruct all magnetic vectorial contributions [68]. The measurement setup in laminography is tilted, meaning the rotation angle is not perpendicular to the incoming beam. The absence of a 180° symmetry and the presence of a 360° symmetry, related to those seen in other tomography setups, results, therefore, in a significantly amplified information density upon measurement of all projections [69, 70].

The technique provides high-resolution images of magnetic domain structure. Tomography is the underlying technology; in this, multiple images of an object are captured from multiple angles. A 3D reconstruction is then generated through computational algorithms. This would enable the visualization of the magnetic domain structure spatial resolutions down to 20 nm [66]. A significant advantage is that it can provide detailed information about the magnetic domains within a material without destructive testing.

The measured spatial resolution of the technique is much smaller than the step size of the specimen sampling [71, 72]; it offers, therefore, higher spatial resolution than comparable microscopy techniques.

Visualizing the magnetic domains in 3D is essential to understanding the behavior of magnetic materials. Developing new materials with improved properties and performance relies on understanding the microscale. Chapter 5 describes this technique, which is used to unravel the 3D magnetic structure of a hot-deformed Nd-Fe-B permanent magnetic material.

Coherent diffraction imaging (CDI)

When electromagnetic waves encounter an obstacle or aperture comparable in size to their wavelength, diffraction occurs, leading to the divergence of the wavefronts. When waves are diffracted, they interfere with each other, resulting in patterns forming on a detector set up behind the obstacle. These fringes can be analyzed to determine the atomic structure of the studied material (the obstacle). The diffraction pattern contains information about the crystal pattern of the illuminated spot. The pattern reveals an approximation of the view's Fourier transform, representing the intensity distribution of the sample's absorption. One of the critical advantages of CDI is its ability to achieve spatial resolutions beyond the limitations of the diffraction limit since the technique does not rely on lenses or other optical elements to create the image.

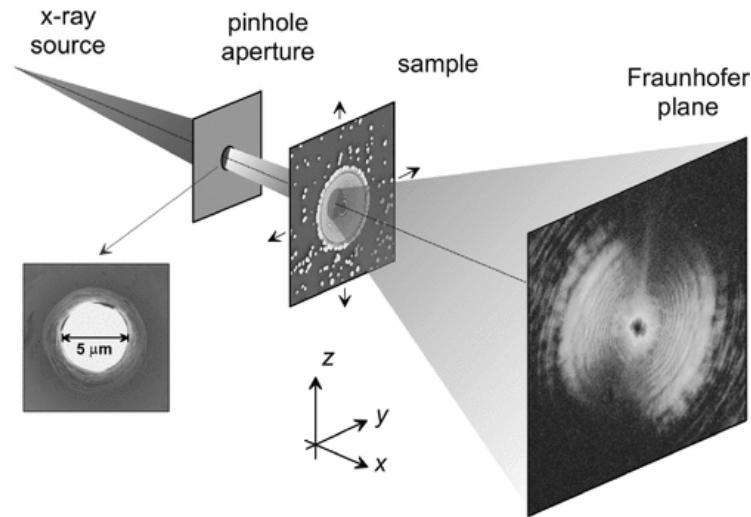


Figure 3.4.: Schematic of the experimental setup. The sample can be shifted in multiple directions to scan the whole area. Adapted from reference [73].

The coherent beam gets restricted, for example, as shown in figure 3.4 with a hole or using slits. In this way, one can restrict the illumination area on the sample. The sample is then scanned, and the diffraction pattern is recorded for multiple spots on the sample. After the whole sample is scanned, iterative algorithms need to be used to allow the reconstruction of high-resolution images. These algorithms will be described in the next paragraph.

Phase retrieval algorithms

During the scattering process, the phase information is lost. Therefore, phase retrieval algorithms have to be used to construct the view of the sample.

Many phase retrieval algorithms exist, including iterative, non-iterative, and hybrid algorithms. This work used an iterative phase retrieval algorithm, which is a computational method to recover the phase information of a signal or image from its intensity measurements. The basic idea behind an iterative phase retrieval algorithm is to update the estimated phase distribution until convergence is achieved iteratively.

The iterative phase retrieval algorithm typically starts by initializing the phase distribution randomly or with some prior information about the predicted signal or image. Then, it computes the Fourier transform of the estimated phase distribution to obtain an estimate of the complex amplitude of the signal or image. The process is schematically shown in figure 3.5. The magnitude or intensity of the measured data is then compared to the estimated magnitude or intensity to obtain a measure of the error. Then, after the phase distribution is updated, the process repeats the Fourier transform and compares it to the measured data. The process continues until convergence is achieved. Convergence is achieved by monitoring the change in the error measure between successive iterations.

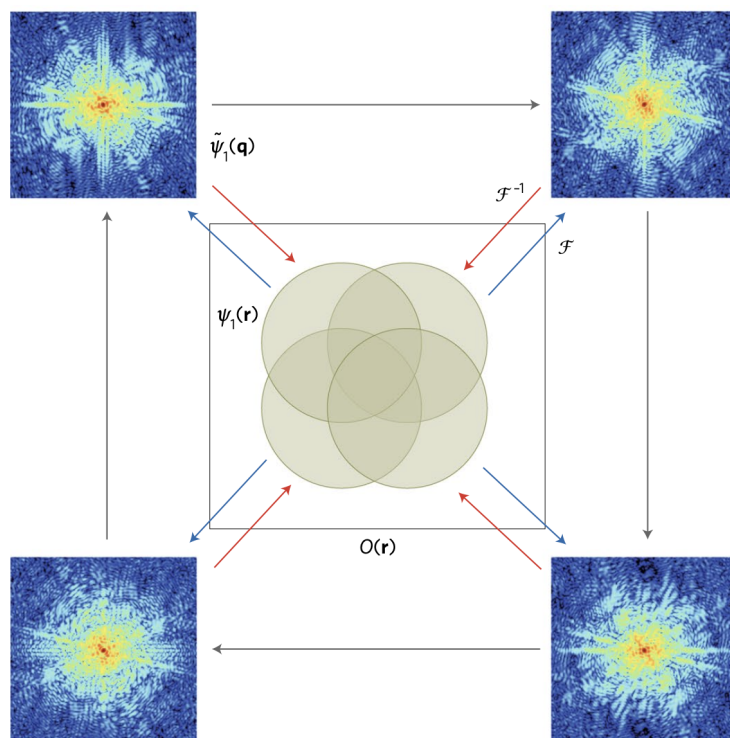


Figure 3.5.: Schematic process description of the iterative phase retrieval in ptychography. From reference [71].

Reconstruction

This paragraph explains the general concept of reconstruction in ptychographic measurements. The explanations will only go into some detail. References [68, 74, 75] give more information on the process. In the previous paragraphs, we described how to get from the overlapping diffraction patterns to the 2D projections of the sample. Multiple 2D projections construct a 3D data set from the measurement — the filtered back projection (FBP) method based on the Fourier slice theorem is used. The Fourier slice theorem states that the Fourier transform of the projection of a 2D object is the same as the 2D Fourier transform of the 2D object and then takes a slice through its origin, which is parallel to the projection line. 2D Fourier images can be reconstructed from multiple Fourier transforms of the projections.

The concept of the 'filtering' works within the FBP algorithm is shown in figure 3.6¹. The measured projection (red) will be fast Fourier transformed (green), then usually a Ram-Lak filter (olive) is applied to the measured signal in the frequency domain. The filtered signal (orange) will be inverse fast Fourier transformed into real space (pink).

The method of back projecting is shown in figure 3.7. The projection of the object is spread out over the whole image plane. The difference between spreading out the unfiltered projection (a and b) and the filtered (c and d) is relatively straightforward. Since the Ram-Lak filter reduces the low-frequency contributions compared to the high frequencies, one can achieve a much sharper result of the back-calculated object.

¹python code to recreate the figure (free, public domain): <https://gist.github.com/gnznng/7fe19818250aa4bd89be4979a96c966c>

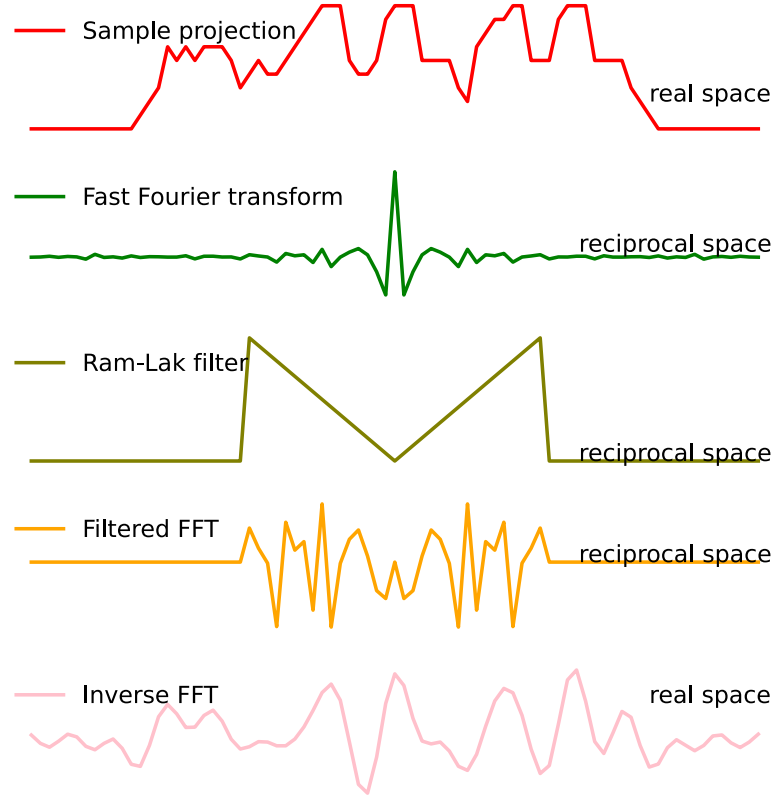


Figure 3.6.: Schematic of the filtered backward projection in 1 dimension.

Involved scattering factors

Two scattering factors generally describe the scattering between the X-ray photon and the atom:

$$f(\vec{r}') = f_C(\vec{r}') + f_M(\vec{r}')(\vec{m}(\vec{r}') \cdot \vec{e}_z), \quad (3.8)$$

where f_C is the electronic scattering factor and f_M the magnetic scattering factor. The scalar product describes the angle dependence of the XMCD signal or the magnetic probe, which shows that only the magnetic contribution along the z -direction, in this case, can be probed. And $\vec{m}(\vec{r}')$ is the normalized magnetization to the saturation magnetization at the cartesian coordinates $\vec{r}' = (x', y', z')$ in sample coordinates.

With generalization and introduction of laboratory coordinates, we can express the above in for the n th XMCD projection P_n , which is related to the measured transmission amplitude A_n via Lambert-Beers-law (similar to the already introduced equation (3.1)):

$$A_n(x, y) = \exp\left\{\frac{-2\pi}{\lambda} P_n(x, y)\right\}, \quad (3.9)$$

where λ is the X-ray wavelength.

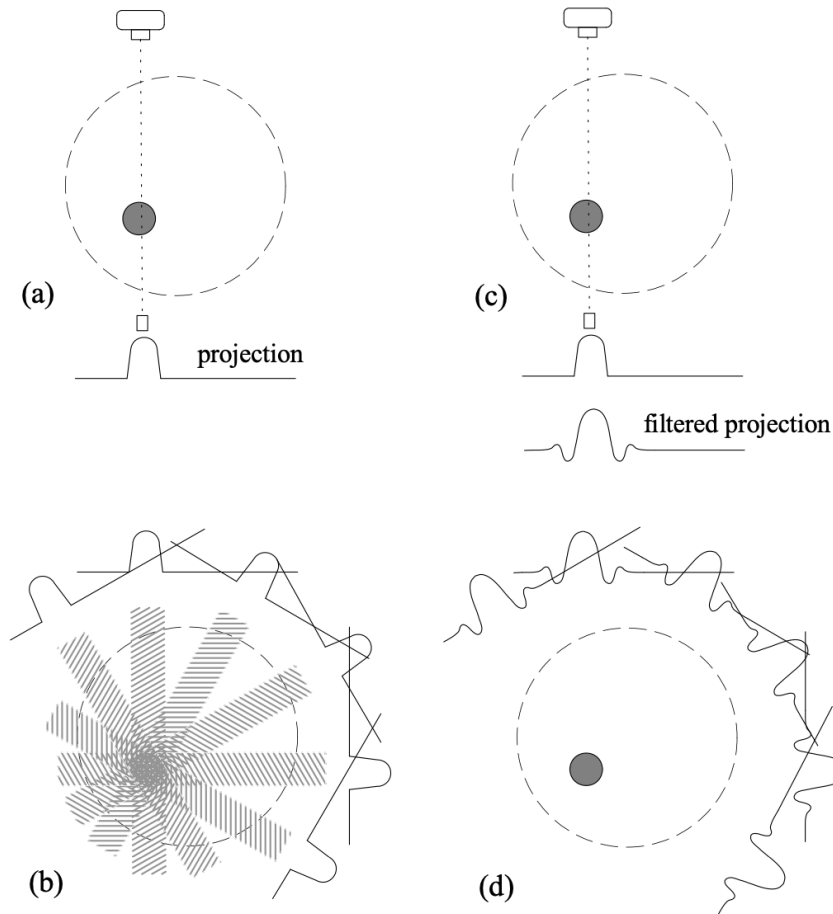


Figure 3.7.: Back projections of unfiltered (a and b) and filtered back-projections (c and d). The measured projection profiles are spread out over the image plane in unfiltered back projection. In filtered back projection, the projection profiles are filtered before being projected onto the image plane. Adapted from reference [76].

We can write $P_n(x, y)$ in the following way:

$$P_n(x, y) = \frac{-r_e}{2\pi} \lambda^2 \left(\sum_k n_{\text{at}}^k \int I(f_C^k(R^{(n)})) dz \pm n_{\text{at}}^{\text{mag}} \int I(f_m^{(n)}(R^{(n)})) ((R^{(n)+}) \vec{m}(R^{(n)}) \cdot \vec{e}_z dz) \right), \quad (3.10)$$

here, $I()$ selects the imaginary part of the complex terms f_C and f_m , $R^{(n)}$ is the rotation matrix describing the sample orientation, and r_e is the electron radius.

Reconstruction of a 3D vector field

In tomography, a scalar field is typically reconstructed, and all the aspects described in the preceding paragraphs apply to scalar fields. However, retrieving the complete magnetic information requires the reconstruction of a 3D vector field. In the 1990s, Prince demonstrated the remarkable possibility of reconstructing an arbitrary n-

dimensional vector field. This breakthrough involved utilizing n tomographic projection datasets, where each dataset is uniquely sensitive to one of the n directions of the vector field [77, 78]. Therefore, with only three tomographic datasets, it is possible to reconstruct a three-dimensional vector field like all three components of the magnetization vector. This was shown later by Braun and Hauck [74], they also state that when the contrast is probed by something like XMCD, we can always subtract the solenoidal component of the vector field ($\nabla \cdot \vec{m}_s = 0$). One requires more a priori information or supplementary data sets featuring a distinct rotation axis to achieve complete reconstruction.

The previously described FBP or simulations can estimate an early guess of the results. The process comparing the measured data ($P_n(x, y)$) with the estimation ($\hat{P}_n(x, y)$) is then iterated multiple times to reduce the difference between them. The metric of error ϵ is defined as:

$$\epsilon = \sum_n \sum_{x,y} \left[\hat{P}_n(x, y) - P_n(x, y) \right]^2. \quad (3.11)$$

The magnetic gradient of the error metric can then be given as:

$$\frac{\partial \epsilon}{\partial \vec{m}(\mathbf{R}^{(n)} \vec{r})} = 2 \sum_n \left[\hat{P}_n(x, y) - P_n(x, y) \right] \mathbf{R}^{(n)} \begin{bmatrix} 0 \\ 0 \\ 1 \end{bmatrix}, \quad (3.12)$$

where $\mathbf{R}^{(n)} \vec{r}$ are the coordinate of the object. The multiplication with the column vector $[001]^\top$ describes that we are only sensitive along the direction of sample magnetization along the X-ray direction. By setting $\mathbf{R}^{(n)} [001]^\top = 1$, we can describe the electronic scalar component, which was used to estimate the location of the magnetic material. This is then used as a constraint in the magnetic reconstruction.

Estimating spatial resolution via Fourier shell correlation

The Fourier shell correlation can be used to find the spatial resolution of a 3D data set. Van Heel and Schatz described the method in reference [79]. If N projections are used to build a 3D model. One can use $N/2$ to avoid crosscorrelation between these and build two models of the same original data set. The *FSC* can then be calculated via

$$FSC = \frac{\text{Re}(\sum_{\text{shell}} F_1(s) \cdot F_2^*(s))}{(\sum_{\text{shell}} |F_1(s)|^2 \sum_{\text{shell}} |F_2(s)|^2)^{1/2}}, \quad (3.13)$$

where s is distance in reciprocal space, F_1 is the Fourier transform of data set 1 and F_2 is the Fourier transform of data set 2. If $F_1 = F_2$, then *FSC* is exactly 1, therefore high correlation means a good resolution. Usually, a *FSC* threshold is determined from which a resolution of the datasets can be estimated. An example of this threshold would be the half-bit, which means using the intersection with the point where only 1/2 bit of information per pixel is present [80].

Preferred orientations lead to anisotropic resolution, which can also be observed in our data set for the magnetic directions. Another limitation is beam coherence, non-parallel incoming X-rays contributing with an angle and smearing out the projection.

4. Element-specific investigations of RE-Co systems

Due to their unique magnetic properties, Sm-Co-based permanent magnets play a significant role in various applications. These magnets are composed of Sm and Co and small amounts of other dopant elements, e.g., Zr, Fe, Cu. One of the critical advantages of Sm-Co-based permanent magnets against the well-known and well-established Nd-Fe-B-based magnets is their exceptional performance at high temperatures. This goes hand in hand with excellent thermal stability, making it a suitable magnet where magnetic strength is needed at elevated temperatures. Furthermore, Sm-Co-based permanent magnets have a higher intrinsic coercivity than their competitor, e.g., Nd-Fe-B. This is necessary in environments where magnets are exposed to strong external applied magnetic fields, which could potentially demagnetize other magnetic materials [81].

This chapter will describe and analyze parts of the RE-Co system family to better understand the model system, Sm-Co, used daily. In particular, the RE-Co systems contain light rare-earth elements like Sm and Ce. Y is technically not a rare-earth element but an interesting element to dope with due to its similar chemical properties. Unlike Sm and Ce, Y has in its 3+ configuration no magnetically important 4*f* electrons, which could contribute to the magnetism or magnetic anisotropy. Later, Cu will be added to the SmCo₅ to observe how this addition of a non-magnetic TM element will change the magnetic properties of the compound. RECo₅ intermetallic compounds were already known in the late '60s due to their enormous strong uniaxial magnetic anisotropy [12, 82, 83]. And even after ca. 60 years, SmCo₅ has the largest uniaxial magnetocrystalline anisotropy.

As one of the critical intrinsic magnetic properties, magnetocrystalline anisotropy sets an upper limit on the magnetic coercivity, which is derived from the magnetic reversal processes dominated by the underlying microstructures (see section 2.4 about Brown's paradox). Together with the saturation magnetization, magnetic coercivity and mainly the energy product $(BH)_{\max}$ are essential parameters characterizing the performance of permanent magnets [20, 24, 84].

The following section analyzes Sm-Co(-Cu) and (Y,Ce)-Co magnetic thin films. Bulk material will be examined for the (Y,Ce)-Co system.

4.1. Sm-Co(-Cu) thin films

This first section investigates magnetic thin films prepared by molecular beam epitaxy (MBE). The goal is to create model systems of single phases. Although the ratio and the amount of the elements applied to the substrate can be determined and controlled very precisely, the substrate can significantly influence the crystal lattice parameters, leading to strain and possible altered physical properties and locally different phases.

Preparation of thin films by molecular beam epitaxy

The measured thin films were produced by MBE in the group of Prof. Alff at TU Darmstadt by Shalini Sharma and Georgia Gkouzia. Figure 4.1 shows a schematic of the MBE vacuum chamber. As mentioned, a high vacuum is needed to grow a clean crystal to remove impurities or contaminants from the air. The base pressure of the system was 10^{-9} mbar. The source materials are inside the chamber in several crucibles loaded with high-purity elemental compounds or materials heated by electron guns. This causes the material in the crucibles to evaporate, forming a molecular beam moving towards the substrate. To encourage the c-axis orientation of the film, it is preferable to utilize Al_2O_3 substrates with a 001 orientation. The substrate is often heated to facilitate better adhesion and promote the growth of a clean phase and clean surface. The substrate will be annealed before the deposition for a few hours at different temperatures in the MBE chamber. The growth happens layer by layer on the substrate with no buffer layer between the substrate and the desired thin film material added during the MBE process.

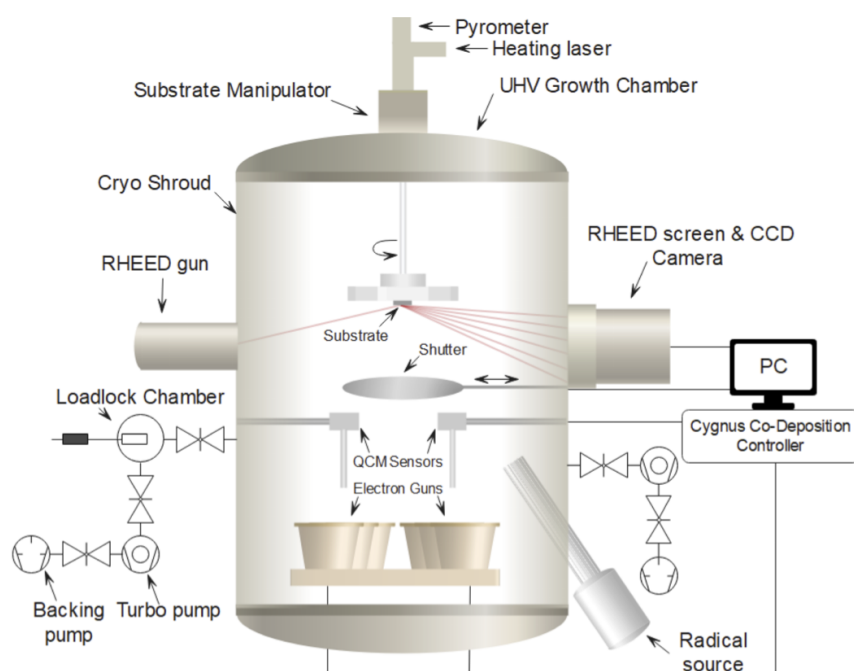


Figure 4.1.: Schematic of MBE chamber used to prepare the magnetic thin films. Courtesy of Georgia Gkouzia from TU Darmstadt.

During the deposition process, it is worth controlling and monitoring several parameters within the vacuum chamber and on the film. Reflection High Energy Electron Diffraction (RHEED) observes the growth and structure during the deposition. Especially for the RE materials used in producing the films, it is crucial to use a sealing capping layer after the growth of the desired thin film is completed. RE elements have a high oxidation probability under ambient conditions. After applying the capping layer, the thin film is safe to remove from the MBE chamber and can be further characterized by X-ray diffraction (XRD) to determine the crystal structure. X-ray reflectivity (XRR) confirmed the thin films' thickness, estimated to be around 30 nm. The magnetic properties of the films were measured by a superconducting

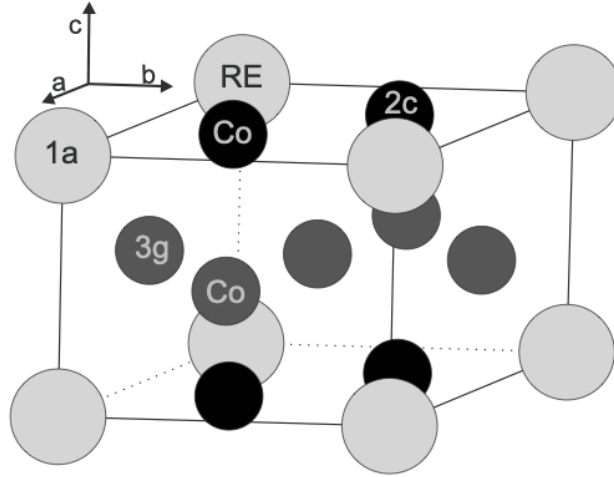


Figure 4.2.: Schematic of crystal structure of the 1:5 phase with Co on the 3g and 2c and a RE atom on the 1a site.

quantum interface device (SQUID) in two directions, field-aligned out-of-plane and in-plane of the films, which will be shown in more detail in the following sections.

Local structure: natural phase decomposition in Sm-Co thin films

This subsection is based on the work published by S. Sharma et al. in reference [85], where EXAFS analysis leads to further proof and quantification of the two present phases in the grown film.

As described in section 3.2, EXAFS is a powerful tool to unravel the geometric structure of a compound by observing what is near the X-ray absorbing atom. Using two crystal structures and models relies on a powerful computing exercise to distinguish between the phases and quantify their ratio. This section will have a closer look at how the analysis was performed and how the local geometric structure of the prepared Sm-Co thin films appears.

In general, the transition from the hard magnetic SmCo_5 phase to the softer $\text{Sm}_2\text{Co}_{17}$ phase can be described as the following: one Sm atom will be exchanged in the center of the SmCo_5 (see figure 4.2 with a space group of $P6/mmm$) structure into two Co atoms, resulting in the stoichiometric transition from $\text{Sm}_3\text{Co}_{15}$ to $\text{Sm}_2\text{Co}_{17}$ [86].

For the *FEFF* calculations, a magnetically relaxed structure with a slightly different Co atoms arrangement was used. If you compare the relaxed structure to the 1:5 phase structure, the hexagonal Co atoms appear more circular. The comparison between the 1:5 phase and the relaxed 2:17 can be seen in figure 4.3. Letting the 1:5 phase magnetically relax did not change the lattice parameters or the crystal structure. The relaxation process was done by Harish Kumar Singh from the group of Prof. Zhang at TU Darmstadt. The main difference between both structures is the added Co dumbbell at one of the RE places per unit cell. This can be seen by the additional Co atom in the lower left and right corner of figure 4.3b). Debora Meira-Motta performed the measurements at the APS in Chicago at EXAFS beamline 20-BM [87].

The EXAFS and XANES at the Co K-edge at 7709 eV can be seen in figure 4.4. The data was collected using a Ge 13-element detector. For the dark blue shown

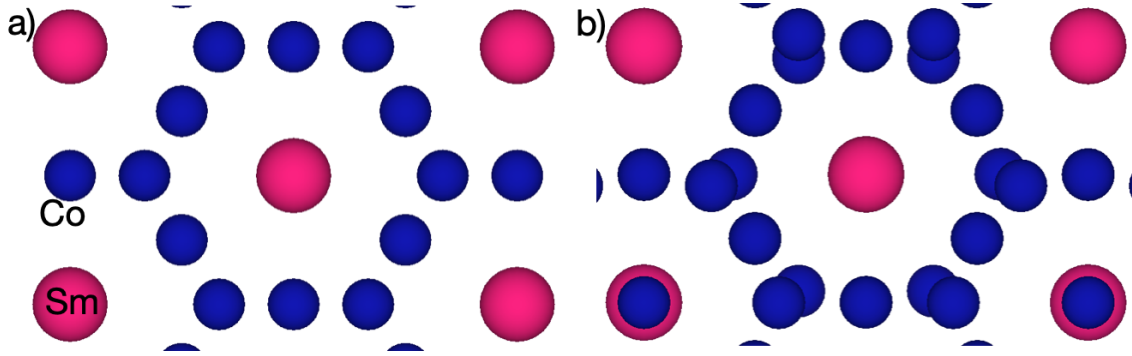


Figure 4.3.: Sm atoms in pink and Co atoms in blue, crystal structure of a) 1:5 phase of the Sm-Co and b) relaxed 2:17 phase, the exchanged Sm atom for two Co atoms can be seen in the bottom row. Structure depicted by *VESTA* [88].

EXAFS signal, multiple scans were merged. As a background spline, the *autobkg()* function of *xraylarch* was used, which is shown in light blue in the subfigure a). In subfigure b), the near-edge region is shown from 7690 eV to 7740 eV, where the distinct in-edge feature can be found at around 35% of the background intensity. The background spline corrected signal is shown in subfigure c). The energy axis was also converted into units of the wavenumber k in inverse Å with the equation (3.4). Additionally, the calculations obtained by *FEFF* and three different superpositions of the two phases are shown, which will be described in more detail in the next paragraph. Also shown is the window function used for the Fourier transform shown in subfigure d). Here, the Fast Fourier Transform converts the signal back into real space. The value for the first neighboring shell is off by ca. 0.5 Å due to the phase shift in the EXAFS equation (see equation (3.4)). One can see that the best fit for 0% overestimates the contributions at the larger distances R . The 100% 1:5 phase fit shows a lack of accuracy around the 3 Å mark. The best fitting model lies between a mixed contribution of 1:5 and 2:17 phases. The equal phase contributions are also shown in light blue, which shows the best fitting result.

The scattering paths for the 1:5 phase are relatively straightforward: 2 different Co absorber places at the $2c$ and 3 at the $3g$ Wyckoff positions. For the absorbing Co in the relaxed 2:17, it is a little more complex. 4 different absorber places as a fraction of 17 Co are involved in the structure: 2 at the $4f$, 3 at the $6g$, 6 at the $12j$, and 6 at the $12k$ Wyckoff positions. Due to the rounding of next neighbor distances in the relaxation process, the path degeneracy had to be adjusted in the fitting process [89].

So, the superposition of the measurement signal containing both phases can be described as follows:

$$\begin{aligned}
 \chi_{Co} = & p_{1:5}(2/5 \cdot Co_1^{1:5} + 3/5 \cdot Co_2^{1:5}) \\
 & + (1 - p_{1:5}) \cdot (2/17 \cdot Co_1^{2:17} + 3/17 \cdot Co_2^{2:17} \\
 & + 6/17 \cdot Co_3^{2:17} + 6/17 \cdot Co_4^{2:17})
 \end{aligned} \tag{4.1}$$

For the *FEFF* calculations, the above-described atom models were used, together with $T_{\text{Debye}} = 332$ K for the 2:17 phase [90] and 272.5 K for the 1:5 (mean for the basal and c-axis [91]). Measurements were conducted at ambient temperatures. The

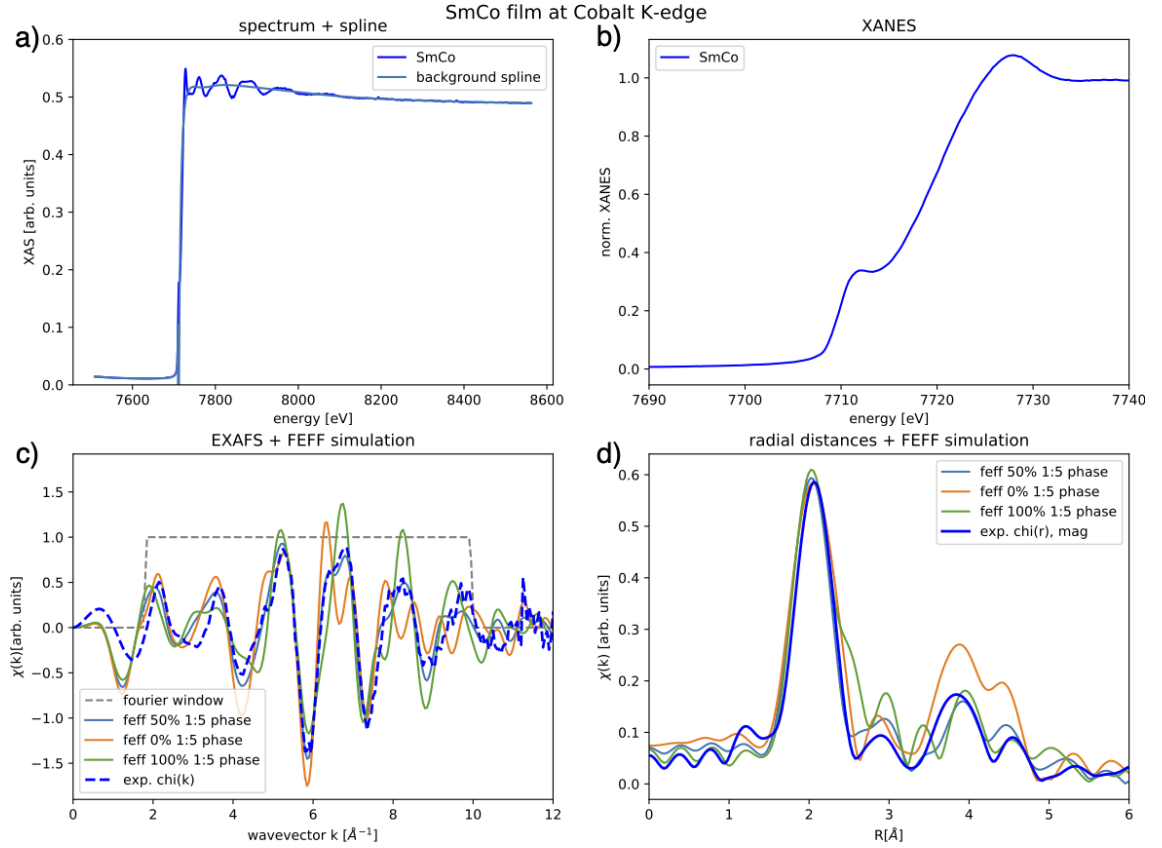


Figure 4.4.: a) EXAFS measurement at Co K-edge and background spline used for the analysis, b) near-edge region obtained during the measurement, c) k^2 weighted $\chi(k)$ with corresponding *FEFF* calculations and window functions for the Fast Fourier Transform, d) Fast Fourier Transform for real space representation of the measurement and *FEFF* calculations.

fitting procedure was performed in k^2 -space. The parameters obtained by the fitting procedure can be found in table 4.1.

Fitting parameters (units)	SmCo ₅	Sm ₂ Co ₁₇
S_0^2	0.85 ± 0.14	0.85 ± 0.14
ΔE (eV)	-0.02 ± 1.56	-0.02 ± 1.56
α	-0.0074 ± 0.0049	-0.0024 ± 0.0053
σ^2 (Å ²)	$2.5 \times 10^{-5} \pm 0.0041$	$3.6 \times 10^{-4} \pm 0.0031$
p	0.351 ± 0.181	0.6491 ± 0.181

Table 4.1.: Parameters obtained for SmCo₅ and Sm₂Co₁₇ phases on fitting the experimental spectra

Here S_0^2 is the amplitude reduction factor, ΔE the energy shift in eV, α the difference to the lattice from the assumed lattice constant, σ^2 the static disorder, and p the contribution to the total signal of the fit. The statistical goodness of the fit is given by the R-factor [92]. The best fit presented in figure 4.5 achieves around 0.06, where the pure contributions are around a factor of 0.2, which is significantly worse and not considered as an excellent fitting result, seen in figure 4.4 c) and d).

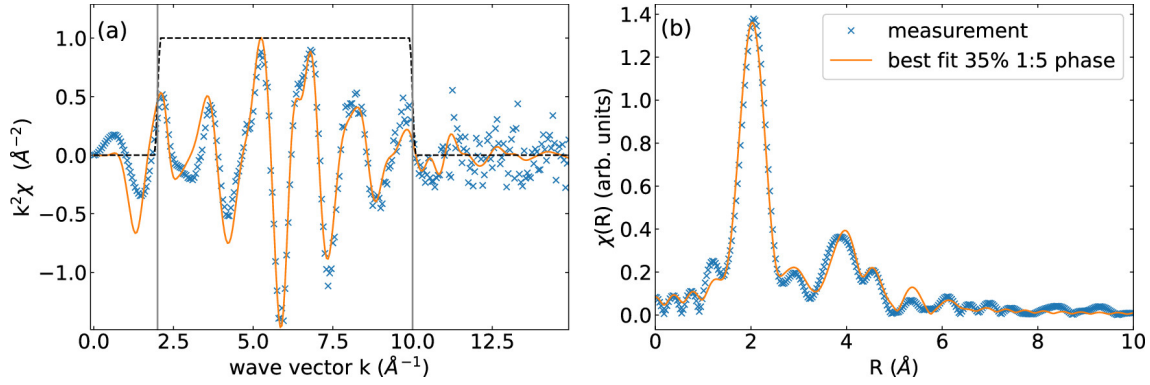


Figure 4.5.: a) Measurement and fit result in k -space, b) Fast Fourier Transform of measurement and fit result. Adapted from reference [85].

EXAFS measurements at the Co K-edge verified and quantified the phase mixture of 1:5 and 2:17. The indication from a smaller volume could be found by the high-angle annular dark-field-scanning transmission electron microscopy (HAADF-STEM) measurements, which can be seen in figure 4.6 with the line profile of both regions. For the $\text{Sm}_2\text{Co}_{17}$ phase along the $[-100]$, every 3rd atomic column exists out of purely Co atoms; the intensity in this line is much smaller. One can also observe that this low-intensity atom column shifts one atom and is below a mixed atom position in the next atomic row.

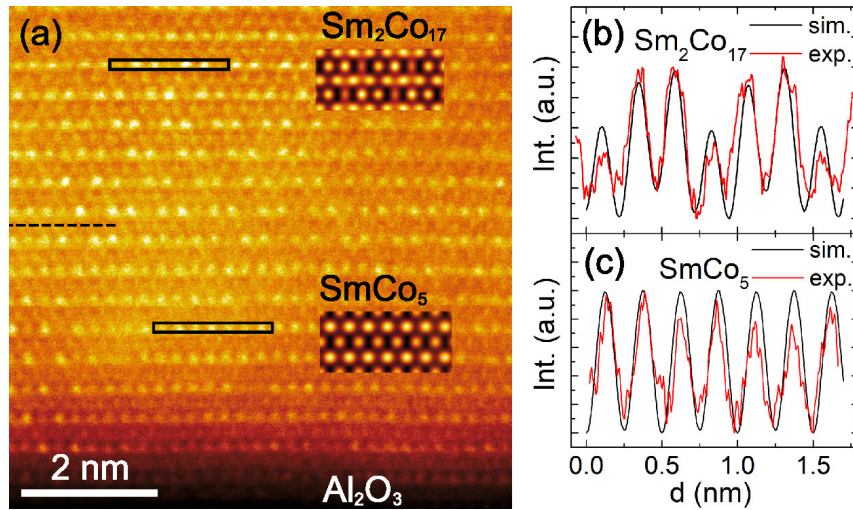


Figure 4.6.: a) HAADF-STEM image with indication of both phases and line profile of experiment compared with simulation for b) 2:17 phase and c) 1:5 phase. Adapted from reference [85].

The coupling of soft and hard magnetic phases can lead to increased magnetic properties, which can be observed in macroscopic measurements. The magnetometry measurements for the discussed thin film can be found in figure 4.7a). Here, a "single-phase"-like hysteresis loop can be observed, which points towards a strong exchange coupling between the SmCo_5 and $\text{Sm}_2\text{Co}_{17}$ phases through their smooth boundary and stacking on top of each other. During the first magnetization with a dominating nucleation mechanism, the magnetization of the specimen increases relatively rapidly since a dominating amount of nucleation centers will give rise to a

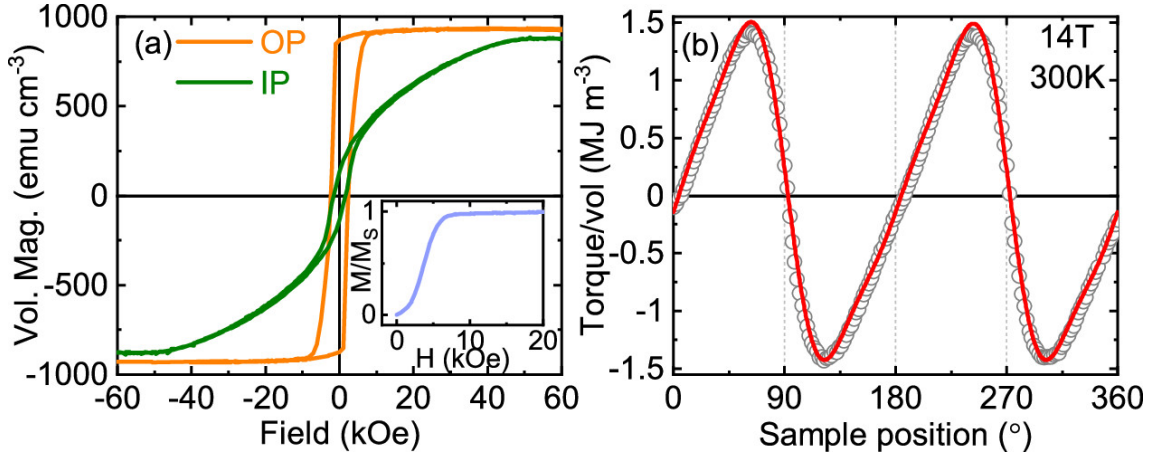


Figure 4.7.: (a) Magnetic hysteresis curves of the Sm–Co thin film measured out-of-plane (OP, orange) and in-plane (IP, green) of the film surface at room temperature. The inset shows the corresponding initial magnetization curve. (b) Measured magnetic torque (open circles) and the corresponding fit (red) to a Fourier series. Adapted from reference [85].

high amount of domain wall motion with a smaller amount of energy applied through the external magnetic field. The opposite is observed within the dominating pinning contribution. In subfigure b), the torque measurement and the corresponding fit are shown. From the magnetic torque measurements and the fit, one can reliably deduce the magnetic anisotropy of ca. 1.67 MJ/m^3 for K_1 , which aligns with the derivation from the anisotropy field, which leads to an anisotropy constant of 2.38 MJ/m^3 . The maximum energy product $(BH)_{\text{max}}$ of the film is determined to be ca. 77.25 kJ/m^3 , which is very close to the $(BH)_{\text{max}}$ 78 kJ/m^3 of $\text{SmCo}_5/\text{Sm}_2\text{Co}_{17}$ nanocomposite powders prepared by intensive milling and annealing process [93].

SmCo₅ phase stabilization by substituting Cu

This subsection is based on the work published by G. Gkouzia, D. Günzing et al. in reference [94], where XMCD analysis leads to the observation of the decoupling of Sm and Co.

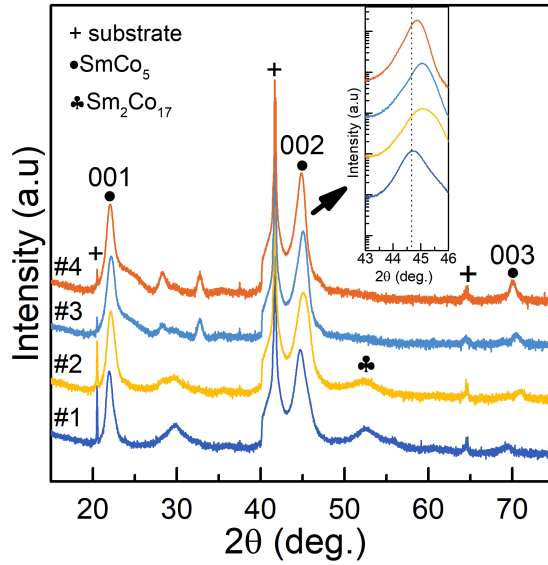
It has been shown that by adding Cu, the stability of the 1:5 phase increases by introducing Cu as an underlayer [95,96]. Here, Cu atoms are considered to have diffused from the underlayer into the SmCo_5 . Other authors also tried to deploy it while growing the thin film directly.

This section shows how Cu can stabilize the 1:5 phase and alter the magnetic properties of SmCo_5 . A series of thin films were produced with MBE in varying concentrations of Cu under identical conditions. This allows to separate the influences of the structure and composition on the magnetic behavior. By combining experimental and theoretical approaches, substituting Cu at the Co $3g$ sites stabilizes the formation of the SmCo_5 structure and enhances magnetic anisotropy and coercivity. This work focuses on the XMCD measurements, revealing that Cu substitution leads to increased decoupling of the Sm $4f$ and Co $3d$ moments. STEM images confirm that the predominant formation of phases is a 1:5 phase but unveiled nanoscale variations in the distribution of Cu and Co through the sample.

The fabrication of the sample was similar to the before-described MBE process, which Georgia Gkouzia conducted at the TU Darmstadt in the group of Prof. Alf. A series of $\text{SmCo}_{5-x}\text{Cu}_x$ films with different compositions, specifically with values of $x = 0.5, 1, 1.5, 2$ were created successfully. Giving us a broad range to study the impacts of Cu addition.

Figure 4.8(a) presents the XRD patterns of the $\text{SmCo}_{5-x}\text{Cu}_x$ film series grown on Al_2O_3 with a 001 orientation. 006 is the primary reflection of the substrate and is observed at an angle of 41.67° (marked by the plus sign). The use of a 001-oriented Al_2O_3 substrate promotes the growth of $\text{Sm}(\text{Co}, \text{Cu})_5$ films due to the matching lattice constants. The preferred orientation along the c -axis (easy uniaxial direction), as indicated by 00 l -type reflections.

Figure 4.8: (a) θ - 2θ XRD patterns of (#1) $\text{SmCo}_{4.5}\text{Cu}_{0.5}$, (#2) SmCo_4Cu , (#3) $\text{SmCo}_{3.5}\text{Cu}_{1.5}$ and (#4) SmCo_3Cu_2 thin films grown onto single crystalline Al_2O_3 substrate at 550°C . At 41.67° , the 006 reflection of the Al_2O_3 substrate is marked with the plus sign. From reference [94].



In the film with the lowest Cu content (#1 $\text{SmCo}_{4.5}\text{Cu}_{0.5}$), the primary reflection 002 of the SmCo_5 phase appears at 44.218° . The 002 reflection shifts towards higher angles with increasing Cu content, which undergoes a maximum at 45.106° . Further increasing the Cu content up to the highest Cu content results in the reflection shifting to lower angles. Simultaneously, the residual reflection from the $\text{Sm}_2\text{Co}_{17}$ phase decreases and vanishes with higher Cu content (the ♣ indicates this reflection). A non-linear shift in the peak position can be observed and explained as follows: The reduction in the 2:17 phase causes the peak to shift towards the 1:5 peak, as previously observed by Sharma et al. in reference [85]. Then, the increased Cu content shifts the peak back, consistent with Vegard's law. This is due to the slightly larger lattice constant of SmCu_5 . It is noteworthy that the phase purity of the 1:5 phase is notably higher compared to that of typical sputtered thin films. Nevertheless, reflections stemming from minor quantities of residual Sm-rich phases can still be detected at approximately 29° and 30° .

However, throughout the series, the overall microstructure consistently maintains a predominance of the 1:5 phase. The presence of the 2:17 phase is also observable in the HDAAF image (see figure 4.10a), as evidenced by the dumbbell pattern of atomic columns (similar to the structure depicted in figure 4.6 of the Cu-less thin film). Figure 4.10b) shows the energy-dispersive X-ray (EDX) measurement with elements represented in distinct colors to indicate their contributions. The elements are not evenly distributed across the entire film. Additionally, aluminum

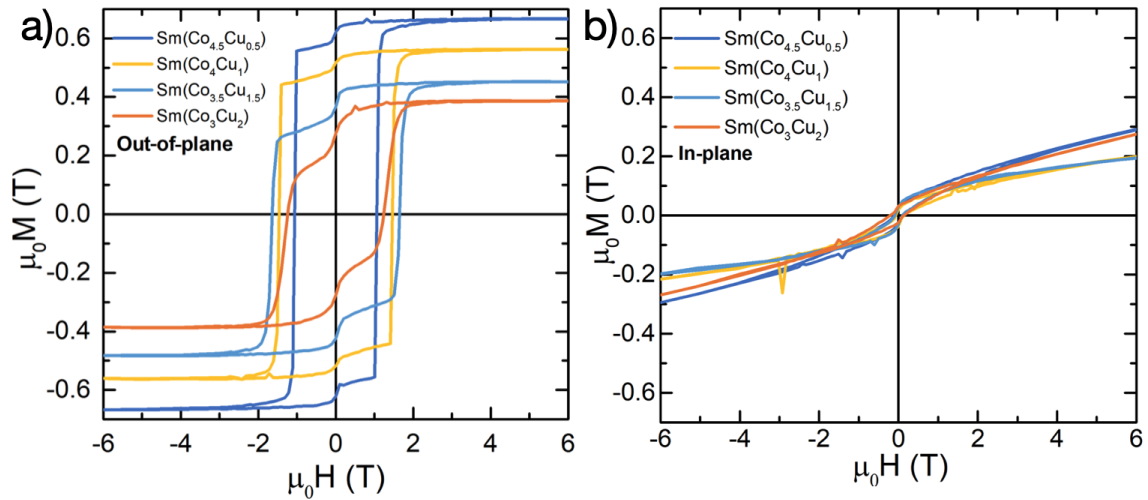


Figure 4.9.: a) Out-of-plane and b) in-plane macroscopic magnetometry measurement of the thin film series. Adapted from reference [94].

from the substrate diffuses into the first nanometer of the magnetic thin film. EDX measurements verify an absence of aggregation throughout the analyzed sample.

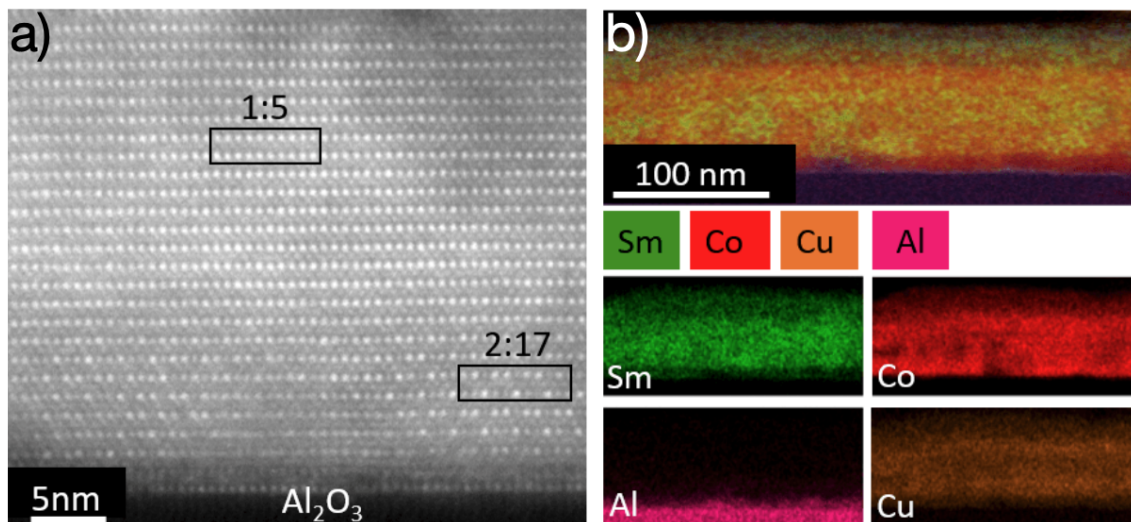


Figure 4.10.: a) High-resolution HAADF STEM image of the interface in the SmCo₄Cu thin film. b) EDX measurement with contributions from the individual elements. From reference [94].

The macroscopic magnetization loops set the stage for the elemental contributions obtained by XMCD hysteresis curves. Figure 4.9 depicts the macroscopic magnetization loops. All samples show an anisotropy perpendicular to the film surface, overcoming the magnetic shape anisotropy in magnetic thin films. In a), the out-of-plane direction is shown; in this direction, the easy axis lies parallel to the c-axis along the magnetization direction in this geometry. All samples show relatively large hysteresis above 1 T of coercive field. At 0 T, all samples show a jump-like behavior. The saturation and remanence decrease with increasing Cu content. Introducing the diamagnetic Cu at the Co sites influences the film's intrinsic properties. The coercive field increases first, having the maximum for the 1.5 Cu content sample. For the highest Cu content, the coercive field decreases again. Since that is a purely

extrinsic magnetic behavior, which is strongly dependent on the film's microstructure may be related to observed twin boundaries in these systems [97]. Subfigure b) shows the in-plane measurement along the hard magnetic axis; all films show similar behavior. At 6 T, the film is not saturated, which means that the film has higher anisotropy than that (compare SmCo_5 with an anisotropy field of ca. 40 T [24]).

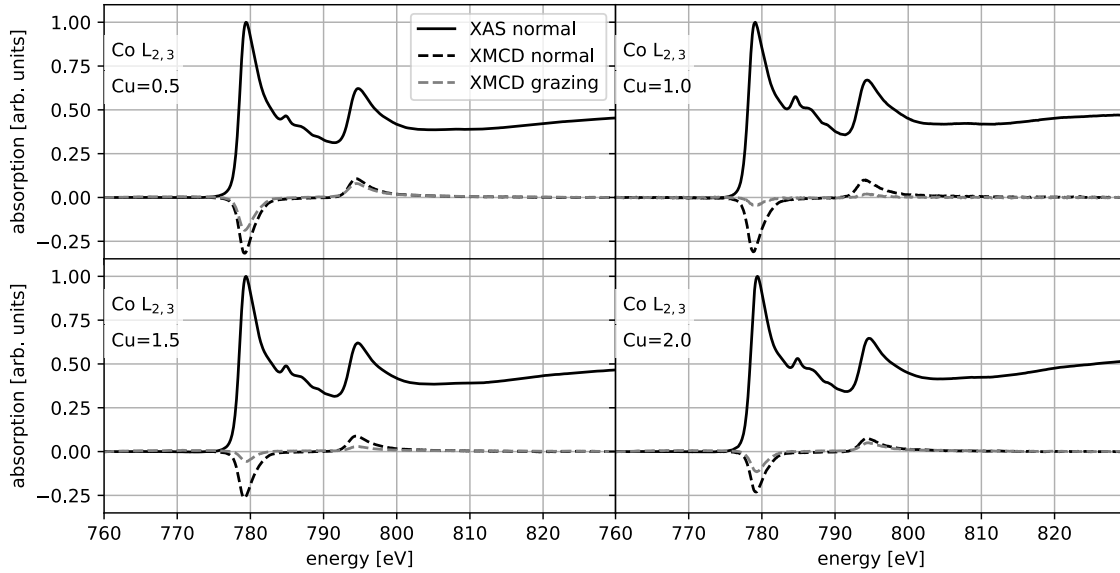


Figure 4.11.: XAS and corresponding XMCD at ambient temperatures and 1.9 T at the Co absorption edges of the whole thin film series with the stoichiometry $\text{SmCo}_{5-x}\text{Cu}_x$.

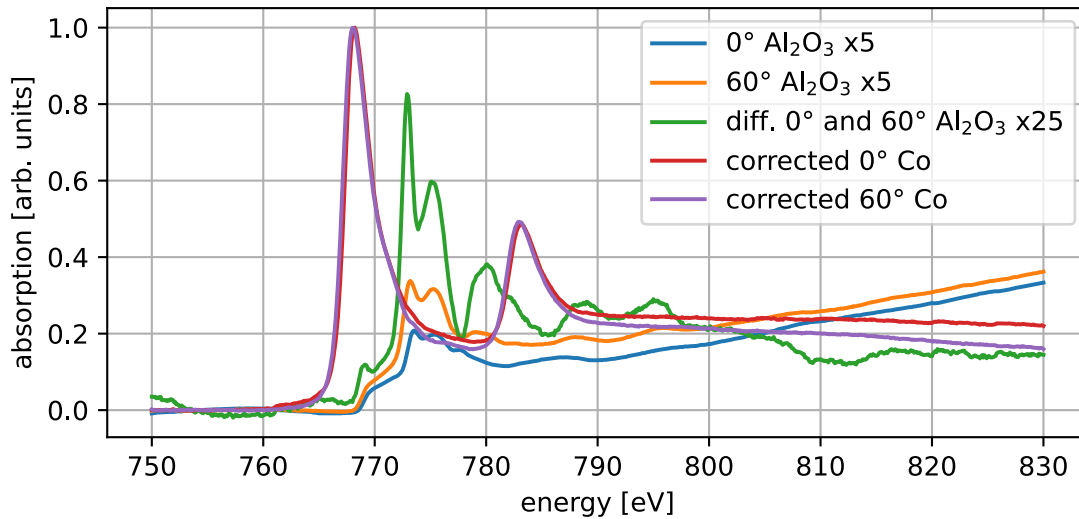


Figure 4.12.: XAS at the Co absorption edges of a film on Al_2O_3 at ambient temperatures showing the effects of the second harmonic of the synchrotron beam.

XMCD and XANES measurements were performed at the bending magnet beamline 6.3.1 at the ALS in Berkeley [98]. The software package xaspy [99] performed the element-specific measurement analysis. This free and open-source Python module

which helps to evaluate X-ray absorption spectra was developed during this Ph.D. thesis.

In the following measurements, the normal incidence is defined as 0° and grazing as 60° with respect to the sample surface normal. The samples were measured at the Sm $M_{4,5}$, Co $L_{2,3}$ and Cu $L_{2,3}$ absorption edges at 1.9 T applied magnetic field. The XMCD and XAS measurements at the Co $L_{2,3}$ -edges can be found in figure 4.11. The overall XAS has a similar shape for all measured samples. The feature between the L_2 and L_3 -edge is the second harmonic of the beam that appears from the Al K-edge. This absorption edge contributes to the overall XAS signal, but the magnetic signal of the sample is not disturbed. Figure 4.12 demonstrates this: The Al absorption edge and the EXAFS signal can be seen. The measurement was performed at two angles, which showed that there is also an angle dependence on the EXAFS signal at the Co edges, which arises from the Al K-edge resonance. This also shows the importance of comparing the normalization with the whitenline since the substrate and slight deviations can influence the edge jump. That restriction makes information about slight changes in Co electron-hole numbers impossible.

The XMCD signals at the Co L-edges are decreasing slightly with increasing Cu content in normal incidence, which means that there are slightly fewer spin-polarized d -state electrons. In grazing incidence, the XMCD signal almost vanishes with increasing Cu content, which can be explained by the following. In this measurement, the magnetic field was cycled from negative 1.9 T to positive 1.9 T at an angle of 60° . At this angle, the applied field is insufficient to switch the magnetic moments completely, and the magnetic moment is pinned in one direction. Therefore, no XMCD contrast can be observed. The small amount of the 2:17 phase could also be responsible for the smaller XMCD. The 2:17 phase shows a smaller anisotropy. The anisotropy within the sample is significant, and at roughly 2 T applied field, the magnetization cannot change from the one easy axis energy minimum into the other minimum.

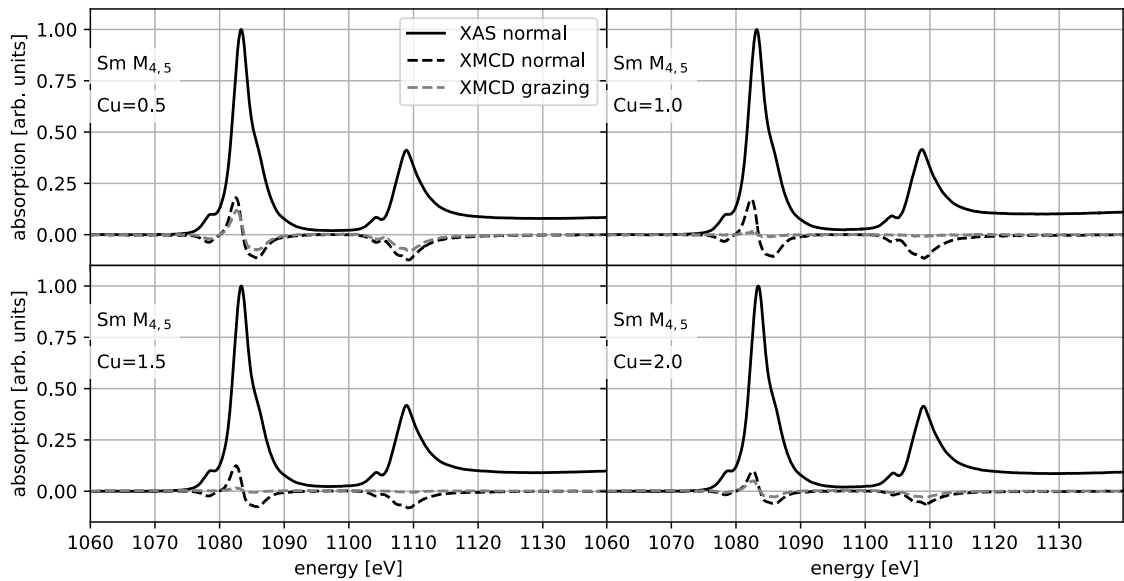


Figure 4.13.: XAS and corresponding XMCD at ambient temperatures and 1.9 T at the Sm absorption edges of the whole thin film series.

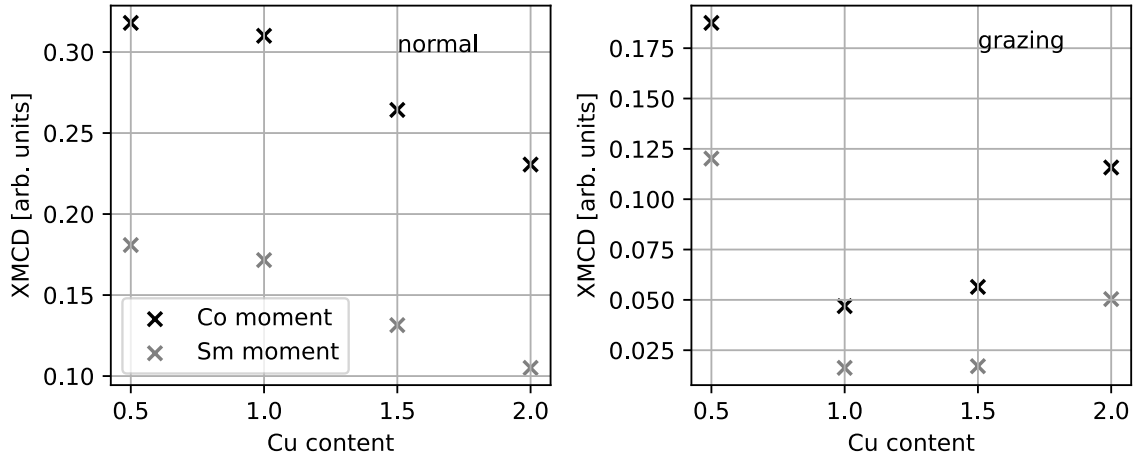


Figure 4.14.: XMCD intensities normalized to the whiteline at the Co L_3 -edge and Sm M_5 -edge absorption edges of the whole thin film series in normal and grazing incidence.

Similar behavior can be seen at the Sm $M_{4,5}$ -edges in figure 4.13. Similar to the behavior of the Co edge, the XMCD reduces with increasing Cu content in grazing incidence. The XMCD finds a minimum at roughly SmCo_4Cu_1 . This is also depicted in figure 4.14, where the XMCD is plotted versus the Cu content. The XAS at the Sm $M_{4,5}$ -edges shows a clear sign of $3+$ ($4f^5$). Unlike at the transition metal edges, the oxidation state at the RE metals is no sign of magnetization or oxidation. Only the Sm XMCD's reduced signal concerning the XAS indicates the level of oxidation. This can influence the estimation of the spin and orbital moments, which will be discussed in the following paragraph.

Figure 4.14 shows the comparison between the XMCD spectra maxima at both edges and both incident angles. The previously described decrease in intensity for the normal incidence measurement can be observed. While some argue that the magnetic moments would vanish for SmCo_2Cu_3 [102], others report high coercivity for this compound [103]. The presented measurements indicate that the sample with stoichiometric formula SmCo_4Cu_1 has the highest anisotropy within the sample series.

At which crystal position the Cu is substituted is still unknown. While there are calculations on preferring the Co $3g$ site [104], other calculations suggest an occupation of the Co $2c$ sites [105]. Our density functional theory (DFT, performed by Ruiwen Xie at TU Darmstadt at the group of Prof. Zhang) calculations indicated that SmCo_4Cu_1 with Cu at the $3g$ exhibits higher single-ion anisotropy compared to pure SmCo_5 .

Monte Carlo simulation for sum rules and discussion of the magnetic dipole term $\langle T_z \rangle$

Magneto-optical sum rules have a long track record of determining the magnetic moments of an atom from XMCD data [59, 106–110]. Usually, sum rules are carried out for only one set of parameters, which are heavily influenced by the bias of the person analyzing multiple parameters and are sensitive to the overall result, as shown in this analysis.

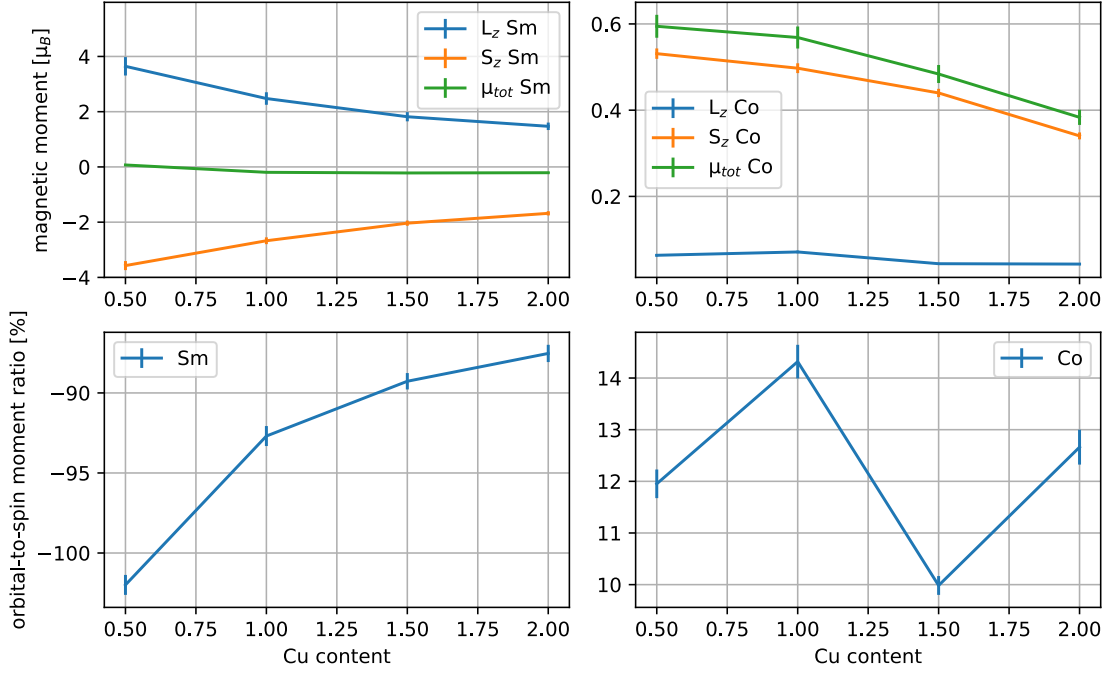


Figure 4.15.: Magnetic moments derived from sum rules and orbital-to-spin ratio for Sm and Co calculated for all measured samples.

This thesis will estimate the error using a Monte-Carlo calculation as a 'robustness check'. This check is included in the software package xaspy version 0.3.3 and described in the following sentences. The advantage of using a Monte Carlo approach is not to avoid the general error in utilizing the magneto-optical sum rules [109]. It can rather be interpreted as a robustness test or check of the analysis. By taking multiple parameters and doing multiple sum rule analyses per measurement, one can reasonably estimate the error of the subjective analysis method. It does not account for the error from oxidation layers or beam specifications like polarization, which usually reduces the measured XMCD compared to the white line. The sum rule analysis can be found in figure 4.15 for all samples. The magnetic dipole term has been neglected while performing these calculations. The magnetic dipole term and its implications will be discussed later. The magnetic dipole term directly influences the spin magnetic moment and all derived quantities like the total magnetic moment and the orbital-to-spin magnetic moment. The derivation of the sum rules for $3d$ and $4f$ system and how the magnetic dipole term $\langle T_z \rangle$ influences the result can be found in appendix A. It can be seen that the total magnetic moment decreases for Sm as well as for Co with increasing Cu content. One can see that the orbital and spin moment is roughly the same for the Sm. The orbital is decreasing from around -100% to about -87%. The negative sign shows that the orbital and spin magnetic moment are aligned antiparallel, as expected by Hund's rule of maximum multiplicity. The Co orbital-to-spin ratio fluctuates around ca. 12% with increasing Cu content, with no visible trend. Since the luminescence of the Al K-edge line contributes to the overall XAS, it is the major source of error for the determination of the magnetic moments in the Co.

In figure 4.16, one can see the Monte Carlo simulation of the sum rule analysis for different $\langle T_z \rangle$ with a little room for the other parameters like the position of the

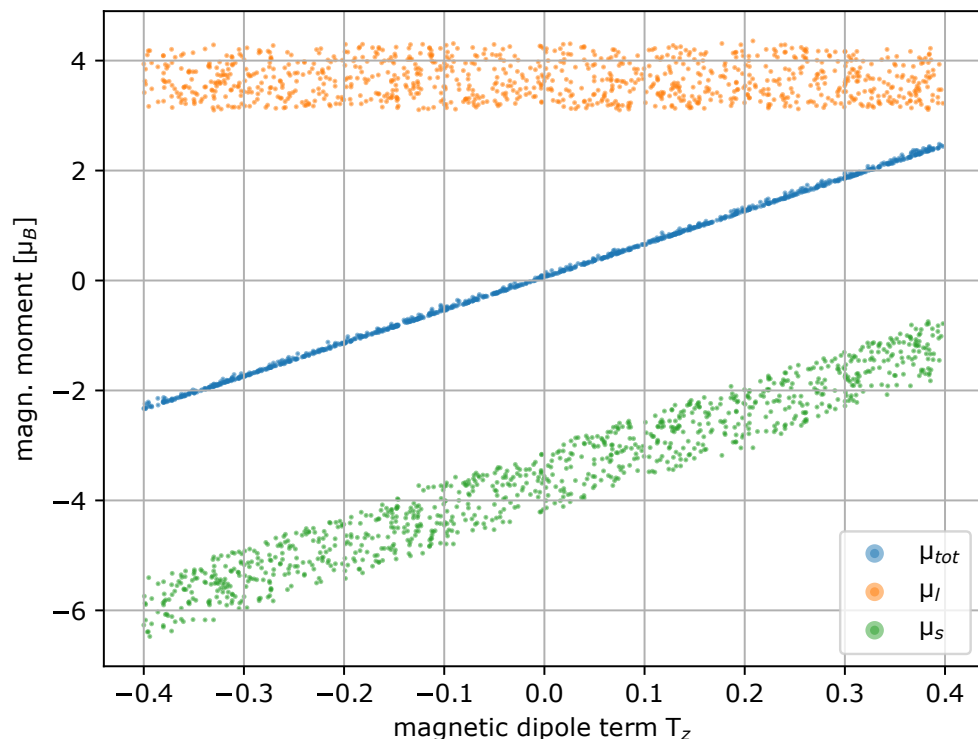


Figure 4.16.: Sum rules applied to different analysis runs with different $\langle T_z \rangle$ applied for the sample $\text{SmCo}_{4.5}\text{Cu}_{0.5}$.

step function and points chosen for integration of the signal. The figure shows that the μ_l and μ_s are relatively broad in the error, but in the μ_{tot} , the error vanishes. This shows that the measurement of the total moment can be very exact from the analysis if the dipole magnetic dipole tensor is defined.

In Sm, the deviation between the sum rules and multiplet calculations result is the largest of all RE metals and reaches around 230% [106]. Teramura et al. calculated for L_z -4.249, for S_z 1.749 and T_z -0.385, which yields a total moment of ca. $0.751 \mu_B$ and orbital-to-spin moment ratio of ca. -120%, a therefore higher orbital moment. The present calculations find a smaller orbital moment than the spin moment. Figure 4.17 shows the calculation for the orbital-to-spin moment with $\langle T_z \rangle$ as an open parameter. The spin magnetic moment of the Sm is strongly dependent on the used $\langle T_z \rangle$ and, therefore, is the orbital-to-spin magnetic moment. One can see that with increasing $\langle T_z \rangle$, the spin moment reduces, which increases the orbital-to-spin ratio. From the negative sign of the ratio, Hund's rule can be verified partially. It states for Sm that spin and orbital moment are in absolute values precisely the opposite. The moments are not the same for most $\langle T_z \rangle$ values. With a $\langle T_z \rangle$ of roughly 0, Hund's rule can be verified for this sample. The magnetic dipole term $\langle T_z \rangle$ is challenging to measure and has an anisotropic property. Therefore, it is difficult to finally define from XMCD if the coupling within the Sm is ferri- or ferromagnetic as different sources project [111,112]. Assuming a small negative magnetic dipole term, an anti-parallel coupling between the Sm and Co can be confirmed in all samples. With even larger negative $\langle T_z \rangle$, the coupling remains anti-parallel. The presented sample

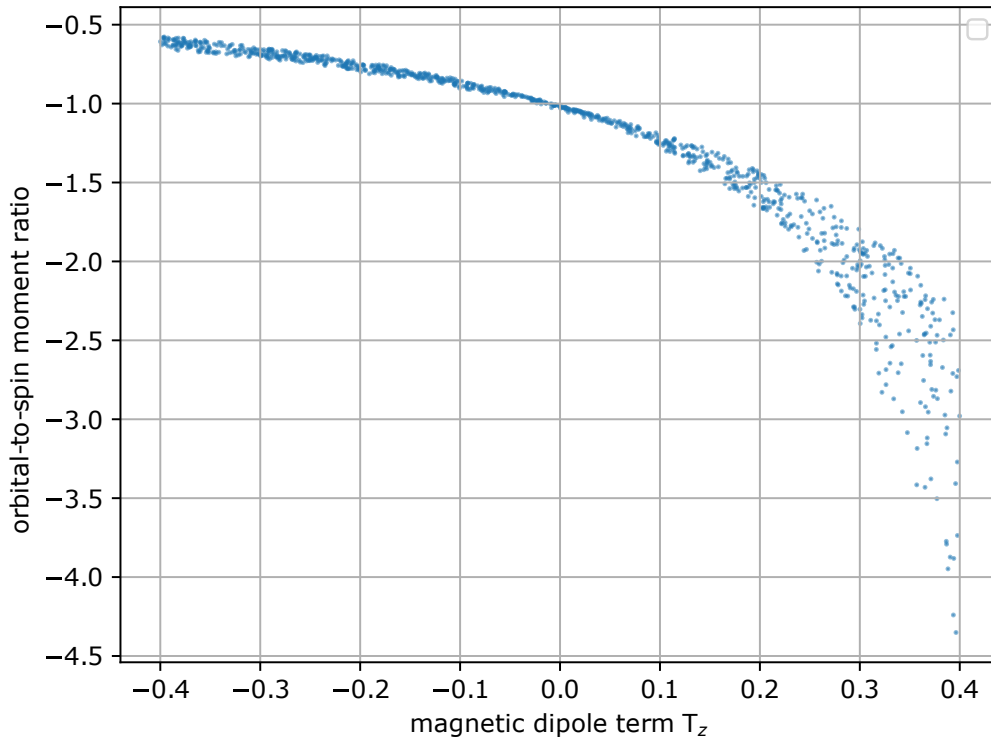


Figure 4.17.: Orbital-to-spin ratio for Sm and Co calculated using sum rules with different $\langle T_z \rangle$.

is the only sample where the net magnetic moment is slightly positive on the Sm with neglecting the magnetic dipole term $\langle T_z \rangle$ (compare figure 4.15).

Induced Cu moment

It is known that an induced moment in Cu can exist and was observed in other systems. For example, in thin magnetic layers of Co/Cu/Co [113], spin injection from an adjacent Co layer [114]. It was impossible to measure a magnetic moment on the Cu $L_{2,3}$ -edges by XMCD in the same measurement procedure used earlier: at room temperature and fields up to 1.9 T. A magnetic moment could not be found on the Cu atoms. Since the moment would be an induced moment, it is expected to be very small and could be overshadowed by the Cu capping layer, which contributes to the overall spectrum as a non-magnetic signal.

Element-specific hysteresis curves

To observe how the individual elements in the magnetization reversal process, element-specific hysteresis curves have been recorded at ambient temperatures at 2 T. Since the measurements were performed at a bending magnet beamline, it was only measured with one circular polarization, and the magnetic field change was recorded. The previously described XMCD minima and maxima energies have been used for the measurement. The element-specific hysteresis loops can be found

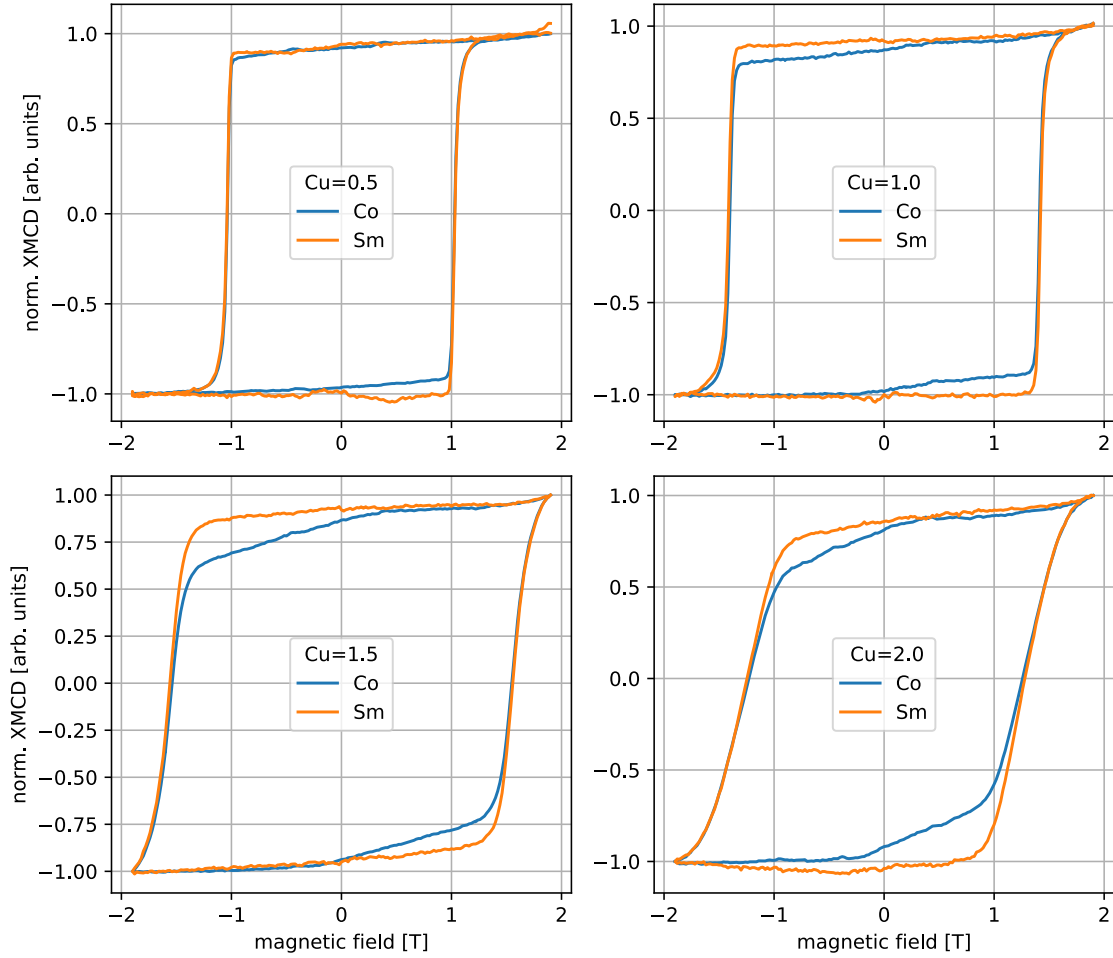


Figure 4.18.: Element-specific hysteresis curves measured at the Sm and Co-edges for increasing Cu dopant concentrations.

in figure 4.18. For the 0.5 Cu sample, the area between both curves is small or non-existent. It can be seen that the area is larger in the fourth quadrant of the hysteresis loop compared to the second quadrant, which could be due to a measurement artifact or error from the permanent magnet since the hysteresis loop should be symmetric for the second and fourth quadrant. Increasing the Cu content, the hysteresis loops also lose the rectangular shape, going more towards a rounded shape. The differences in the Co and Sm edge hysteresses increase with increasing Cu content, which could be interpreted as the additional Cu decoupling the magnetism between the Sm and Co. Although no indication was found in the measurement for Co segregation, a higher ratio of weaker ferromagnetic Co would lead to similar behavior of the element-specific macroscopic hysteresis loop.

Judging by the loops' squareness, the thin films are transitioning from nucleation to pinning type reversal mechanism with increasing Cu content. Figure 4.19 shows the extracted values of the element-specific hysteresis curve. Figure a) depicts that the overall magnetic hysteresis area increases with increasing Cu content. The maximum is at 1.5 Cu and then decreases to almost the same values as the 0.5 Cu content for both measured elemental contributions. Figure b) depicts the difference in hysteresis area; the decoupling increases linearly with increasing Cu content. Figure 4.19c)

illustrates the coercive field with increasing Cu content. The hysteresis and coercive field show a similar inverse U-shape behavior, with a maximum of 1.5 Cu.

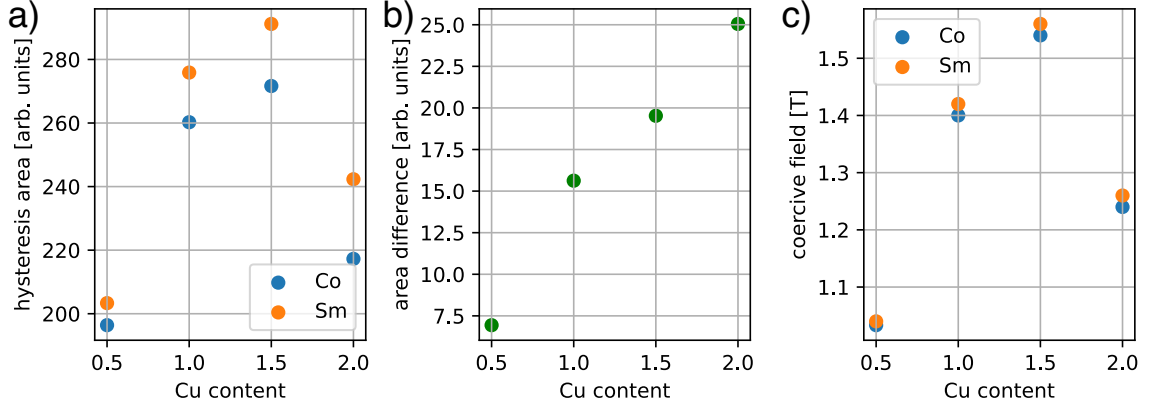


Figure 4.19.: Derived values from the element-specific hysteresis curves, like a) hysteresis area of Co and Sm, b) are difference between the Co and Sm signal, and c) coercive field for Co and Sm hysteresis loops.

Comparing the values obtained from the hysteresis loops with those from the XMCD spectra, one can observe that the coercive field dependence derived from the hysteresis loops behaves like XMCD grazing incidence measurement. Since the moments do not flip entirely due to only applied 1.9 T magnetic fields, this can be linked to a higher anisotropy of the film with 1.5 Cu.

4.2. Electronic and magnetic structure of (Y, Ce)Co₅

The element Ce is an interesting dopant to study due to its electronic properties and abundance within the earth's crust [115,116]. It is known that the valency of Ce can be found in mixed valence states [117,118] in Ce-oxides as well as in intermetallic compounds [119,120]. Wohlleben and Röhler suggested that the valency of Ce can be estimated using L₃-edge X-ray absorption measurements rather than volume in metallic systems [121]. Nordstrom et al. calculated a non-negligible moment for spin and orbital moment in Ce in CeCo₅, which would manifest the existence of itinerant moment in Ce in CeCo₅ as well [122]. The magnetic moment could be observed in the itinerant *d* with XMCD [123]. Wang et al. studied the magnetic response via XMCD in the system Ce₂Fe₁₄B, observing a total magnetic moment on the Fe of ca. 3.12 μ_B and Ce 0.100 μ_B . The main contribution in the Ce moment can be attributed to the well-localized 4*f*¹ electronic states [124].

(Y,Ce)-Co thin film systems

The double peak structure in the hard X-ray spectra in figure 4.20a) can be attributed to the Ce 4+ (4*f*⁰) oxidation state. The two peaks originate from two different screening mechanisms: The low-energy structure is obtained when a 4*f* electron effectively screens the core hole in the final state. The higher energy structure (about 6–10 eV higher) arises from inadequate screening by the 5*d* electron.

This is possible due to the hybridization with the conduction band [120, 125]. The soft X-ray spectra were collected at beamline PM3 at BESSY II [126]. The hard X-ray spectra have been recorded at the beamline 20-ID at the APS [127].

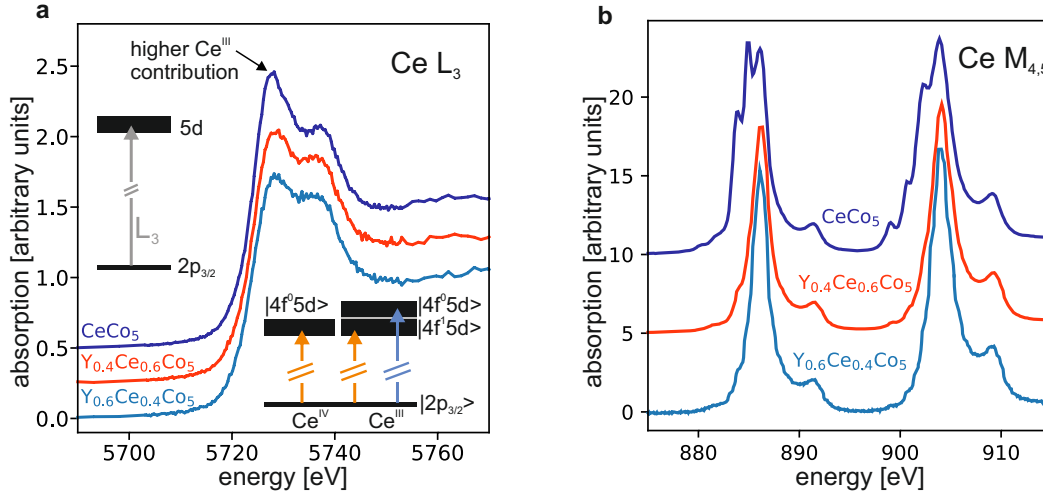


Figure 4.20.: XAS of three (Y, Ce)Co₅ thin films measured at the a) L₃ and b) M_{4,5}-edges.

The thin film measurements at the soft and hard X-ray absorption edges will be compared next. A larger contribution of oxidation state 3+ ($4f^1$) for Ce can be found in the pure CeCo₅. Figure 4.20 b) displays the different measured soft X-ray spectra. Figure 4.21 shows multiplet calculations, which look comparable with the measured spectra. These spectra were recorded with the surface-sensitive total electron yield detection mechanism, which leads to a higher contribution of a probably oxidized surface below the capping layer. Therefore, there is the possibility that especially the (Y, Ce)Co₅ films are already oxidized, resulting in a dominant 4+ ($4f^0$) contribution in the soft X-ray spectra.

The multiplet calculations give the possibility to also simulate the magnetic moment on the Ce and the XMCD spectra, which shows only a magnetic signal from the Ce on the 3+ ($4f^1$) oxidation state; the XMCD is non-zero. Suppose a tetra-valent state is assumed; no magnetic signal can be observed. The electron from the $4f$ becomes itinerant. The atomic multiplet calculations use Quanty with an applied magnetic field of 1 T [128]. Under the assumption that the $4f$ electrons are strongly localized, no strong additional crystal field is present. For simplicity, no $4f$ ligand hybridization, ligand to metal charge transfer assumed, and no exchange field. The shoulder in the experiment at slightly higher energies than the absorption edge could not be reproduced with the Quanty multiplet calculations. This shoulder is attributed to ligand hole contributions to the $4f^0$ ground state [129].

With these results, a direct correlation between the $4f$ states, and the spectra of the hard X-ray region at the L₃-edges by comparing the same thin film with the measurements from the soft X-ray region and our simulations could be found. Since Ce is known to be a very reactive element, the thin film capping was insufficient until the XMCD measurements could be performed with the previously described luminescence detection technique to get a clean signal. Here, larger capping would increase oxidation resistance and still be suitable for luminescence yield measurements.

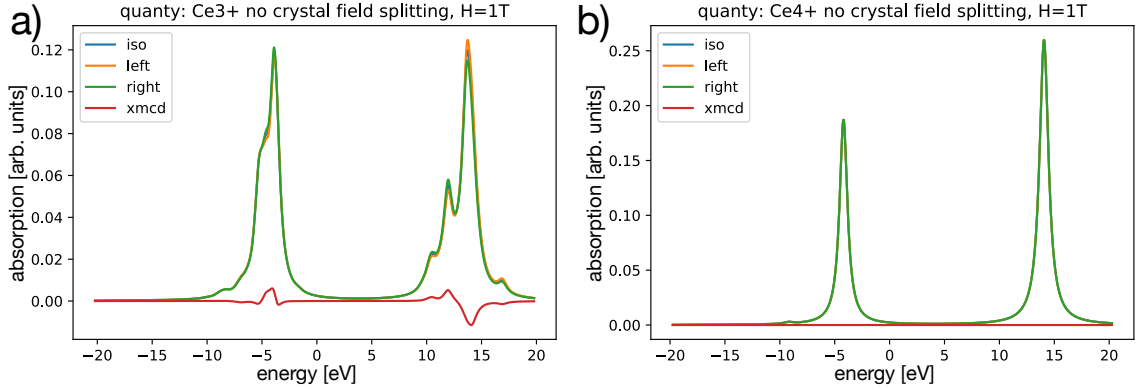


Figure 4.21.: X-ray magnetic circular dichroism (XMCD) calculation for a) 3+ ($4f^1$) and b) 4+ ($4f^0$) oxidation state with calculated XMCD signal.

(Y,Ce)-Co bulk systems

This section transfers the knowledge and the techniques used in the previous section from the thin films to the bulk. X-ray-based techniques investigate a bulk sample series of (Y, Ce)Co₅. The previous section analyzed magnetic thin films in the hard and soft X-ray region better to understand spectral features and the corresponding electronic structures. Within the approach presented in this section, this knowledge will deduct information from single crystal (Y, Ce)Co₅ bulk samples.

In figure 4.22, the Curie temperature of (Y, Ce)Co₅ sample series can be seen. At 0% Ce, the Curie temperature is around 975 K, which decreases to around 700 K for 100% Ce. The peculiarity of this system can be seen at around 50-60% of Ce substitution, where the Curie temperature suddenly decreases.

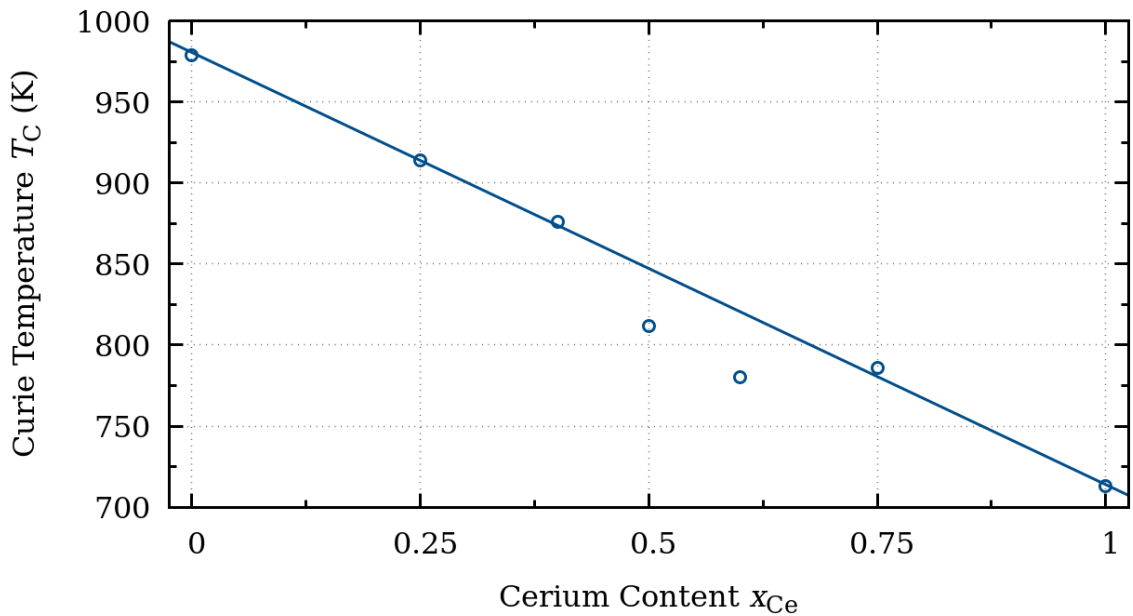


Figure 4.22.: Curie temperature measurements of the (Y,Ce)Co₅ bulk samples. The drawn line acts as a guide to the eye. From S. Giron at TU Darmstadt.

Short-range order can be a good approximation to investigate the Ce valency [130]. To get the short-range order of a compound, the previous sections showed that

EXAFS measurements are a proven tool. The EXAFS measurements for the bulk material can be found in figure 4.23a). During the analysis, the first Co-Co path was used to estimate the next neighbor for the fitting procedure via *FEFF* calculations. The Fast Fourier transform (FFT, see figure 4.23a)) of the background corrected $\chi(k)$ is directly related to the bond length between the absorbing atom and the next atomic neighbors. This first shell (neighbors at the closest distance) contains most cobalt atoms. In a minority, the rare earth (RE) atoms are present. The first shell contains several distances from about 2.46 (2c - 2c and 2c - 3g distances) to 2.84 Å (3g - 3g distance). To obtain the real distance to the first shell of the $Y_{1-x}Ce_xCo_5$ systems, the Co-Co paths were fitted from *FEFF* and the software package *larch* using a $CeCo_5$ structure [45,47]. Since the presence of RE elements has a low impact on the overall spectra, estimated from the calculations, the RE path was neglected. As the diffraction measurements suggest, the samples exhibit long-range ordering and order properties on the local scale. EXAFS measurements show a deviation of the mixed sample $Y_{0.4}Ce_{0.6}Co_5$ to the upside of the overall trend within the measured series, although significant errors are present.

The lattice parameter and, therefore, the next neighbor can also indicate the valence state, as in the 3+ ($4f^1$) state; more volume is needed since an additional electron is closer to the Ce. Therefore, the Co-Co distance increases as an indication of the valency. Although the distances between Ce would be a better indicator, a reasonable signal during the measurements could not be obtained.

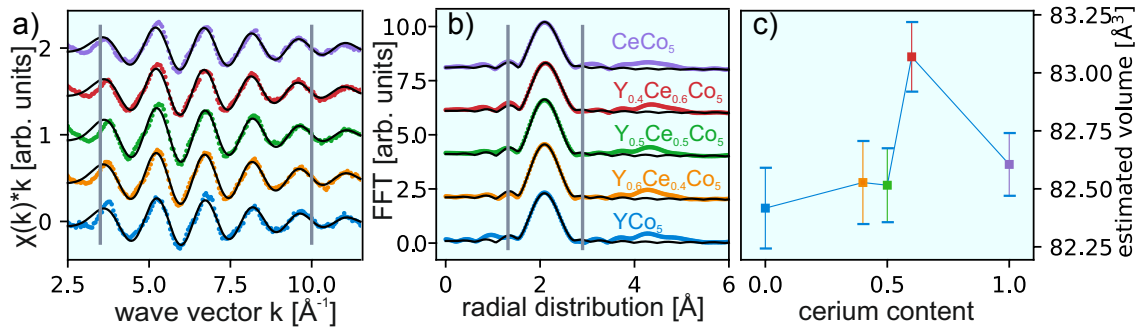


Figure 4.23.: EXAFS and corresponding fit for the first Co-Co scattering path of the (Y, Ce) Co_5 bulk samples.

The larger lattice can be observed in XRD measurements as well. Figure 4.24 shows the lattice parameters a , c , and the corresponding volume when the Ce content is increased.

Figure 4.3a) shows the structure of the 1:5 phase. The lattice parameter a lies within the picture plane, where the Co atoms contribute more. There are fewer first-scattering Co-Co paths within the out-of-plane direction. This explains a higher sensitivity with the EXAFS measurements to the behavior one can observe in the lattice parameters measured by XRD.

We can thereby correlate that with increasing Ce content at around 50-60%, there is an unusual increase in 4+ ($4f^0$) states due to the one f electron close to the core getting itinerant, increasing the lattice parameter. The itinerant electron will then not contribute to the magnetic moment of the Ce anymore, which correlates to a drop in Curie temperatures in these systems. Materials with a higher intrinsic magnetic moment are often associated with unpaired electrons in their electronic

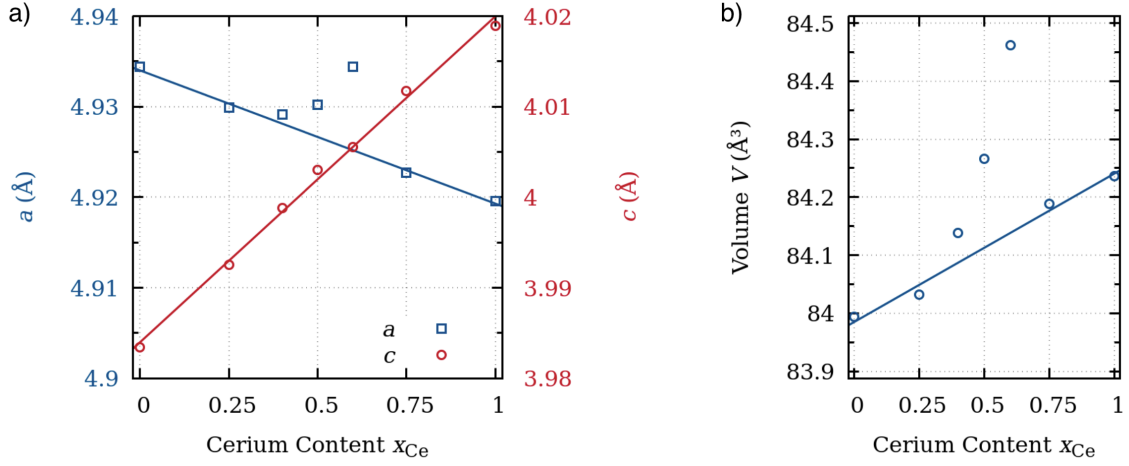


Figure 4.24.: a) from XRD derived a and c lattice constants and b) calculated volume of $(Y, Ce)Co_5$ bulk series. From S. Giron at TU Darmstadt.

configurations. They usually tend to have higher Curie temperatures. The stronger magnetic interactions between neighboring atoms or ions are more resistant to thermal disruption. Therefore, the lattice constant and the distance-dependent exchange coupling between the Ce and Co could affect the Curie temperature.

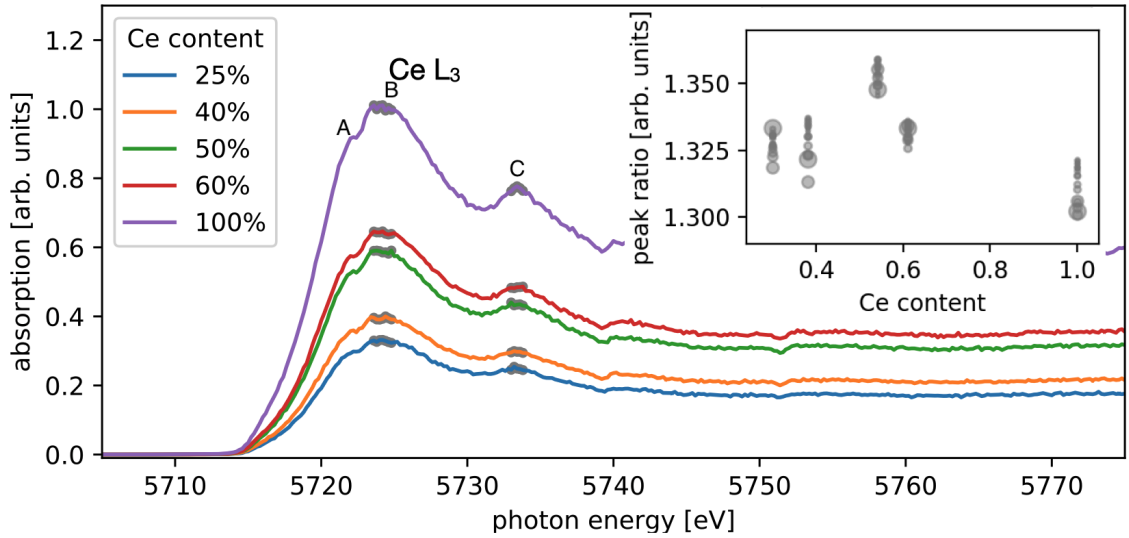


Figure 4.25.: HERFD spectra of the $(Y, Ce)Co_5$ bulk samples. The inset describes the ratio of the first to the second peak, or feature B to C.

However, the measured HERFD data shows the opposite picture if interpreted in the following way: In figure 4.25, one can see the measured HERFD spectrum for the samples collected at beamline BM20-ROBL at the ESRF [131]. It is similar to the hard X-ray spectra shown in figure 4.20 for the thin film systems. In HERFD, the resolution is higher, so the identification of smaller features within the spectrum is possible. For example, the subtle in-edge peak marked by an A was not visible within the previous XAS measurements due to the broadening of the transition line. The in-edge peak A could also resolve from an artificial monochromator malfunction and is therefore not further discussed. The main absorption peak is marked with a B. The second main peak marked with the C is due to the $4+$ ($4f^0$) oxidation state

nature of the Ce, as described in the previous paragraph. No pre-edge peak can be observed as it was seen in Ce-oxides, and are attributed to transitions into the $5d$ states [132]. The inset within the figure describes the feature B to C for slightly different energy points chosen. One can see a slight decline, with a little increase at 50% and 60% Ce content. This can be attributed to the higher number of $4f^1$ states within this sample compared to the other ones, which would be contradictory to the results from the lattice parameters and short-range distances, which were discussed before. On the other hand, it could be that the $5d$ states are distributed differently due to the different crystal distances, which we observe via EXAFS and XRD.

5. Interaction domains in Nd₂Fe₁₄B studied in three dimensions

This chapter is mostly based on the to be submitted manuscript: *Insights into hot-deformed anisotropic Nd₂Fe₁₄B magnets: Interaction domains studied by non-destructive 3D magnetic laminography and magnetometry*

Understanding the coupling mechanisms involved in state-of-the-art permanent magnet Nd-Fe-B is an ongoing task in designing high-performance nanocrystalline hard magnetic materials. This requires evaluating how extrinsic properties play with intrinsic magnetic properties. Understanding the usually complex domain structure of Nd-Fe-B has long been of interest [133–135]. Our study focuses on the extrinsic properties, describing the domain structure in three dimensions by probing the magnetic moment in a highly textured Nd₂Fe₁₄B model system. In this system, so-called interaction domains are crucial in macroscopic magnetic behavior. Interaction domains extend over multiple grains and are coupled magnetostatically through a few nm thin paramagnetic regions. Additionally, exchange coupling is present on the short-length scales. This behavior was first observed in iron nanoparticles embedded in a non-magnetic matrix using the Bitter technique [136]. The properties of these interaction domains and their spatial and magnetic dimensions play a crucial role in understanding magnetic reversal processes in nanocrystalline and nanogranular magnetic materials [137].

Interaction domains are present in many prepared Nd-Fe-B systems [137–141], as well as in Sm-Co-based systems [142]. This work studies hot-deformed Nd-Fe-B permanent magnets, which are comparable with ones investigated by Thielsch et al. [140], Hioki [141] and Khlopov et al. [138]. In the previously mentioned studies, the authors used surface-sensitive techniques like magnetic force microscopy (MFM) to study the interaction domain structure. In these studies, extensive work was performed in the demagnetized state and at various applied magnetic fields to observe the process of magnetic reversal. These two-dimensional techniques generally lack the representation of the entire bulk image, which is essential to exclude the surface demagnetization field and surface effects. It is known that, especially in softer magnetic materials, these effects lead to differences in the domain structure at the surface versus in the bulk. Flux closure domains can form at the material's surface to reduce the stray field. X-ray magnetic circular dichroism (XMCD) microscopy is a powerful, non-destructive tool to study the surface of the permanent magnet [143–145]. But, using this non-destructive X-ray-based technique XMCD with high energy photons in combination with laminography, one can extend the information from the sample surface to insights into the 3D magnetic structure. The ability to depict complex magnetic structures with this method in all spatial directions has become more prominent over the last few years [69, 70, 75, 146–149]. Very

recently, the first 3D visualization of a single particle of a sintered permanent Nd-Fe-B magnet was shown by Suzuki et al. [150] with a similar technique. Takeuchi et al. applied fields during their measurements, observing the magnetization reversal process in real-time very recently [151], with grains in the μm range. This work presents the first 3D magnetic representation of a hot-deformed nanocrystalline anisotropic Nd-Fe-B permanent bulk magnetic sample, with grain sizes of a few 100 nm and domain widths of about 900 nm.

5.1. Sample system and preparation

The chosen sample family is as previously mentioned, the well-known system Nd-Fe-B, which usually arises from three different tertiary phases in the phase diagram: (i) the tetragonal Φ -phase $\text{Nd}_2\text{Fe}_{14}\text{B}$ (most important for magnetism and used in this studies primarily), (ii) the orthorhombic η -phase $\text{Nd}_{11}\text{Fe}_{40}\text{B}_{40}$ and (iii) the rhombohedral ρ -phase $\text{Nd}_5\text{Fe}_2\text{B}_6$. At 1180 °C, the critical phase for permanent magnets is formed: tetragonal Φ -phase $\text{Nd}_2\text{Fe}_{14}\text{B}$. The structure is shown and described in figure 5.1.

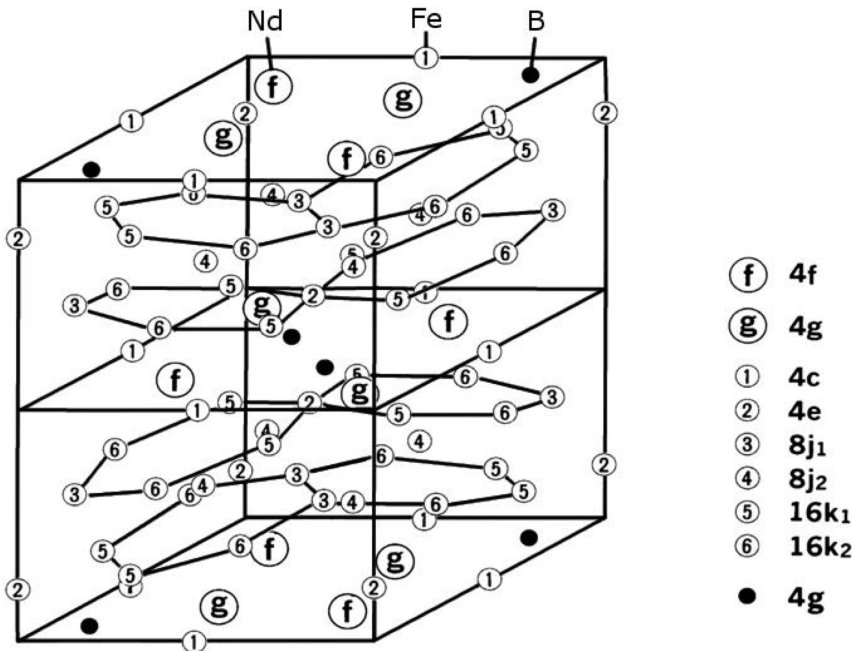


Figure 5.1.: Atomic structure of $\text{Nd}_2\text{Fe}_{14}\text{B}$. C-axis (magnetic easy axis) pointing up. Adapted from reference [152].

The tetragonal unit cell of Φ -phase $\text{Nd}_2\text{Fe}_{14}\text{B}$ consists of atoms arranged in a specific structure. The crystal lattice is a hexagonal close-packed (HCP) crystal structure with a space group of $P4_2/mnm$ [153]. The unit cell consists of 68 atoms, with 8 Nd atoms, 56 Fe atoms, and 4 B atoms arranged in the following structure: The Nd atoms occupy the 4f and 4g Wyckoff positions, the Fe atoms occupy the 4c, 4e, 2 times 8j, and 2 times 16k Wyckoff positions, and the B atoms occupy the 4g Wyckoff positions. The crystal structure has a conventional lattice constant of approximately 8.78 Å for a and b lattice constants, with a ratio of $c/a \approx 1.4$. The lattice is ordered ferrimagnetically with a net magnetic moment of ca. $31.30 \mu_B/\text{f.u.}$,

raising from Nd and Fe from 8 unique magnetic sites. The magnetic easy axis aligns along the c -axis in the lattice (pointing up in the described figure).

The magnetically important Fe $3d$ states are interatomic exchanges coupled with the Nd $5d$ electron states. Therefore, they are a good indicator of the unit cell net magnetic moment direction and magnitude. By tuning the energy of the left and right circularly polarized light at Nd L_2 -edge energy, the magnetization projection of the XMCD contrast at the Nd $5d$ electron states can be probed. The magnetic contrast is larger at the Nd L_2 -edge than at the TM Fe K-edge [154].

The samples discussed in this chapter were prepared in the group of Prof. Gutfleisch at the Technical University of Darmstadt. All of the discussed samples have in common that their magnetic domains consist of interaction domains (explained in the next paragraph) with different grain sizes: single-phase Nd-Fe-B ribbons with 100-200 nm isotropic equiaxial grains, Nd-rich melt-spun ribbons with 100-200 nm isotropic equiaxial grains, hot-deformed (die-upset) variation of the second sample with highly textured grains of high aspect ratio (100x500 nm), and a hot-pressed sample with in general larger domain sizes. The following paragraphs will describe the last sample with the high texture in more detail. This work will focus mainly on the anisotropic-prepared (hot-deformed) sample. This sample showed the most three-dimensional magnetic contrast in the laminography measurements.

Interaction domains

Craik and Isaac (1960) were the first to describe the interaction domain phenomenon in mercury-embedded iron nanoparticles. The nanoparticles, around 15 nm, exhibited magnetic domains much larger than their grain sizes when observed using the Bitter technique. The samples displayed a shape and magnetization reversal behavior similar to uniaxial materials but with lower energy associated with division due to the long and narrow interaction domains compared to regular domains [136].

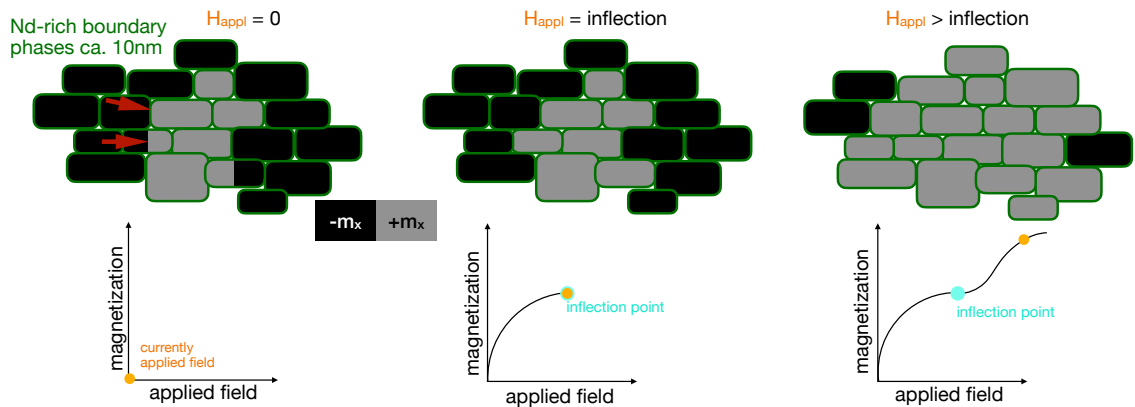


Figure 5.2.: Schematics of the magnetization reversal in a sample with dominating interaction domains including multi-domain grains. The red arrows indicate a single- and multi-domain particle domain wall.

The domain structures of the surface of Nd-Fe-B systems have been studied quite extensively over the recent years [133–135]. Magnetic microstructure in die-upset melt-spun Nd-Fe-B magnets also displays cooperative phenomena resulting from magnetostatic interaction observed by Khlopkov et al. [138]. The formation and

size of these interaction domains are highly dependent on the degree of texture that arises due to varying degrees of deformation. Optical Kerr-microscopy studies reveal that interaction domains are undetectable in cases of low degree of texture. In a subsequent study, the magnetic interaction domains were compared in thermally demagnetized and DC-demagnetized states [137]. In the DC-demagnetized state, the interaction domains are much smaller, while in the thermally demagnetized sample, the maze-like larger structure is visible. This could come from more considerable magnetic frustration during the heating and cooling process. Later, Woodcock et al. conducted measurements in highly textured Nd-Fe-B thin film systems, where they observed and discussed interaction domains concerning the grain size compared to the single domain particle size and to sample texture [139]. Thielsch et al. published three years later an in-situ magnetic force microscope study of the magnetization reversal of interaction domains in hot deformed Nd-Fe-B magnets [140].

Interaction domains have different physical properties concerning classical domains in uniaxial magnetic anisotropic systems. In some Nd-Fe-B-based samples, where interaction domains occur, a few nm thick grain boundary of an Nd-rich phase separates the different grains. The paramagnetic boundary phase decouples the grains in terms of exchange coupling; the remaining coupling between the grains is magnetostatic. This coupling is enhanced if the easy axes (c-axes of the grains) align, which will form chain-like domains throughout the whole sample (can be observed in the following sections). This is very different from interaction in Sm_2Co_{17} magnets, where it is believed that exchange coupling through a ferromagnetic $SmCo_5$ phase takes place, as described in the previous chapter.

The idea of interaction domains is very similar to the exchange spring magnets [155]. Soft and hard magnetic phases are coupled in an exchange spring magnet through interfacial exchange interaction. This process hardens the underlying soft magnetic phase. This magnetic hardening can also be achieved in commercial Nd-Fe-B magnets. Pinning and Nucleation theory description can be found in section 2.3. The domain wall thickness of Nd-Fe-B is in the range of ca. 1-5 nm [156, 157].

Macroscopic sample preparation

The samples for this work were prepared at TU Darmstadt using different techniques. This chapter used two macroscopic sample preparation methods: Hot-pressing and -deformation, which will be described in the following paragraphs.

Hot-pressed Nd-Fe-B melt-spun ribbons

Hot-pressing involves compacting a powder mixture of magnetic materials under high pressure and temperature. In our case, the magnequench MQU-F powder from melt-spun ribbons¹ was used as the base powder. Melt-spinning is when the liquid material is dropped onto a fast-spinning wheel. This process will rapidly cool down the material and solidify it in a few ms.

The hot-pressing process begins by mixing the magnetic powders and then pressing the mixture into a die cavity under high pressure, typically around 200 to 400 MPa.

¹<https://mqitechnology.com/wp-content/uploads/2018/06/msds-mqu-f-20070-070-r08-ce.pdf>

The die is designed to impart the desired shape and dimensions of the magnet. A schematic sample preparation procedure can be found in figure 5.3.

Next, the compacted powder is heated to a temperature above the recrystallization temperature of the magnetic materials, typically between 800 to 1000 °C, in a controlled atmosphere to prevent oxidation. At this temperature, the particles within the compacted powder begin to bond together, forming a solid mass. As the temperature increases, the material becomes more malleable, allowing the particles to align and increasing magnetic strength.

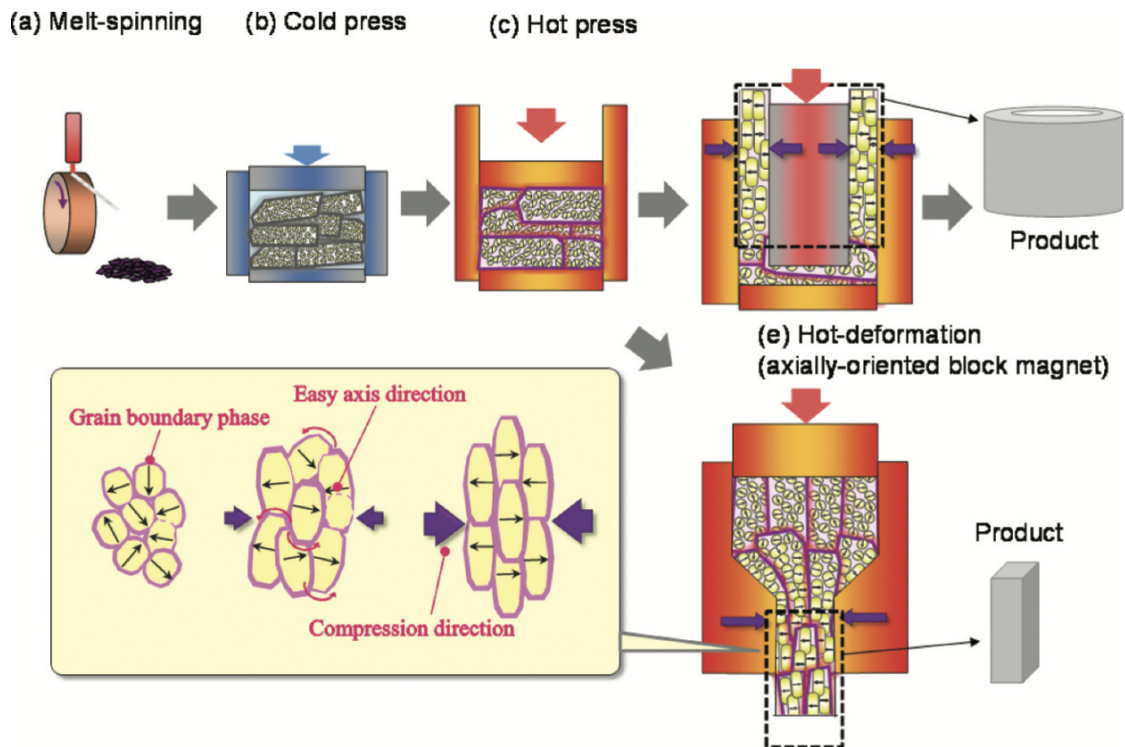


Figure 5.3.: Schematic of the production process of hot-pressing Nd-Fe-B samples. From reference [141].

Finally, the hot-pressed magnet is cooled slowly to room temperature in a controlled atmosphere to prevent oxidation and cracking. The resulting magnet has high magnetic strength, energy density, and thermal stability.

Our specific sample was first hot-pressed at 725 °C under uniaxial pressure of 150 MPa into cylinders with 13.5 mm diameter.

Hot-deformed Nd-Fe-B melt-spun ribbons

The hot-deformation process is relatively similar to the hot-pressed process and is also the first step. Subsequently, die-upsetting (allowing the increase of the diameter while applying pressure) was carried out at 750 °C with maximum uniaxial pressure of 200 MPa, using a die with a 22.5 mm diameter, resulting in a disc-shaped sample with a degree of deformation equal to one. This resulted in a highly textured bulk sample, which provides structured anisotropic flakes with c-axes orientation along the pressure applied in die-upsetting. The flakes have a size of about 100 nm by 400 nm (as one can observe in figure 5.5).

Sample processing via focussed ion beam preparation

Sample preparation using a focused ion beam (FIB) is a powerful technique used in materials science and engineering to prepare thin samples for analysis using high-resolution microscopy techniques, such as transmission electron microscopy and scanning electron microscopy. The technique uses a focused beam of ionized Ga atoms to remove material from a bulk sample selectively. A FIB was used to prepare the samples on thin SiN membranes. This is necessary because magnetic laminography requires an X-ray transparent material. This is achieved by reducing the sample thickness and a low background membrane. Therefore, the technique is reliable for preparing a μm thin sample for the hard X-ray magnetic laminography experiment. FIB systems contain a vacuum chamber containing a beam-column, sample holder, and detectors. The beam-column typically consists of a source of ionized particles, such as Ga ions, which are accelerated to high energies and focused into a tight beam using electromagnetic lenses. The detectors are used to monitor the process and image the sample. The used FIB setup, in particular, had an additional electron beam column, which can be used to receive higher-resolution images.

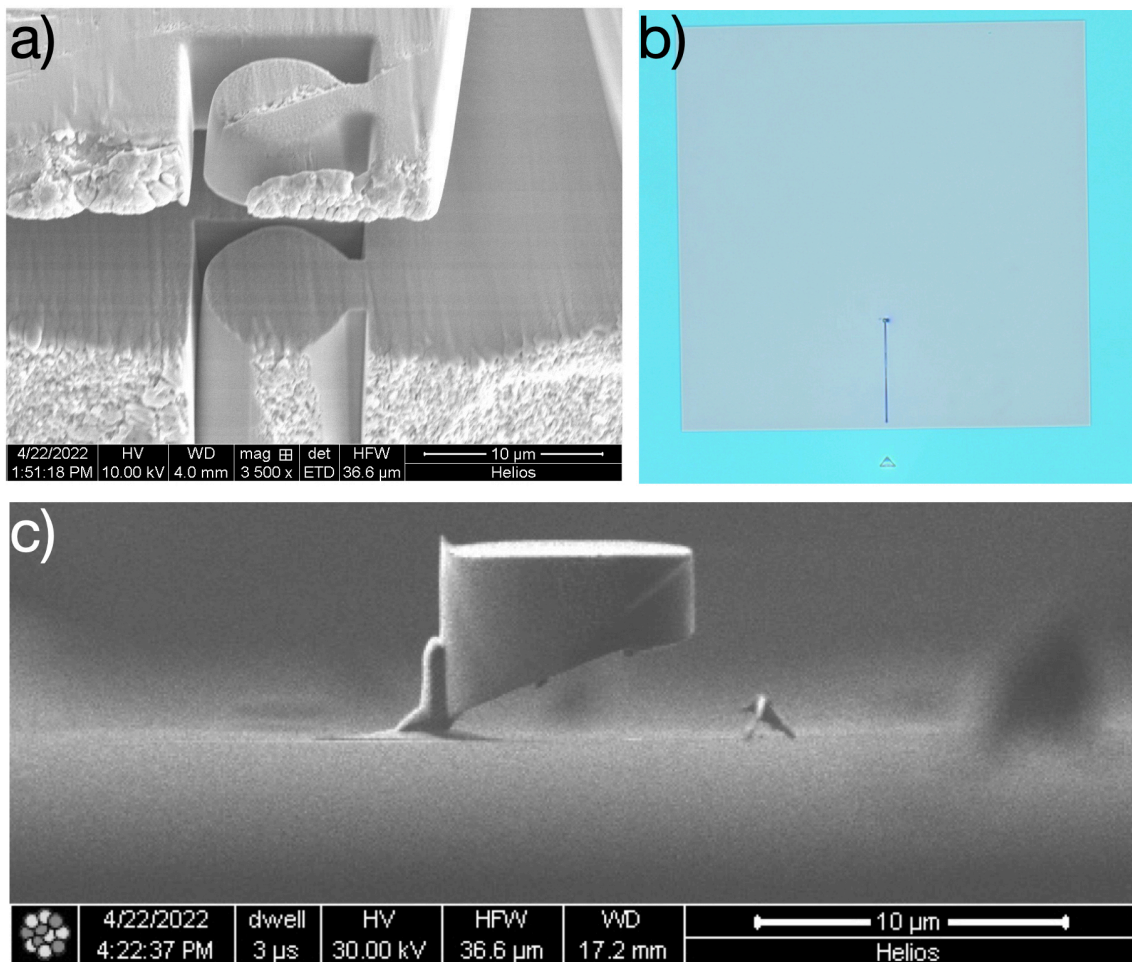


Figure 5.4.: a) electron image of the FIB cutting process for the hot-deformed sample, b) a light microscopy image of the membrane. The Pt stripe is visible on which end the sample is placed, and c) a close-up of the prepared single phase sample on the SiN membrane.

The bulk sample is first mounted onto a small substrate material during FIB sample preparation and loaded into the FIB vacuum system. The ion beam is then selectively removed material from the bulk sample. First, cutting parallel to the surface is performed with the required disk height. Then, a half disk-like form is cut out from the top, as shown in figure 5.4a). One ends up with a freestanding disk, which is then attached to the manipulator by the deposition of Pt. The Ga beam then cuts out the last piece. With the help of the manipulator, the disk is moved above the surface of the SiN membrane, where a thin Pt stripe is deposited to help with sample alignment before the cutting process. Via Pt deposition, the sample is then fixed to the SiN membrane, and finally, the Gd beam cuts off the manipulator needle. Once the membrane is prepared, it can be removed under the ambient atmosphere. The whole process described here is depicted in more detail schematically in figure B.1 in the appendix B. A light microscopy image of the prepared sample before the experiment can be found in figure 5.4b). Pt fixes the sample onto the SiN membrane. The free-standing disc-like sample on the membrane can be seen in figure 5.4c). All samples are around 9 μm by 6 μm and shaped like a disc.

Atomic structure by electron backscatter diffraction

Electron backscattering diffraction (EBSD) is a powerful microscopy technique used to study the crystallographic properties of materials at a microscopic level. In this work, the technique is used to get the microstructure of the highly structured sample. In EBSD, a beam of high-energy electrons is directed onto a sample, and the backscattered electrons are collected using a 2D detector. Information about the crystal structure, crystal orientation, and grain boundaries can be obtained by analyzing the patterns formed by the backscattered electrons. Scanning the whole sample allows the scattering pattern to be collected for multiple spots on the surface. This can be further increased by comparing the reflexes from the sample to a known lattice, in our case, the lattice structure of $\text{Nd}_2\text{Fe}_{14}\text{B}$.

The main advantage of EBSD is its ability to provide high-resolution crystallographic information on a microscopic scale. It can be used to study the microstructure of materials in great detail, including the crystallographic orientation of individual grains, grain boundaries, and defects such as dislocations and twins. EBSD can also be used to determine the texture of polycrystalline materials, which is essential for understanding their mechanical and physical properties [158].

EBSD maps were acquired at a voltage of 20 kV using a step size of 15 nm. Neighbor Pattern Averaging and Reindexing (NPARTM) was used for post-processing to improve the signal-to-noise ratio. Enrico Bruder conducted the measurements at the TU Darmstadt. The EBSD analysis for the anisotropic prepared (hot-pressed) sample can be found in figure 5.5. The color in the EBSD map on the left represents how the axes are aligned toward the vertical map direction. The axes A1 and A2 are the sample coordinates, where A1 is parallel to the vertical axis of the EBSD map, and A2 is horizontal. The circle in the lower right shows that most grains are aligned parallel to the 001 direction (or c-axis) with the vertical direction. The color scale above the polar map shows that the c-axis is about 14.5 times more likely to be aligned in the A2 direction than in random distribution. On the left side of the EBSD map, one can see larger grains, most probably from the so-called flake boundary, which comes from the cooling gradient during the melt spinning. These

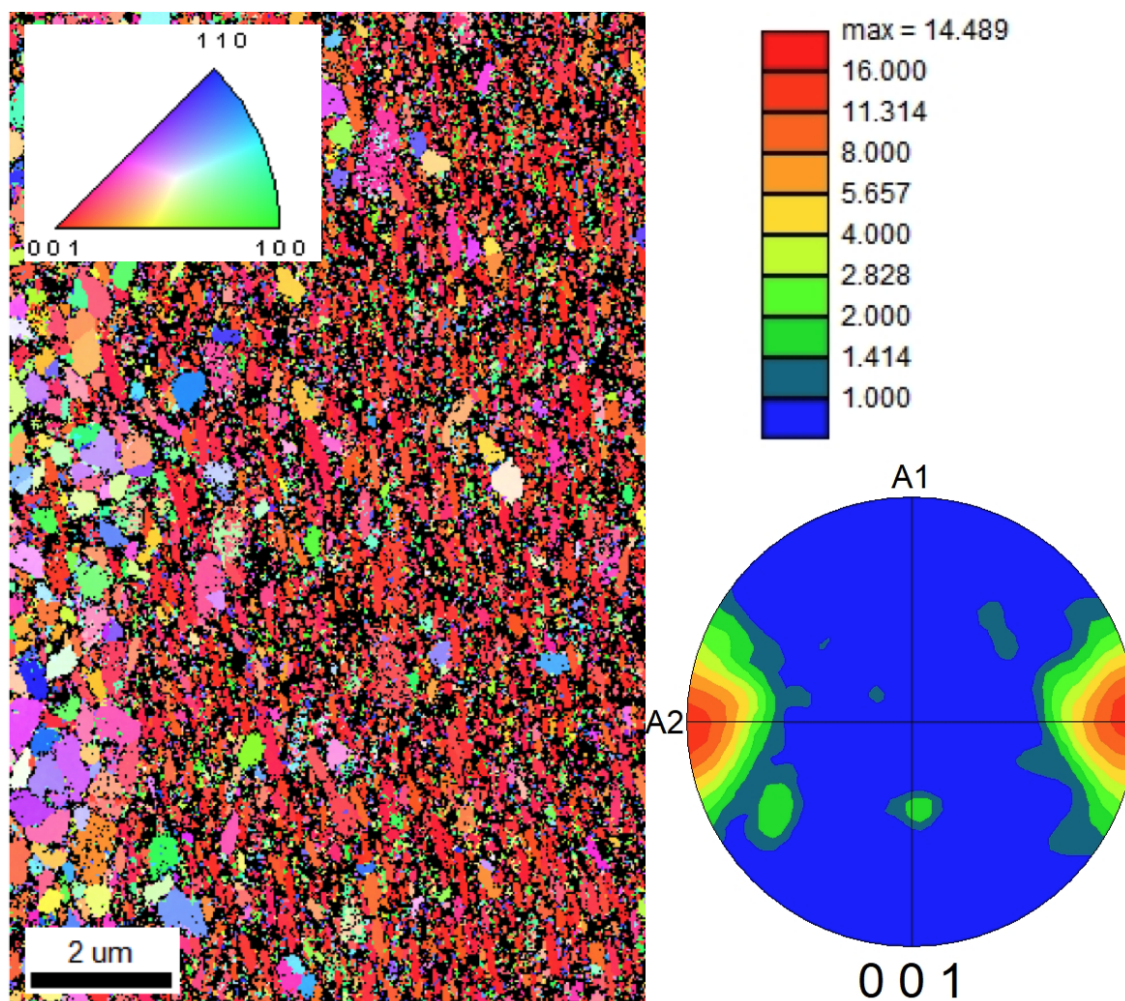


Figure 5.5.: EBSD analysis of the anisotropic prepared hot-deformed $\text{Nd}_2\text{Fe}_{14}\text{B}$ sample shows a high texture of the underlying grains. From E. Bruder at TU Darmstadt.

measurements show high textured grains and microstructure within the sample of anisotropic prepared hot-deformed $\text{Nd}_2\text{Fe}_{14}\text{B}$.

Figure 5.6 shows a scanning electron microscopy image of the sample. In the image, one can see that the grain size is roughly $100\text{ nm} \times 400\text{ nm}$. The distribution of the particles looks pretty oriented with the long axis along the vertical picture axis.

Macroscopic magnetic characterization by magnetometry

This paragraph will examine the macroscopic magnetization measurements for the later investigated samples. The macroscopic magnetic measurements in this chapter were performed using a vibrating sample magnetometer (VSM) in the physical property measurement system (PPMS-14, Quantum Design).

The performed measurements can be found in figure 5.7. All samples are very close to saturation at 5 T and have similar values for the saturation magnetization ranging from ca. 120 to $145\text{ Am}^2/\text{kg}$. The isotropic single phase $\text{Nd}_2\text{Fe}_{14}\text{B}$ sample shows in the first magnetization curve a pinning-type behavior with increasing fields (see section 2.3). The hot-pressed, Nd-rich, and hot-deformed sample shows an

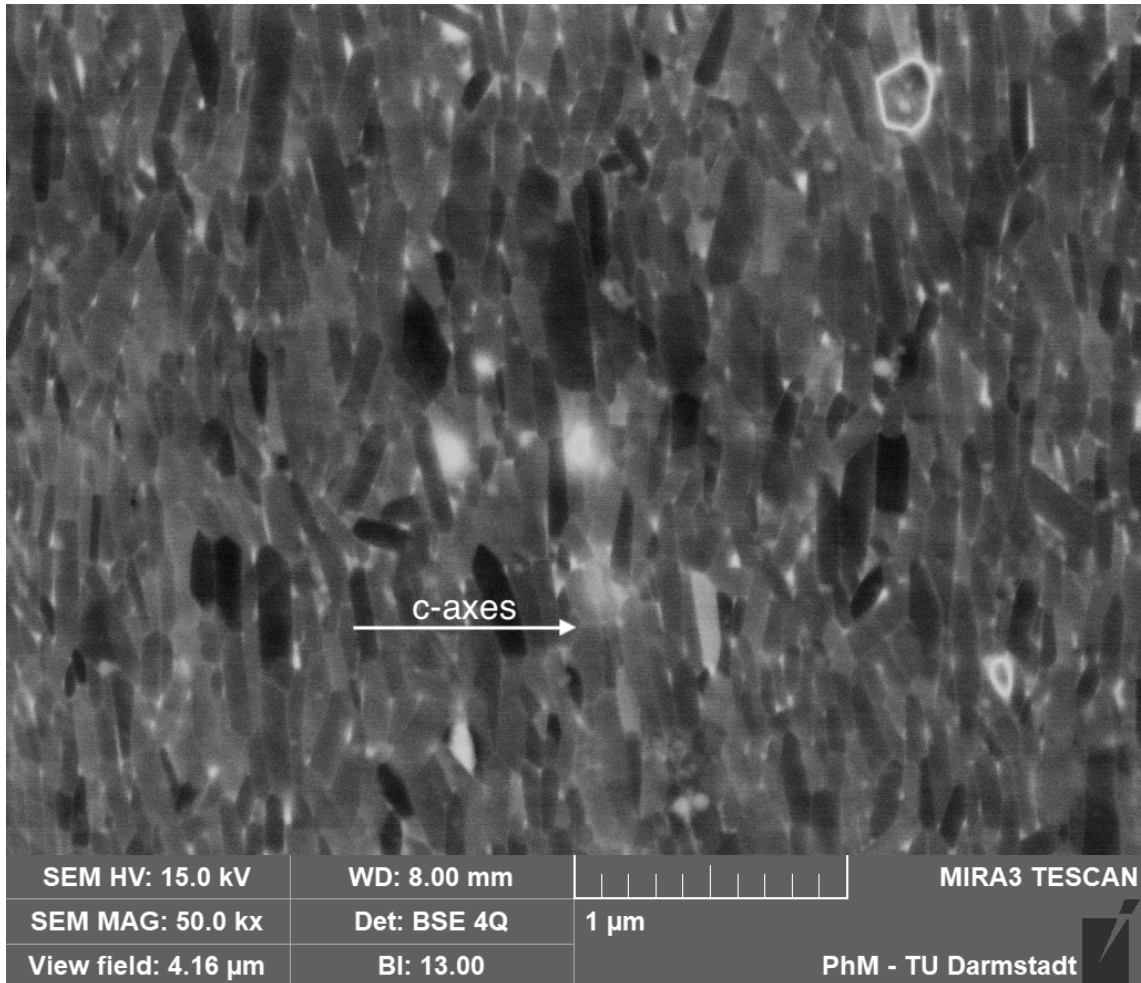


Figure 5.6.: Scanning electron image of an hot-deformed sample. From E. Bruder at TU Darmstadt.

exponential increase in the first magnetization curve, indicating a nucleation-type magnetic behavior. It is important to note that the first magnetization process follows a two-step behavior, which indicates several processes taking place in the sample and will be discussed later.

The coercive field is the highest for the Nd-rich sample (ca. 2.1 T), followed by the hot-pressed sample (1.9 T). The hot-deformed sample has a coercive field of ca. 1.4 T. The smallest coercive field has a single-phase sample of ca. 1 T. The lower coercivity for the higher texture can be explained by collective switching behavior, which expands chain-like through the whole sample during the magnetization reversal process. This can be observed in the gradually textured hot-deformed magnetic samples [138]. The coercivity, in general, in highly structured samples is lower than in non or less-structured samples. During the magnetic reversal process, the domains can flip in a chain-like behavior, therefore being more linked.

The hot-deformed sample achieves the highest remanence of about 1.30 T, followed by the single-phase sample with about 0.83 T. The Nd-rich and hot-pressed samples are lower in remanence and have roughly the same value. For the Nd-rich sample, it is 0.70 T; for the hot-pressed sample, it is 0.68 T. In the high textured hot-deformed sample, the remanence is much higher, which would align with the fact that there

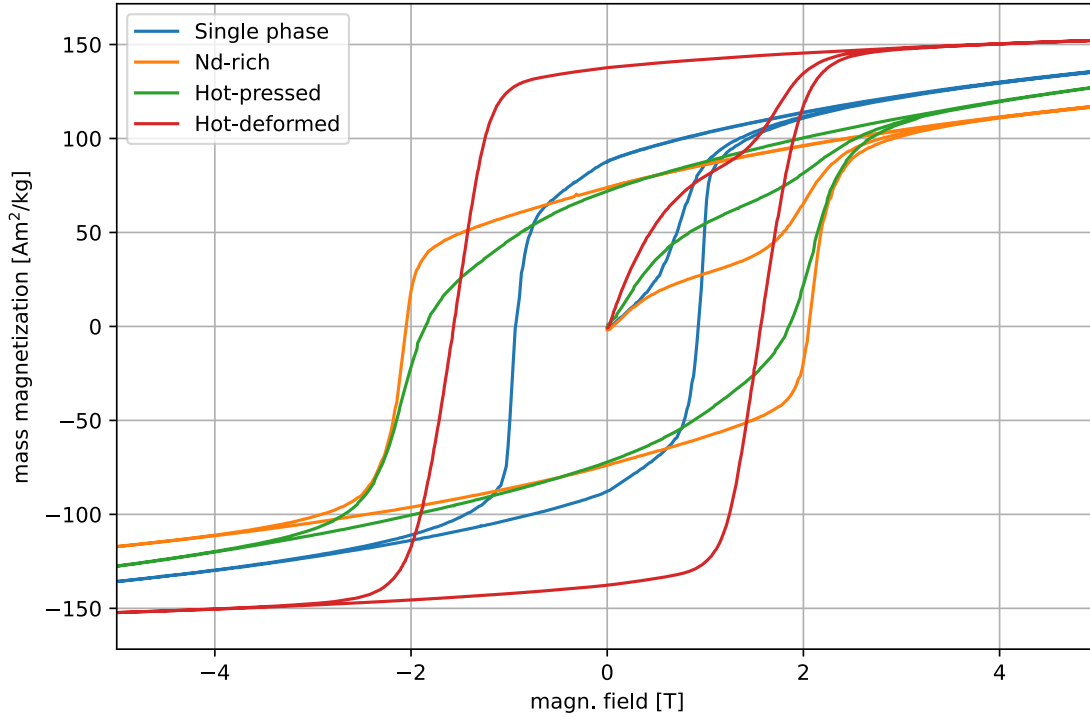


Figure 5.7.: Magnetic hysteresis curves for the different samples. From A. Aubert at TU Darmstadt.

are more grains oriented in the direction of the applied magnetic field and, therefore, more c-axis.

We see that the form of the hot-deformed sample's hysteresis loop is much more rectangular. This underlined the strong pinning of the domains during the magnetic reversal process. Only a small percentage of the sample loses the magnetic moment during the applied field reversal process. After the threshold of about 2.0 T applied field, the chain-like reaction starts, and the magnetic reversal process resembles a fast switching of the magnetization direction.

The maximum energy product $(BH)_{\max}$ of the samples are shown in figure 5.8a) as described with equation (2.1). The textured hot-deformed sample has the highest $(BH)_{\max}$, followed by the Nd-rich. The hot-pressed and single-phase sample has around the same $(BH)_{\max}$. It is interesting to note that the hot-deformed sample has an around three times higher maximum energy product $(BH)_{\max}$. With a density of 7590 kg/m^{-3} for $\text{Nd}_2\text{Fe}_{14}\text{B}$, this would mean for the lower maximum energy product $(BH)_{\max}$ of ca. 300 kJ/m^3 to 987 kJ/m^3 . The error bars are estimated to be around 20 %.

In figure 5.8b), the hysteresis curve for the highest textured sample is shown together with the inset of the schematics from figure 5.2. From the first magnetization curve, one can calculate the so-called single domain grain ratio (SDGR), which is described as an estimate of how many single- vs. multi-domain grains are in the sample [141]:

$$\text{SDGR} = 1 - \frac{J_1}{J_S}, \quad (5.1)$$

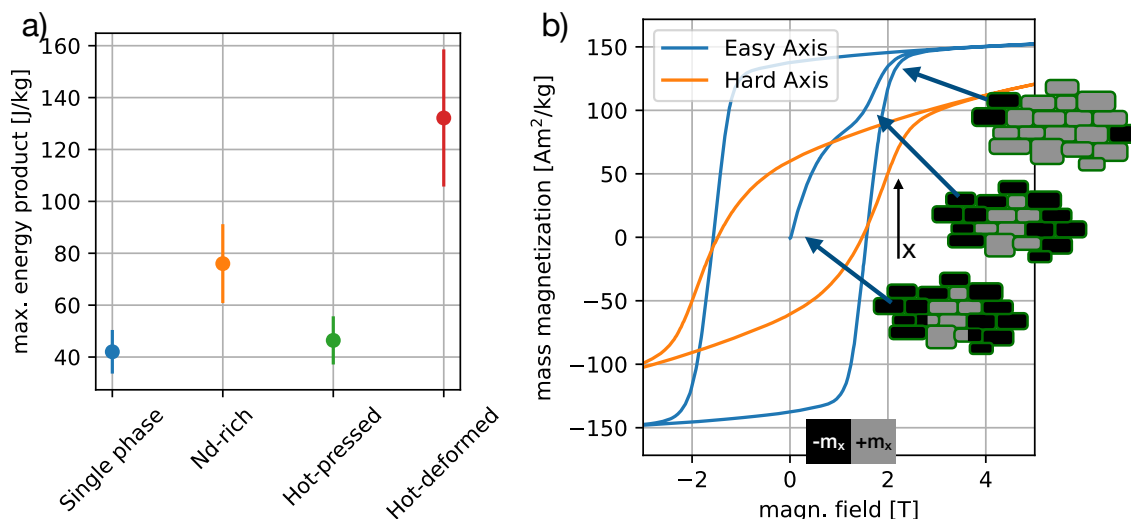


Figure 5.8.: a) maximum energy product $(BH)_{\max}$ of the previous data from figure 5.7. b) magnetic hysteresis data for the hot-deformed sample and the schematic for grain switching from figure 5.2.

where J_1 is the inflection point, and J_S is the magnetization at the saturation. With equation (5.1), an estimation for the ratio of single-domain grains within the sample can be obtained. For the shown hot-deformed sample, with $J_1 = 80 \text{ Am}^2/\text{kg}$ and a saturation magnetization of $J_S = 150 \text{ Am}^2/\text{kg}$ an overall SDGR of ca. 47 % can be estimated. One can estimate an SDGR for the Nd-rich sample of ca. 30 % and the hot-pressed sample of ca. 55 %. For the single-phase sample, there is no indication of a two-step behavior within the first magnetization curve.

5.2. Experimental evaluation and data processing

This section will first have a look at the measurement setup used to obtain the data for the previously discussed samples and sample systems. It will also look at how the data was treated to derive a 3D model of the magnetization at the end of this section. Laminography was first mentioned by Hasenkamp in 1973 [159]. Laminography also does not allow the reconstruction of a 3D structure with isotropic resolution, but the missing information is reduced from a wedge to a cone in reciprocal space [160,161]. It has been shown that this information can be recovered.

Experimental setup and alignment at the cSAXS beamline

The measurements were carried out at the cSAXS beamline of the Swiss Light Source (SLS) at the Paul Scherrer Institute in Villigen, CH. The beamline is designed to do small-angle X-ray scattering experiments; therefore, it is equipped with a ca. 7 m long flight tube with a high-resolution 2D Eiger detector exhibiting 1.5 million pixels. Ptychography measurements, in general, work in transmission and reflection. The measurements presented in this work were performed in transmission mode. The LamNI endstation setup for the experiment was used, which will be described shortly. Figure 5.9a) shows a basic schematic of the setup. A CAD model of the LamNI instrument can be seen in b) without the detectors and most X-ray optics.

The Fresnel zone plate is directly attached to the front of the X-ray optics holder. The largest peculiarity of this setup is the tilted sample rotation axis, which is tilted in the following way: parallel to the X-ray propagation direction (z-axis), the stage is first tilted around the x-axis by 15° and then tilted around the y-axis by 60° . This results in a 61° (laminography angle) between the incoming X-ray and the rotation axis. The sample position is measured with laser interferometers, which are indicated in figure 5.9 b). A complex double rotational sample stage keeps the interferometers in the same coordinate system. Holler and coworkers can find more details on the setup in reference [67].

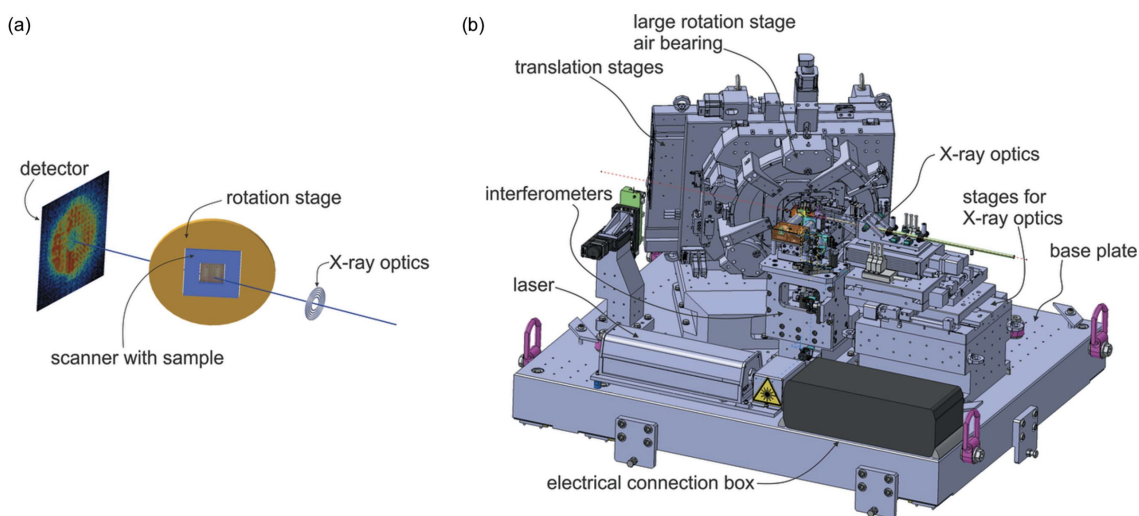


Figure 5.9.: a) schematic of measurement setup b) LamNI instrument as a CAD model without detector setup. From reference [67].

The measurement setup involved aligning the samples using a light microscope attached to a camera. However, the tilting angle limited the view of the membrane and the attached sample. A Pt stripe was attached to the sample to overcome this, as previously described in the FIB preparation process. It helped in locating it using the camera monitor. The scan type used is shown in figure 5.10. As the sample and sample membrane window were tilted, the field of view appeared as an ellipse. The two color markers in the figure represent the two circular polarization measurements taken at the same rotation angle. The diffraction images obtained on the sample were slightly different. However, since the reconstructed 2D image can be aligned, the two varied measurements can still be overlapped coherently.

The SLS cSAXS beamline produces light using a linear undulator, which requires transforming the polarization from linear to left and right circular polarized light. To achieve this, a phase retarder is inserted between the beamline optics and the sample. Circular polarization is achieved during the experiment by adjusting the angles, number, and position of the inserted quarter wave plates, as described in reference [162]. The circular polarization of the X-rays was determined to exceed 99%, while the phase plate absorbed approximately 65% of the incident light in the setup [72].

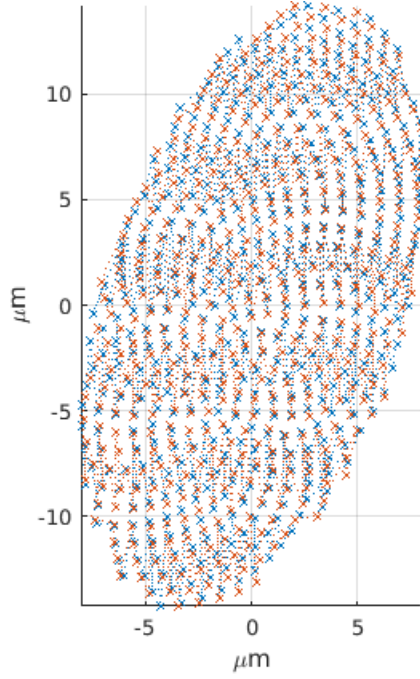


Figure 5.10: Scanning steps of roughly 200 spots, with the measured two different polarizations in blue and red forming an elliptic field of view.

Without an applied field, the XMCD effect is probed in the hard X-ray region at the L_2 -edge of the Nd-Fe-B samples. The complex transmission function is given by:

$$T(E) = A(E) \exp\{i\phi(E)\}, \quad (5.2)$$

where A is the amplitude and ϕ is the phase. Both are dependent on the X-ray energy. We can now define two XMCD signals, the amplitude XMCD A_{XMCD} and the phase XMCD ϕ_{XMCD} :

$$A_{\text{XMCD}} = \frac{|A_L|^2 - |A_R|^2}{\Delta_{\text{edge}}} \quad (5.3)$$

$$\phi_{\text{XMCD}} = \phi_L - \phi_R, \quad (5.4)$$

Where Δ_{edge} is the relative change in absorption across the absorption edge. An X-ray absorption spectrum of the sample can be obtained by moving the linear undulator's energy and recording the integral over all roughly 1.5 million pixels of the Eiger detector. The representative XAS measurement for the samples in transmission can be found in figure 5.11a) for the Nd L_2 -edge for the hot-deformed sample. As expected, both samples have the same XAS fingerprint. The measured spectrum is in good agreement with the literature, for example, measured spectra by Gomez et al. [private communication] (see figure 5.11b)) or Menushenkov et al. (see reference [154]). Tuning the energy to 6728 eV will provide the largest XMCD contrast.

Figure 5.12 shows the XMCD projection for 3 different energies. The magnetic contrast is visible in every single projection. The color bar shows the magnetic contrast in arbitrary units. The best magnetic signal was obtained for 6728 eV, which was used for the measurements.

The non-magnetic projection for the isotropic hot-deformed sample is shown in figure 5.13a) for 36° . In subfigure b), the XMCD projection is shown for angle 36° and

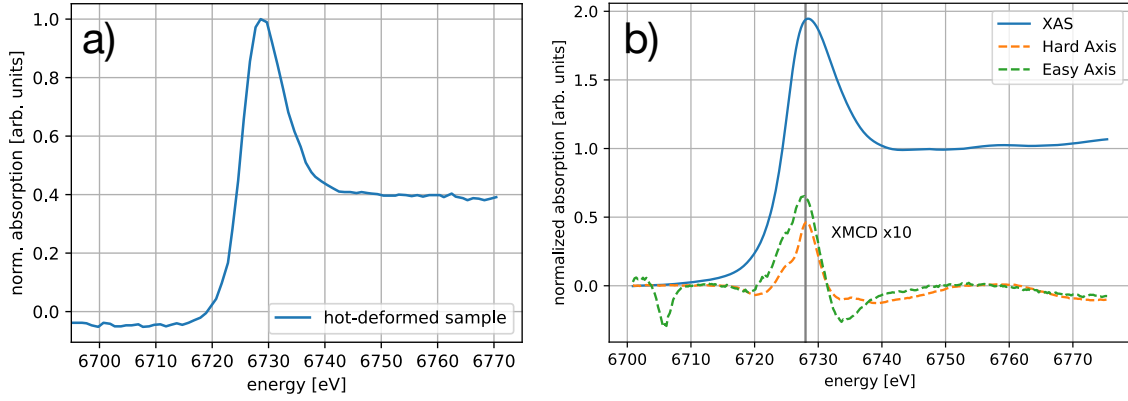


Figure 5.11.: a) XAS by integrating over all the pixels of the detector for the Nd L_2 -edge for the hot-deformed sample b) XAS and XMCD of a similar Nd-Fe-B sample to compare the energy features. b) data collected by G. Gomez at ESRF.

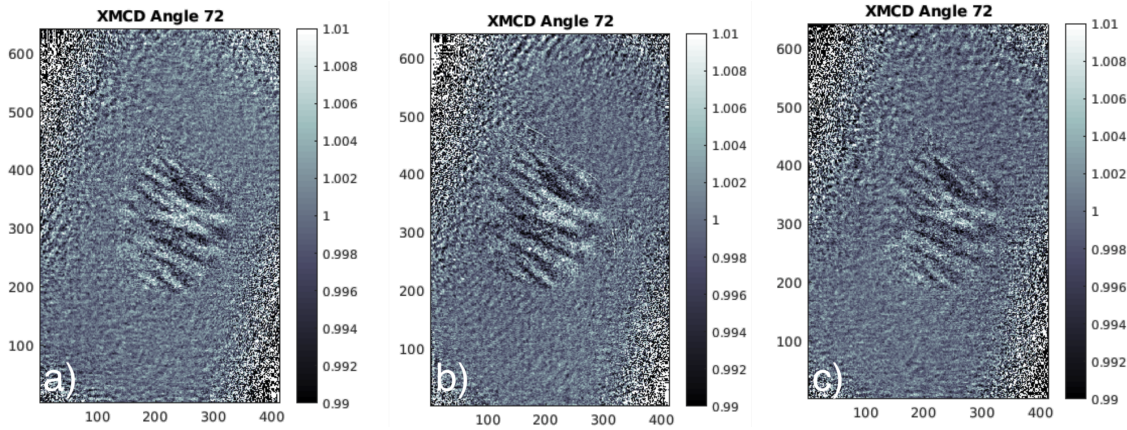


Figure 5.12.: XMCD projections measured with energies of a) 6727 eV , b) 6728 eV , and c) 6729 eV at 72° rotation angle.

c) 108° rotation angle. One can see that the magnetic domains in this sample are too small to identify them within the noise level from the membrane surrounding the sample. The Nd-rich and single-phase samples were measured in the same way but did not show any magnetic contrast. This concludes that in these samples, the interaction domains are so small that the spatial resolution of the measurement is so low that the actual magnetic signal is below the noise level.

Reconstruction model

The process of 2D image recovery necessitates a 4D dataset [163]. However, this poses a challenge when utilizing 2D detectors for measurement purposes. During the diffraction measurement, the phase information is lost, which needs to be recovered. The difference map method is used for the first few hundred iterations (more information in reference [164]). The maximum likelihood method was applied additionally (more information can be found in reference [165]). For the reconstruction pipeline, the software package *PtychoShelves* was used (see reference [166]).

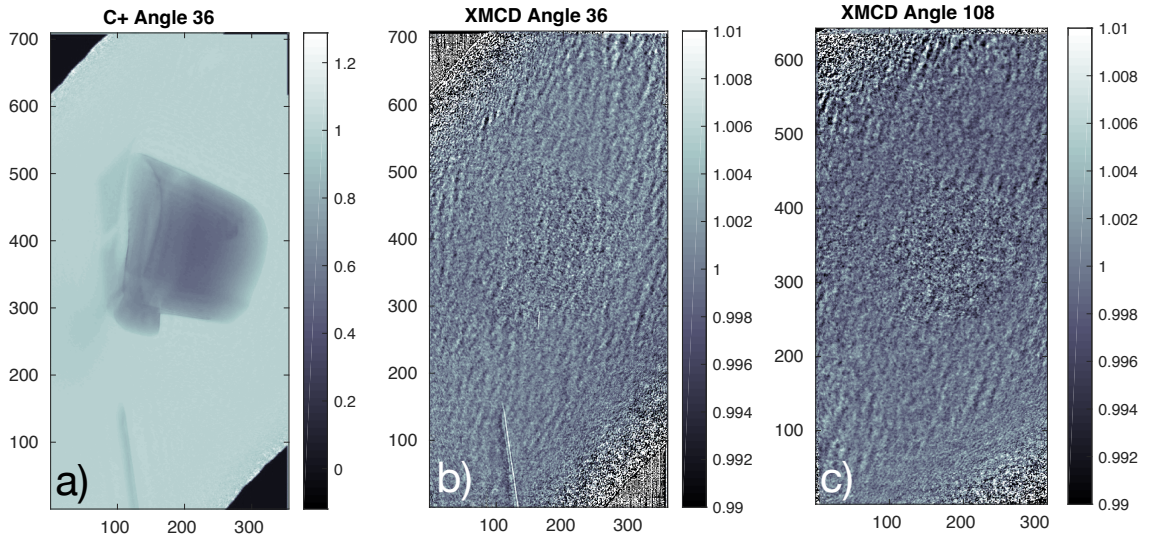


Figure 5.13.: Isotropic hot-pressed sample: reconstructions a) of positive helicity of light at 36° , b) XMCD contrast at 36° , and c) and XMCD contrast at 108° rotation angle.

With the multiple 2D images measured at different laminography angles, methods described in the theory section 3.4 can be applied to the data set.

In figure 5.14, a comparison between the measured magnetic projection (top row) and projections reconstructed (bottom row) from the 3D magnetic structure is shown for the three different laminography angles 40° , 80° , and 275° . One can see that almost all of the features can be found in both images measured or reconstructed at the same angle. This shows that the 3D magnetic structure exhibits high certainty. The complete reconstructed 3D magnetic structure will be analyzed in more detail in the next section 5.3.

Before integrating the 2D projections into a 3D image using the reconstruction algorithm, the signal-to-noise ratio is enhanced. The filtering procedures and their effect on the 2D projections to improve the XMCD projection signal and minimize artifacts are shown in figure 5.15. A Gaussian filter with a standard deviation of $\sigma = 8$ pixels is used to smooth the image. An image later Gaussian filtering with a σ of 50 pixels is generated. As seen in the top right image, the resulting image is subtracted to minimize the artifacts, such as bright, overexposed, or dark shadow areas. Due to the low frequency of the artifacts, the magnetic signal is not interrupted.

By doing so, the signal originating from areas outside the sample, which is regarded as noise, is significantly diminished. As a result, the magnetic contrast of the sample is accentuated and becomes more noticeable.

5.3. 3D magnetic structure of the hot-deformed sample

The 3D magnetic structure of the highly textured anisotropic prepared sample (hot-deformed sample) could be successfully derived. This section will analyze the structure regarding the domains, the direction of magnetizations, and the implications

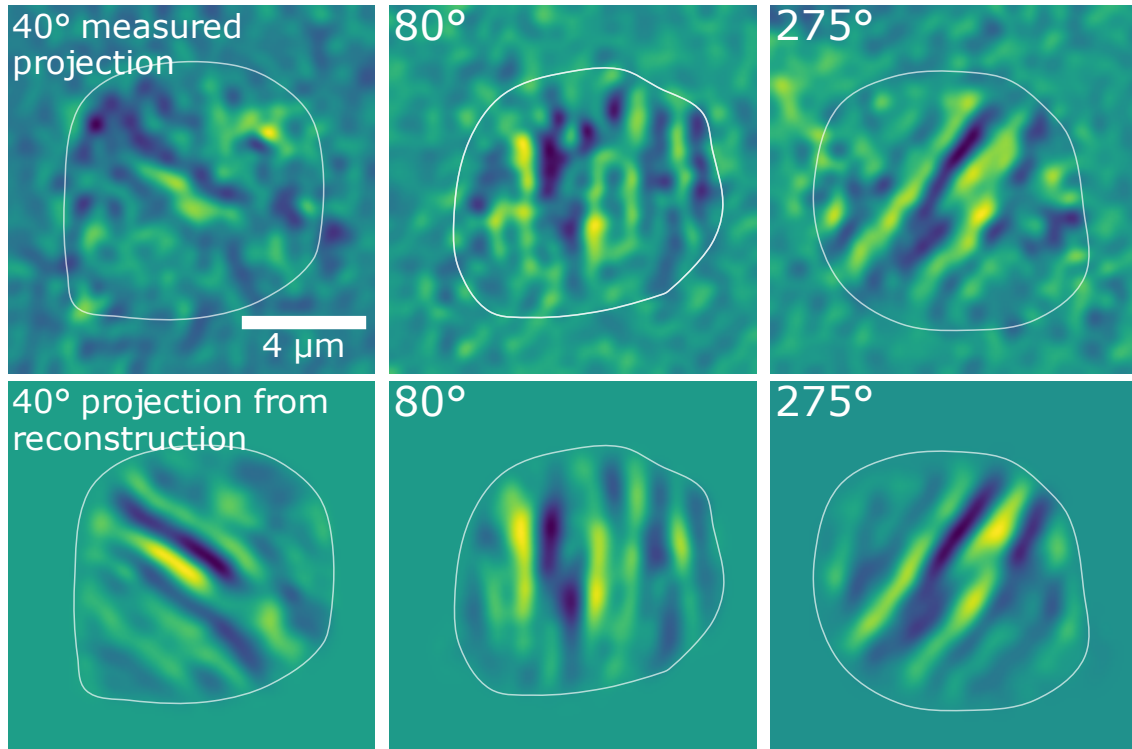


Figure 5.14.: Comparison between the measured magnetic projection (top row) and the projection model from the 3D magnetic reconstruction (bottom row). Region of the sample is marked.

of the measurement error and spatial resolutions. Figure 5.16 shows a side-by-side comparison of the magnetic domain structure inside and at the sample's surface. The magnetization along the x-axis can be seen. Here, the positive domains are shown in red, and the negative domains are in blue. The magnetization is normalized to one. The magnetic x-component is about an order of magnitude higher than the y- and z-component of the magnetization. The white arrows depict the c-axes orientation. In subfigure a), the sample is shown magnetization on the surface of the sample. Subfigure b) shows the sample with one cutout in each direction to emphasize how the domains evolve inside the bulk material. From the top, the domains look stripe-like, and from the side, perpendicular to the c-axis, a complex maze-like pattern occurs. It can be observed that at the surface as well as in bulk, the domains form the well-known maze-like structures, which were observed by Thielsch et al. on the surface [140], which can be seen in figure 5.17. Here, an island-like domain is indicated by a circle. The rectangle indicates a more maze-like domain. The following paragraphs will explain how these different structures relate to each other.

In figure 5.18, the transition from an island-like domain (indicated by the circle) to a more maze-like structure (indicated by the rectangle) can be observed. These structures are evident in the surface magnetic image, as shown in figure 5.17. This transition provides valuable insights into the underlying magnetic structure. Different representations of the domain structures are shown to explore how the magnetic domains follow along within the sample in figure 5.19. In subfigure a), an extract of the complete structure is shown. If the sample is cut in the upper half perpendicular to the c-axis, one would observe an island-like impression, which vanishes if one cuts

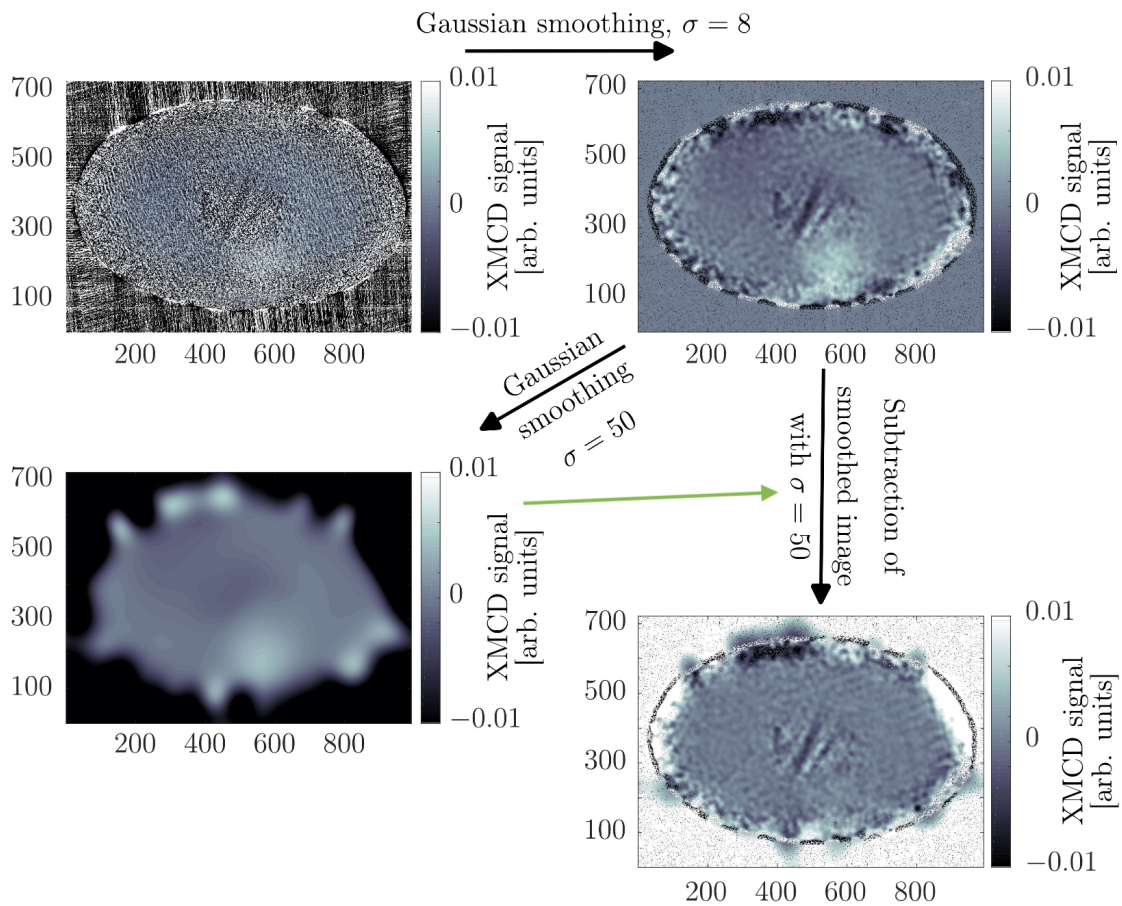


Figure 5.15.: Filtering procedures and their effect for the 2D projections to improve the XMCD projection signal and minimize artifacts. A Gaussian filter with a standard deviation of $\sigma = 8$ pixels is used to smooth the image. An image later Gaussian filtering with a sigma of 50 pixels is generated, and the resulting image is subtracted to minimize artifacts such as bright, overexposed areas or dark shadow areas. Adapted from reference [167].

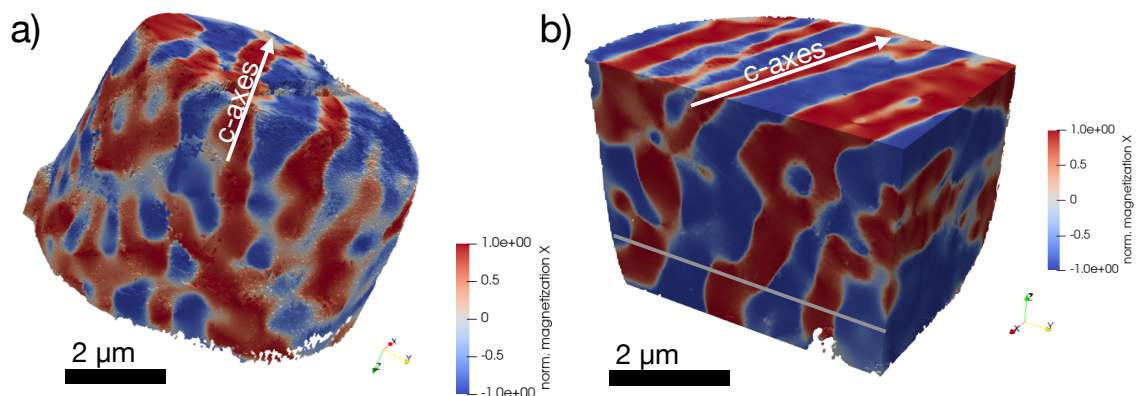


Figure 5.16.: Magnetization a) on the sample's surface and b) in the center of the sample. The grey line shows an example line profile. The c-axes direction of grains depicted by white arrows.

Figure 5.17: MFM image of the thermally demagnetized state with the c-axis perpendicular to the imaging plane and magnification as in image. One domain appearing like an island is highlighted by a circle. Adapted from reference [140].

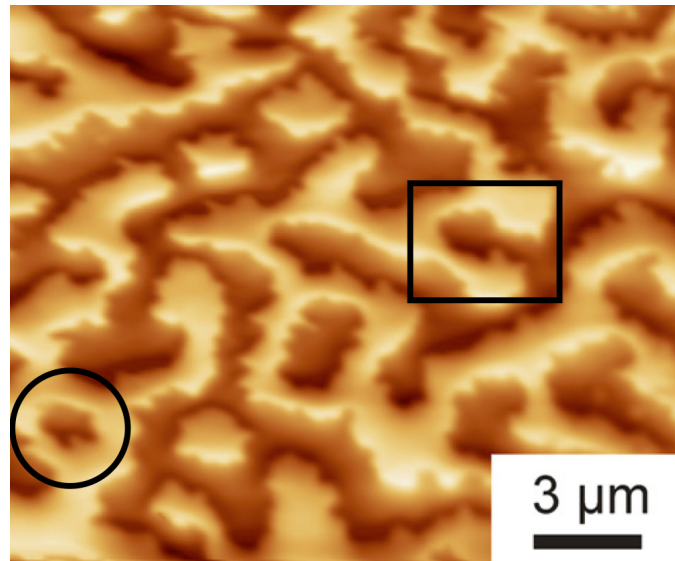
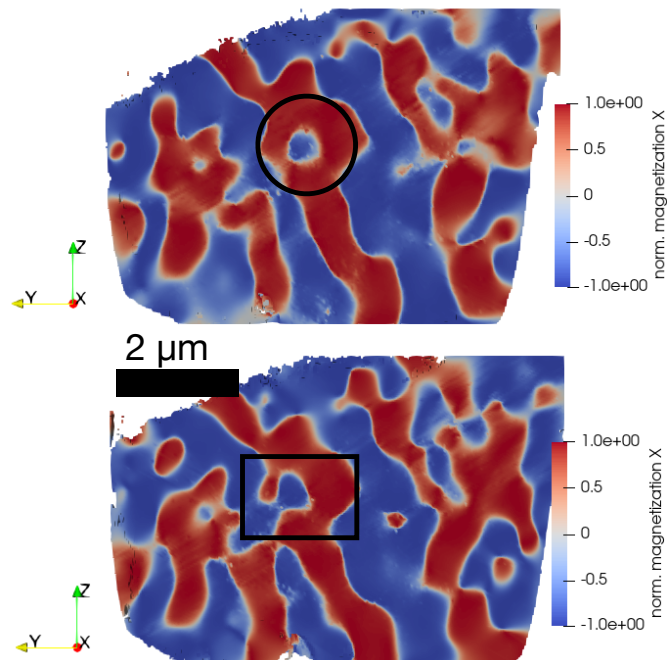


Figure 5.18: Magnetization within the sample showing the transition from the appearing island domain to a more maze-like domain during the step size of ca. $1 \mu\text{m}$.



through the sample. The sketch and the violet domain in subfigure b) emphasize this behavior. In subfigure c), the domain structure is again shown in red for the positive domains and blue for the negative. From these representations, one can also see that all domains are connected.

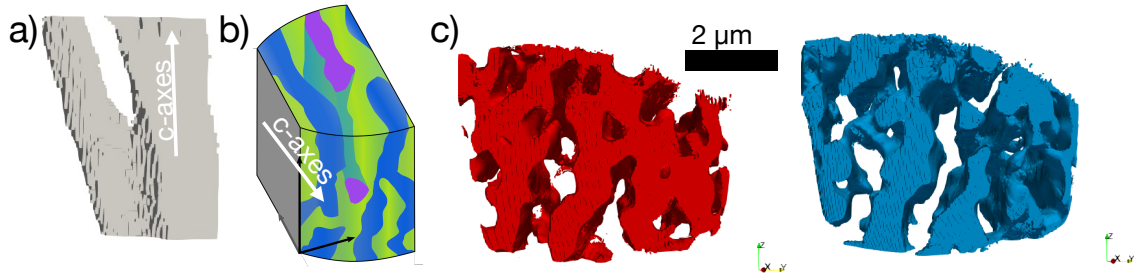


Figure 5.19.: a) Extraction of a 3D domain b) schematic on complex domain structure. C-axes direction of grains depicted in white arrows. c) positive and negative domains colored in red and blue.

To compare slice by slice how the magnetic domains are developing, in figure 5.20, the reference values and coordination system of the sample are shown along all three spatial axes. The coordination system is used as in figure 5.18. These slice-by-slice comparisons are shown in green and blue and are only 2D. The chosen center point for the sample coordination system for x is 465 px, 470 px for y , and for the height z is 130 px. The coordination system of the sample is defined as x being along stripe direction (visible in c)), z being along the most significant symmetry axis of the sample, and therefore y being perpendicular to both. The colors in the figure represent the magnetization along the x -direction in arbitrary units, where red represents positive magnetization and blue negative magnetization.

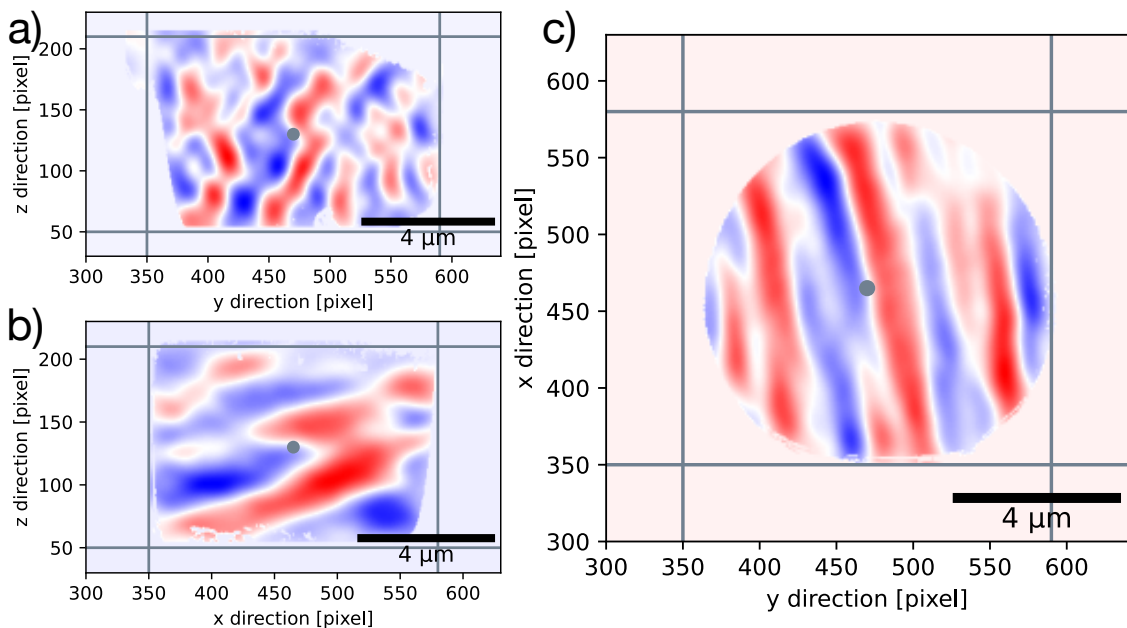


Figure 5.20.: View of the sample along the a) x -direction, b) y -direction, and c) z -direction. Magnetic contrast along the x -direction used for the visualization of all figures.

A more detailed view of the magnetic structure is shown through the figures 5.21 to 5.23. Here, only the magnetization along the x-direction is plotted since it is, by a factor of about ten, the most dominant component of the 3D magnetization due to the grain orientation. The blue and red colors show the magnitude and sign. For better visualization of the domain walls, the sharpness is increased where the magnetization in the x-direction changes the sign. Again, one can verify the maze-like pattern observed in other studies.

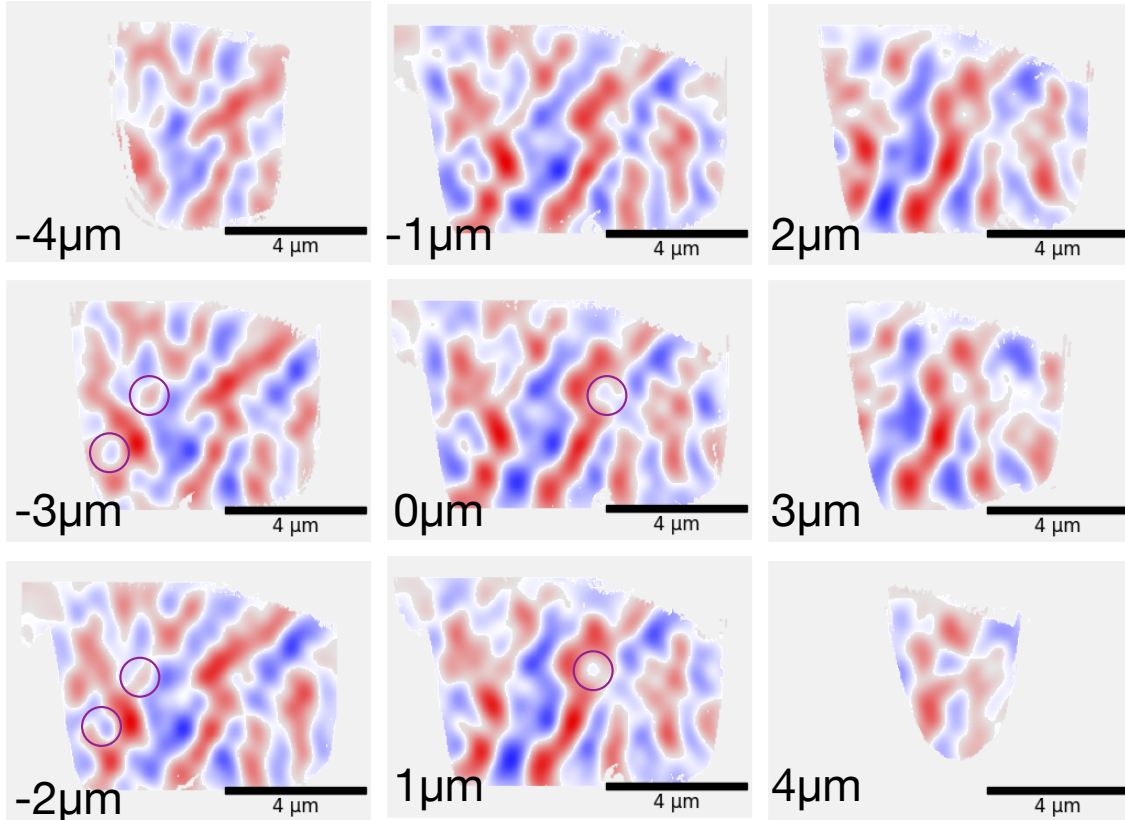


Figure 5.21.: Slices through the sample along the sample x-direction.

Figure 5.21 shows slices through the y-z plane, so looking along the x-direction of the coordinates of the sample. Starting at $-4 \mu\text{m}$, the point of view moves along the x-direction, each slice separated by $1 \mu\text{m}$. The scale bar shown in the lower right corner of each subfigure is $4 \mu\text{m}$.

Particular attractive regions to follow through the sample slice are marked in the image. In the same region, the domain is closed a few μm later at the shown slice at $3 \mu\text{m}$.

By analyzing the domain regions in the x-direction of the sample, it can be inferred that the presence of island or branching domains is not solely attributed to the surface proximity in surface-sensitive measurement techniques, as they are also observed within the sample. Furthermore, our findings suggest that certain branching domains at the surface do not simply reverse polarity upon penetrating deeper into the sample material but instead undergo a transformation in shape and merge into more complex and labyrinthine magnetic domain branches within the sample for all of the structures.

The sample from the y-direction (see figure 5.22) will be looked closer at. This view is perpendicular to the stripes and the symmetry axis of the sample cylinder. The

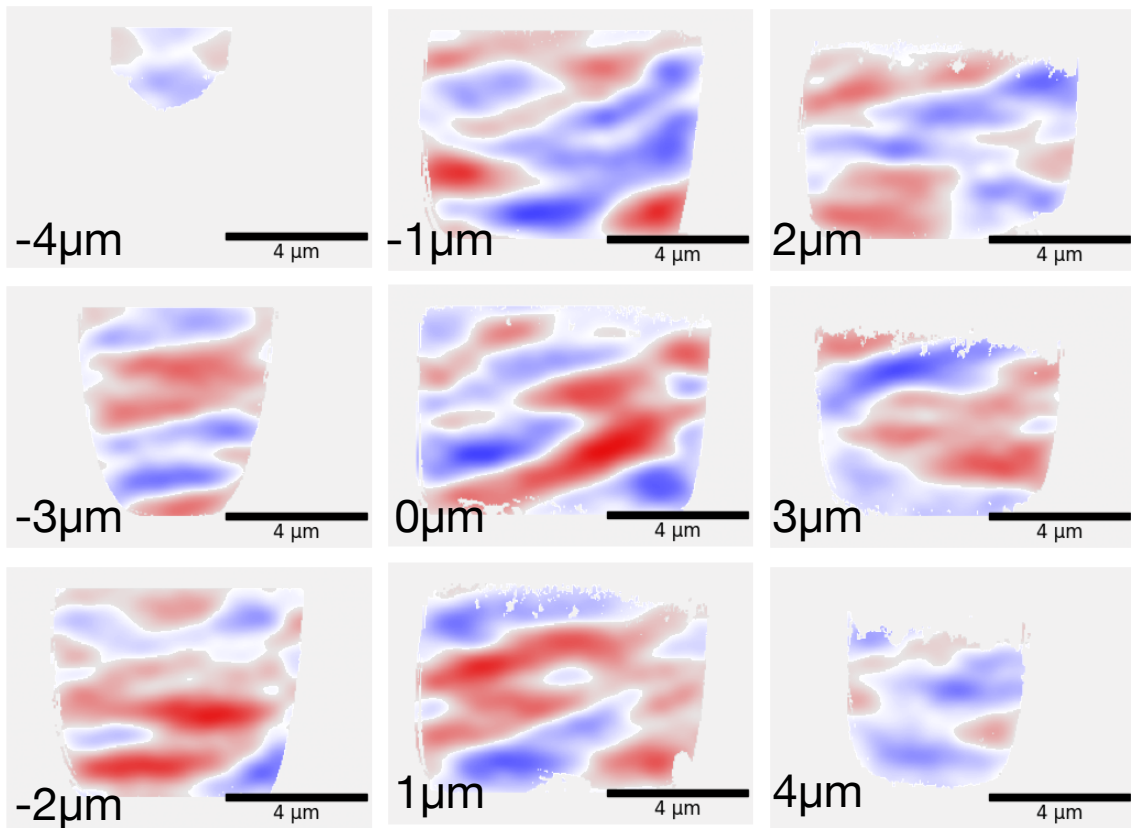


Figure 5.22.: Slices through the sample along the sample y-direction.

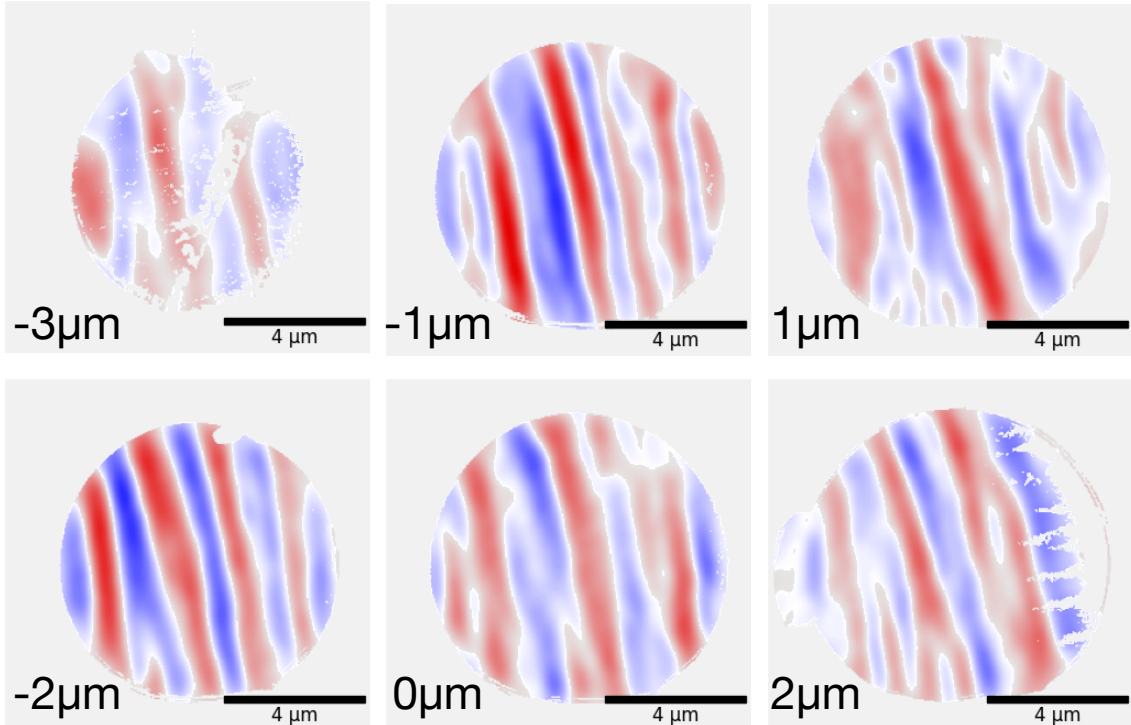


Figure 5.23.: Slices through the sample along the sample z-direction.

slicing steps are the same as in the visualization before, just along a different axis (y-axis). Looking at the x-component of the magnetization from this direction reveals

another picture. The domains in the slices seem more chaotic; the domains are relatively large from this angle and mostly connected through complex patterns. In the centered subfigure at 0 μm , one can see that the large red domains stretch from the top of the sample to the bottom. The slice at 3 μm shows similar behavior. The large blue domain stretches the whole sample height in a C-shape manner. Although it appears that the view from this angle of single islands exists, these domains are also connected to domains of the same kind.

Looking at the slices perpendicular to the symmetric axis of the disc (view along the z-axis), one can observe a stripe-like pattern in the sample. One can observe that the magnetization follows along the easy axis of the sample, which is the x-direction of the sample. This axis is the preferred orientation of the grains' c-axes. The small divergence of approximately 15° from the domain direction and the x-axis is factored in by multiplying the outcome by $\cos 15^\circ$. This is negligible at the spatial resolution. Around the center slice, the stripes are not separated. More complex domain patterns, like branching patterns, could be found on the bottom and top parts. From the other perspectives, it is known that these domains are connected along the z-direction. One finds a superposition of both a checkerboard- and sheet-like pattern, resulting in a maze-like formation along the easy magnetic axis.

Domain width estimation

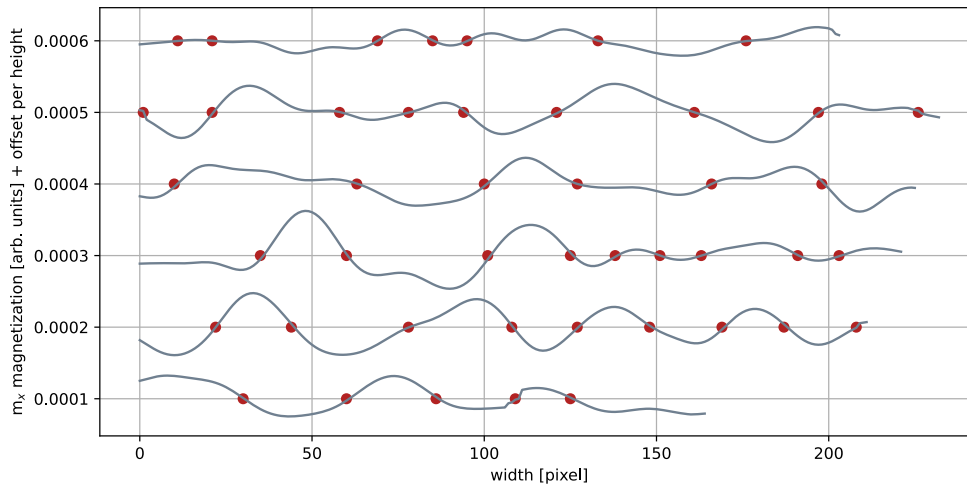


Figure 5.24.: Zero crossings of the magnetization along the y-direction sliced along the center of the x-direction.

We use a Monte Carlo approach to estimate the sample's domain width because of the relatively large dataset size. Since the domain structure is pointing mostly in only the x-direction, line profiles can be placed randomly in the sample perpendicular to the x-direction. The line profile (see figure 5.24) is used to determine the number of pixels (and therefore distance) between the zero crossings of the magnetic moment in the x-direction. The line profile from the slices around the middle point of the 3D magnetic structure and the reference point in the other directions can be

seen in figure 5.24. One can now slice the 3D magnetic structure multiple times and extract the line profile along the y-direction to see the zero crossings of the m_x magnetization. The line profiles of the m_x magnetization are shown as representative. Here, the 3D magnetic structure was sliced along the central point of the x-direction. Each line profile is about 27 pixels or 1 μm apart.

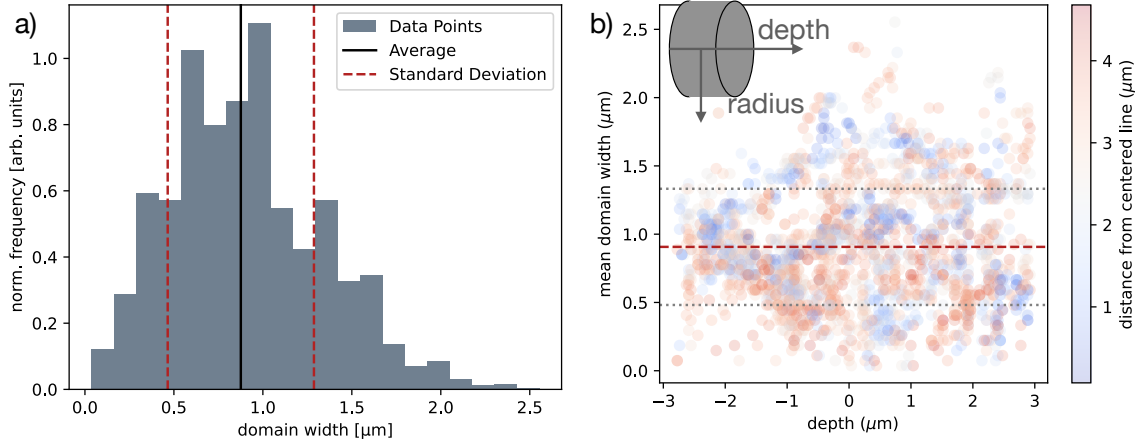


Figure 5.25.: a) histogram of all domain widths obtained by the data set, b) radially dependent domain width concerning the middle point of x-y.

The result of summing up all contributions can be found in figure 5.25a). One can see that the average domain width is ca. 0.889 μm along the y-direction. The distribution is slightly asymmetric, with a flatter tail towards the larger domain widths. Domains up to 2.5 μm can be found within the sample. To check if there is a dependence on the depth or distance from the central rotation axis of the cylindrical sample. This can be seen in figure 5.25b). The average domain width per line scan is not dependent on the distance from the center line. Fewer larger domain widths exist between the bottom -3 and -1 μm . Since this is not symmetric around the central slice of the sample, it can be assumed that it is coming from the sample properties instead of surface effects. This could be due to more inclusions in the lower part of the sample (see following paragraph). In general, the results are in good agreement with the findings of literature for these types of magnets (see reference [140]).

Nd-rich inclusions and effect on the domain structure

During the 3D magnetic structure analysis, multiple Nd-rich islands could be identified within the reconstruction of the non-magnetic XAS (see figure 5.26). This can be obtained from the measurement via not the subtraction of plus and minus circularly polarized light but by addition. These islands show different absorption coefficients at specific spots, visible by high concentrations of Nd. Nd aggregations can be found in the sample presented in this thesis. This is not unusual for Nd-Fe-B-type magnetic materials [150] and could be due to a flake boundary from the melt-spin process. The Nd-rich inclusions start at around 1 μm and continue randomly until the end of the sample at ca. 3 μm in x-direction.

In the lower region of the sample with more Nd islands, a slightly smaller domain width can be seen if one compares it to the upper part of the sample (see figure 5.25b)). This effect could be due to the paramagnetic Nd in that area, reducing

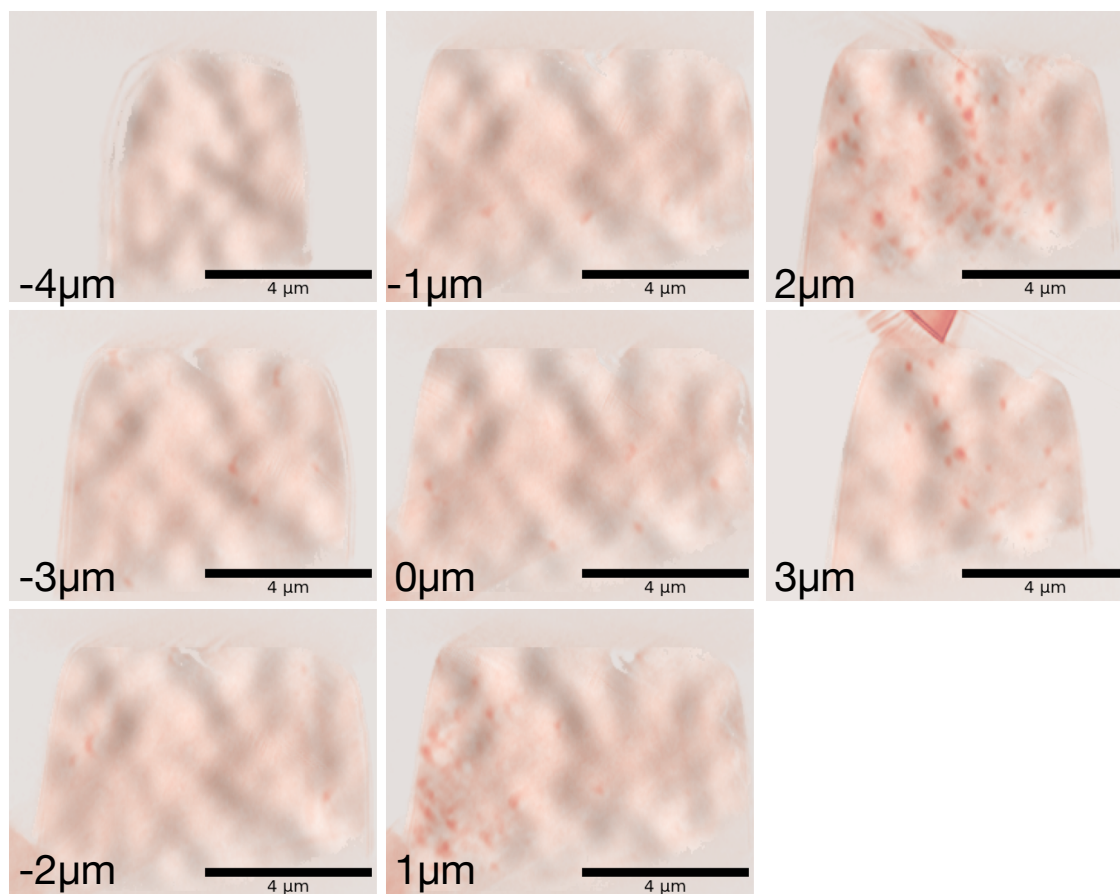


Figure 5.26.: Overlay slices through the sample along the sample x-direction. Magnetization in x-direction plotted (black and white contrast) with the XAS signal (dark red spots), showing the Nd-rich inclusions.

the anisotropy energy. However, a larger sample size must be analyzed utilizing advanced measurement and evaluation techniques to arrive at a more definitive conclusion.

Element-specific anisotropy of Nd

In recent XMCD studies, an element-specific anisotropy was observed in $\text{Nd}_2\text{Fe}_{14}\text{B}$ systems [154]. It comes most probable from the RE sublattices. The Fe provides the magnetization. Studies on the magnetic structure were performed by Givord et al. [168]. Haskel et al. [169] show by dichroic resonant diffraction of circularly polarized X-rays, that intrinsic magnetic stability around the c-axis arises predominately at one of the Nd sites (g). In contrast, other RE site (f) undermines magnetic stability by favoring a magnetic moment orientation in the basal plane (compare to figure 5.1). This means that the XMCD effect on the Nd has different contributions depending on the direction in which it is measured and when measured in saturation. This effect does not significantly add to the error in this work since it can be assumed that in the demagnetized state, the only direction of the magnetization is the easy axis (c-axis).

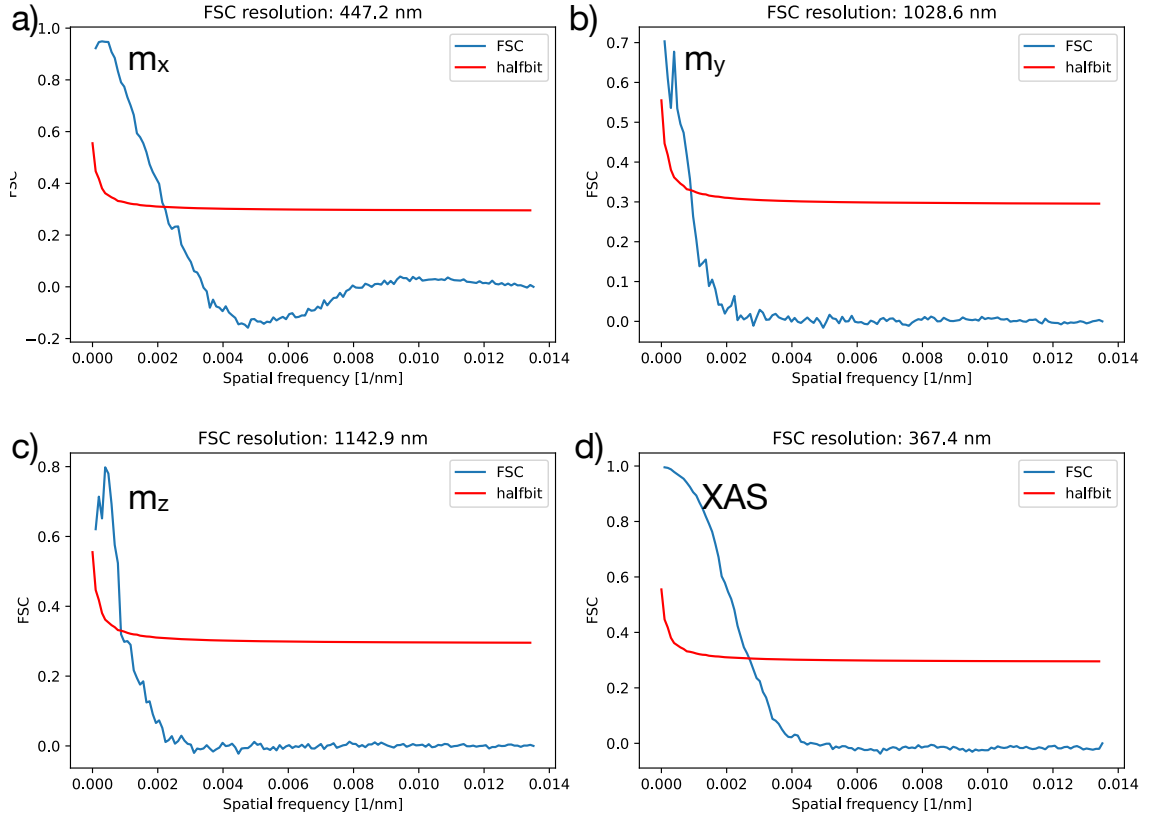


Figure 5.27.: Fourier shell correlation of magnetization in a) x-direction, b) y-direction, and c) z-direction.

Resolution estimation via Fourier shell correlation

The resolution of the lensless imaging measurement can be performed using equation (3.13) discussed in the theory section. With the help of this formula, one compares the Fourier transform of two individually analyzed 3D reconstructions with half of the dataset. The calculated result can be found in figure 5.27. The subfigure for m_x shows, where one can see that in the magnetic dominant x-direction, the magnetization reaches spatial frequency halfbit threshold later, meaning a larger spatial resolution in the x-component of the magnetization of about 450 nm. The resolution is worse for the y and z magnetization and can be seen in b) and c), respectively, and reaches about 1 μm . The resolution of the non-magnetic reconstruction can be found in d), which reaches even higher resolutions than the magnetization along the x-component of about 370 nm.

6. Conclusion and outlook

The presented work evaluated rare-earth-containing model systems like Nd-Fe-B and RE-Co-based systems via synchrotron-based techniques like extended X-ray absorption fine structure (EXAFS), X-ray absorption near-edge spectroscopy (XANES), X-ray magnetic circular dichroism (XMCD), and X-ray magnetic laminography. Working with large research facilities like synchrotrons requires a lot of organization, competition, and multiple people per beam time, which was especially difficult during the time of COVID-19. However, this work has displayed a consistent level of output in beam times and research contributions over the past 4 years. This chapter will first give a conclusion of the thesis and then an outlook on how, especially the work pursued in this thesis, could be continued in the upcoming years.

6.1. Conclusion of this thesis

Element-specific investigations of RE-Co systems

This thesis showed the intrinsic magnetic properties of the RE-Co model systems by utilizing techniques like EXAFS, XANES, and XMCD. The first part describes the success of growing the SmCo_5 and $\text{Sm}_2\text{Co}_{17}$ phases in one thin film. This work showed that both phases coexist and that the decomposition of these phases happens naturally, with a smooth boundary and a strong coupling between the phases. The epitaxial strain energy stabilizes the SmCo_5 phase up to a thickness of 4 nm, above which a matrix of $\text{Sm}_2\text{Co}_{17}$ with nanoscale intermixed SmCo_5 is observed. EXAFS analysis showed a novel way to quantify such crystallographically complex phases reliably. The best fit of the EXAFS spectrum revealed the presence of about 35% SmCo_5 and 65% $\text{Sm}_2\text{Co}_{17}$. The observed magnetization of the film is consistent with the total of magnetizations in a magnetically exchange-coupled system. The magnetocrystalline anisotropy and magnetic hardness of the film reflect the nanoscale architecture of the film comprising SmCo_5 and $\text{Sm}_2\text{Co}_{17}$ phases with coherent interfaces.

How Sm and Co couple under the influence of Cu could be successfully shown by utilizing XMCD. The magnetic moments of Sm and Co decouple with increasing content of Cu, which can be observed in the element-specific hysteresis curves. XMCD was combined with a technique called X-ray excited optical luminescence, verifying our findings through the whole magnetic thin film. The XMCD investigation of these highly crystalline $\text{SmCo}_{5-x}\text{Cu}_x$ thin films grown by molecular beam epitaxy on Al_2O_3 substrates, in conjunction with advanced computational and characterization techniques, has unveiled that Cu substitution also enhances the intrinsic magnetic anisotropy, accompanied by an increase in coercivity.

In the (Y, Ce) Co_5 systems, it was possible to correlate the hard X-ray and soft X-ray measurements in thin films to determine the Ce oxidation state. This is important since in the soft X-ray region, the magnetically important Ce 4*f* electron states

are probed. With the correlation to hard X-ray region, expectations about the magnetism can be drawn from the more robust Ce L₃-edge. In addition, HERFD-XANES is shown for a bulk material series, which shows peculiarities that can be explained via the change in lattice distances rather than the change in Ce valence, which also plays an important role in the distribution of the 5*d* states.

Interaction domains in Nd₂Fe₁₄B studied in three dimensions

For the first time, the observation of the (interaction) domain structure from the sample surface was extended into the bulk, providing a comprehensive view of the domain arrangement throughout an entire hot-deformed ca. 9 μm by 6 μm sample. This breakthrough underscores the effectiveness of magnetic laminography as a non-destructive tool for studying domains in bulk-like permanent magnetic samples.

Our demonstration involved the measurement and reconstruction of the 3D complex magnetic structure within a hot-deformed anisotropic nanocrystalline Nd₂Fe₁₄B sample, achieving a spatial resolution of approximately 450 nm along the direction of the largest magnetic contribution aligned with the structural c-axis of the individual grains. Macroscopic measurements revealed the distinctive behavior of interaction domains during the first magnetization curve along the easy direction of the hot-deformed permanent magnet Nd-Fe-B. Our measurements and magnetic reconstruction provided compelling evidence of a predominant alignment of magnetic domains parallel to the preferred magnetic axis (c-axis) in a stripe-like fashion, spanning across multiple grains as interaction domains, with no indication of flux closure domains. In all other directions, the sample showed an intricate structure of interconnected magnetic domains.

6.2. Outlook

Although this work has shown interesting results, this work also sets the stage for many proceeding experiments. These paragraphs propose shortly how one could continue with further measurements.

Magnetic thin films

The analysis routines created during this work can be used for high-throughput XMCD with gradient tertiary Sm–Co–X thin films. Here, extensive work by the group of Nora Dempsey at the CNRS in Kerr and XRD-analysis has been done. Still, the element-specific magnetization into the different compounds would be an insightful addition. Especially the measurement of the induced moment in Cu.

We found an ordered and unordered phase in the binary phases of a Sm–Co thin film. The XMCD of this sample shows an anisotropic signal on the Co but not on the Sm. Here, more angle-resolved XMCD investigations would be beneficial for further research.

Oxidation was encountered partially during measurements of the (Y, Ce)–Co systems. However, valuable information could be extracted, as it was discussed in the previous section. Nevertheless, the total electron yield measurement could not obtain a magnetic signal. Later, the luminescence signal was also not able to get

a magnetic signal of the Ce because the film was at this time fully oxidized. For further measurements, I suggest the preparation of a sufficient capping layer (e.g., 10 nm Pt) on top of the highly oxidizing Ce-containing thin films. When grown on substrates like MgO or Al₂O₃, one can measure the XMCD directly via luminescence detection.

3D magnetization

Although we achieved a relatively high resolution with the magnetic laminography measurements, currently, our spatial resolution allows us to map the domain structure but not the underlying characteristics of the domain walls. However, we anticipate significant future spatial resolution improvements, thanks to advancements and upgrades in synchrotron light sources coupled with increased photon flux and, therefore, a higher signal-to-noise ratio. This will enable us to determine the underlying textures in permanent magnets, shedding light on the 3D domain structures in these complex systems, especially at grain boundaries. For the 3D magnetization measurements, there would be the following suggestion. However, the domain walls and the magnetic distribution of moments closer to the domain walls could not be imaged. But the domains show an interesting behavior of themselves. We find that much better resolutions are required for the magnetic imaging of the domain walls. This could also be achieved non-destructively using soft X-ray ptychography-based techniques requiring much thinner samples. With a domain size of ca. 0.9 μm , one needs about 2 μm of sample to get at least one domain wall within the sample. At this thickness, only about 1% of the incoming beam is transmitted. Using soft X-ray measurements would enhance the magnetic signal, with the XMCD signal normalized to the white line improving by approximately tenfold. Consequently, by increasing the scan point density and extending the illumination time, one can anticipate a substantial enhancement in structural resolution.

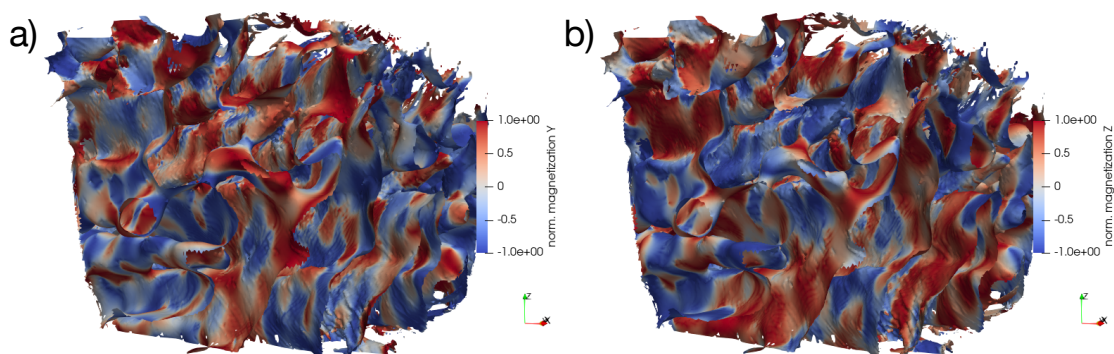


Figure 6.1.: Magnetization on m_x domain walls along a) y-direction and b) z-direction.

In which direction the upcoming research could go can be seen by analyzing the data beyond the resolution limit. The pre-assessment of the data hints at domain patterns on the domain walls. In figure 6.1a) and b), the domain walls are depicted; on the domain walls, the magnetization along a) y-direction and b) z-direction is shown. This could indicate that, in general, the morphology of the domain walls is somewhere between Néel and Bloch walls. As mentioned, the resolution along the magnetic y- and z-direction is relatively low. Splitting the measured dataset into

two, as done for the Fourier shell correlation, revealed that the noise was too high to retrieve solid evidence. Further investigation of the domain structure is required. It will be performed with a smaller piece of sample and higher resolution to map the magnetization within the domain walls—for example, soft X-ray tomographic measurements at the Cosmic beamline at the ALS in Berkeley.

Another direction to go, which a lot of groups are going, is to measure with different applied magnetic fields. Especially in the sample presented in this work, it would be interesting to study how the Nd-rich inclusions will interact with the domain walls during the magnetic reversal process. However, since the total measurement time for the dataset presented was around 3 days, one has to come up with ideas on how to shorten the measurement time while keeping the data quality sufficiently high.

Research Contributions

During my time as a Ph.D. student and a strong involvement within the research framework CRC/TRR270, I had the opportunity to contribute to many beam times, visits, or projects. The contributions range from peer-reviewed papers to contributing open source computer code for data analysis.

Peer-reviewed publications

Element-Specific Study of Magnetic Anisotropy and Hardening in $\text{SmCo}_{5-x}\text{Cu}_x$ Thin Films 09/2023

G. Gkouzia, D. Günzing et al., Inorg. Chem., XXXX-XXXX
<https://doi.org/10.1021/acs.inorgchem.3c01768>

Role of kinetic energy on Nb3Sn thin films by low-temperature co-sputtering 07/2023

N. Schäfer, D. Günzing et al., J. Appl. Phys. 134 (4): 043903
<https://doi.org/10.1063/5.0145181>

Formation of precipitates in off-stoichiometric Ni–Mn–Sn Heusler alloys probed through the induced Sn-moment 06/2023

B. Eggert, A. Cakir, D. Günzing et al., RSC advances 13, 18217-18222
<https://doi.org/10.1039/D3RA01420G>

Spatially-resolved dynamic sampling of different phasic magnetic resonances of nanoparticle ensembles in a magnetotactic bacterium *Magnetospirillum Magnetotacticum* 04/2023

T. Feggeler, J. Lill, D. Günzing et al., New J. Phys. 25 043010
<https://doi.org/10.1088/1367-2630/acc81f>

Autonomous atomic Hamiltonian construction and active sampling of X-ray absorption spectroscopy by adversarial Bayesian optimization 03/2023

Y. Zhang, R. Xie, T. Long, D. Günzing et al., npj Computational Materials, 23, 9, 46,
<https://doi.org/10.1038/s41524-023-00994-w>

Tailoring magnetic anisotropy by graphene-induced selective skyhook effect on 4f-metals 05/22

A. Herman, S. Kraus, S. Tsukamoto, L. Spieker, V. Caciuc, T. Lojewski, D. Günzing, et al., Nanoscale, 2022, 14, 7682-7691,
<https://doi.org/10.1039/D2NR01458K>

Towards a mechanistic understanding of the sol–gel syntheses of ternary carbides 02/22

J. P. Siebert, M. Juelscholt, **D. Günzing** et al., *Inorg. Chem. Front.*, 2022,9, 1565-1574,

<https://doi.org/10.1039/D2QI00053A>

Strain- and field-induced anisotropy in hybrid elastomers with elongated filler nanoparticles 07/21

J. Seifert, **D. Günzing** et al., *Inorg. Chem. Front.*, *Soft Matter*, 2021,17, 7565-7584,

<https://doi.org/10.1039/D0SM02104K>

Epitaxy Induced Highly Ordered Sm₂Co₁₇–SmCo₅ Nanoscale Thin-Film Magnets 06/21

S. Sharma, A. Zinter, **D. Günzing** et al., *ACS Appl. Mater. Interfaces* 2021, 13, 27, 32415–32423

<https://doi.org/10.1021/acsami.1c04780>

Conferences and workshops

Poster: Insights into hot-deformed anisotropic Nd₂Fe₁₄B magnets: Interaction domains studied by non-destructive 3D magnetic laminography and magnetometry 09/23

Rare-Earth Permanent Magnets in Birmingham, UK

Talk: XMCD investigation on Sm-Co magnetic thin films: strong orbital pinning on Co and the role of Sm 09/22

DPG condensed matter section in Regensburg, Germany

Talk: XAS investigations on magnetic systems – towards microscopic understanding and tailoring hysteresis 11/21

Photon Science meeting at Advanced Light Source, Lawrence Berkeley National Laboratory

Poster: Complex nanostructured magnetic thin films investigated by x-ray absorption spectroscopy 09/21

DPG condensed matter section virtual meeting

Workshop on magnetism for 2 weeks 09/21

European School on Magnetism in Cluj, Romania

Talk: Induced orientation of hematite nanospindles studied via Mössbauer spectroscopy 03/20

CENIDE Conference in Bergisch Gladbach, Germany

Exchanges and visits

Visiting PhD student 06/22 - 08/22

Magnetic spectroscopy group, Lawrence Berkeley National Laboratory, Berkeley, CA, US

Visiting PhD student 10/21 - 11/21

Magnetic spectroscopy group, Lawrence Berkeley National Laboratory, Berkeley, CA, US

Open Source Software contributions

xaspy: Python module XMCD evaluation and fast evaluation of synchrotron measurements: initiator 2020 - today

D. Günzing 10.5281/zenodo.7847593

Xraylarch: X-ray Analysis for Synchrotron Applications using Python, commit 1e9a2e6, 231f0ed, 1e83d16 2020

M. Newville, B. Ravel, M. Rovezzi, mkak, Bob620, M. Rakinin, D. Günzing, et al., xraypy/xraylarch 0.9.48 (0.9.48). Zenodo. <https://doi.org/10.5281/zenodo.4067344>

Attended beam times

Soft XMCD - multiple beam times 06/22 - 08/22

6.3.1, ALS, Berkeley, CA, US

Hard X-ray 3D laminography 05/22

cSAXS, SLS, Villigen, CH

EXAFS 04/22

P65, DESY, Hamburg, DE

Hard XMCD 12/21

P09, DESY, Hamburg, DE

Soft XMCD - multiple beam times 10/21 - 11/21

6.3.1[§] 4.0.2, ALS, Berkeley, CA, US

Hard XMCD 07/21

ID12, ESRF, Grenoble, FR

Soft STXM 07/21

MAXYMUS, BESSY, Berlin, DE

Soft XMCD (remote) 06/21

6.3.1, ALS, Berkeley, CA, US

Soft XMCD 12/20

PM3, BESSY, Berlin, DE

Soft XMCD 10/20

PM2-VEKMAG, BESSY, Berlin, DE

XRD (remote) 09/20

ID22, ESRF, Grenoble, FR

μ XAS mapping and EXAFS (remote) 09/20

ID-20, APS, Chicago, US

EXAFS (remote) 08/20

ID-20, APS, Chicago, US

Soft XMCD 02/20

UE46_PGM-1, BESSY, Berlin, DE

Soft XMCD 01/20

PM2-VEKMAG, BESSY, Berlin, DE

Appendices

A. Derivation of sum rules for $3d$ and $4f$ systems

In this part we will derive the sum rules for XMCD from the original source, these can be found in references by Carra, Thole, Koenig, Sette, Altarelli, van der Laan, and Wang [52–54]. We can use the following to derive the actual magnetic moments connected to the states:

$$\begin{aligned}\mu_l &= -\langle L_z \rangle \cdot \mu_B \\ \mu_s &= -2 \cdot \langle S_z \rangle \cdot \mu_B\end{aligned}$$

We use the following approximation

$$\begin{aligned}\mu'_{\text{XAS}} &= \mu^+ + \mu^- + \mu^0 \\ &\approx \mu^+ + \mu^- + \frac{\mu^+ + \mu^-}{2} \\ &= \frac{3}{2} (\mu^+ + \mu^-),\end{aligned}\tag{A.1}$$

with μ^0 denoting linear polarization, and μ^- denoting right and μ^+ left circular polarization. This is important to notice, since during the experimentation at the beamline usually only left and right circular polarized will be used, or the field will be switched with the same circular polarization, or both.

The sum rules as found in references are [52–54]:

$$\begin{aligned}\langle S_z \rangle &= \frac{\int_{j_+} d\omega(\mu^+ - \mu^-) - [(c+1)/c] \int_{j_-} d\omega(\mu^+ - \mu^-)}{\int_{j_+ + j_-} d\omega(\mu^+ + \mu^- + \mu^0)} \cdot \frac{3c(4l+2-n)}{l(l+1) - 2 - c(c+1)} \\ &\quad - \frac{3c(l(l+1)[l(l+1) + 2c(c+1) + 4] - 3(c-1)^2(c+2)^2)}{(l(l+1) - 2 - c(c+1)) \cdot 6lc(l+1)} \langle T_z \rangle,\end{aligned}\tag{A.2}$$

where $\langle T_z \rangle$ is the magnetic dipole tensor, c and l are the initial and final orbital respectively ($s, p, d, f, \dots = 0, 1, 2, 3, \dots$). Which edges are integrated within the measured signal are described by $j_{\pm} = c \pm 1/2$. n is the number of electrons in the final shell. The magnetic orbital moment $\langle L_z \rangle$ with the same sign conventions can be written as:

$$\langle L_z \rangle = \frac{\int_{j_++j_-} d\omega(\mu^+ - \mu^-)}{\int_{j_++j_-} d\omega(\mu^+ + \mu^- + \mu^0)} \cdot \frac{2l(l+1)(4l+2-n)}{l(l+1)+2-c(c+1)} \quad (\text{A.3})$$

For the calculation of the moments we use for $L_{2,3}$ -edges $c = 1$ and $l = 2$, and for the $M_{4,5}$ -edges $c = 2$ and $l = 3$. We use the approximation from equation (A.1). For the $L_{2,3}$ -edges we can write:

$$\begin{aligned} \langle S_z \rangle &= (10-n) \frac{\int_{j_+} d\omega(\mu^+ - \mu^-) - 2 \int_{j_-} d\omega(\mu^+ - \mu^-)}{\frac{3}{2} \int_{j_++j_-} d\omega(\mu^+ + \mu^-)} \\ &\cdot \frac{3}{6-2-2} - \frac{3(6[6+4+4]-0)}{(6-2-2) \cdot 36} \langle T_z \rangle \\ &= (10-n) \frac{\int_{j_+} d\omega(\mu^+ - \mu^-) - 2 \int_{j_-} d\omega(\mu^+ - \mu^-)}{\frac{3}{2} \int_{j_++j_-} d\omega(\mu^+ + \mu^-)} \\ &\cdot \frac{3}{2} - \frac{3(6[14]-0)}{2 \cdot 36} \langle T_z \rangle \\ &= (10-n) \frac{\int_{j_+} d\omega(\mu^+ - \mu^-) - 2 \int_{j_-} d\omega(\mu^+ - \mu^-)}{\int_{j_++j_-} d\omega(\mu^+ + \mu^-)} - \frac{7}{2} \langle T_z \rangle. \end{aligned} \quad (\text{A.4})$$

Calculating $\langle L_z \rangle$ for the 3d transitions:

$$\begin{aligned} \langle L_z \rangle &= (10-n) \frac{\int_{j_++j_-} d\omega(\mu^+ - \mu^-)}{\frac{3}{2} \int_{j_++j_-} d\omega(\mu^+ + \mu^-)} \cdot \frac{12}{6+2-2} \\ &= (10-n) \frac{4 \int_{j_++j_-} d\omega(\mu^+ - \mu^-)}{3 \int_{j_++j_-} d\omega(\mu^+ + \mu^-)} \end{aligned} \quad (\text{A.5})$$

For the 4f rare earth metals (the $M_{4,5}$ -edges), we use $c = 2$ and $l = 3$:

$$\begin{aligned}
\langle S_z \rangle &= (14 - n) \frac{\int_{j_+} d\omega(\mu^+ - \mu^-) - [3/2] \int_{j_-} d\omega(\mu^+ - \mu^-)}{\frac{3}{2} \int_{j_+ + j_-} d\omega(\mu^+ + \mu^-)} \cdot \frac{6}{3(4) - 2 - 2(3)} \\
&\quad - \frac{6(3(4)[3(4) + 4(3) + 4] - 3(1)^2(4)^2)}{(3(4) - 2 - 2(3)) \cdot 36(4)} \langle T_z \rangle \\
&= (14 - n) \frac{\int_{j_+} d\omega(\mu^+ - \mu^-) - [3/2] \int_{j_-} d\omega(\mu^+ - \mu^-)}{\frac{3}{2} \int_{j_+ + j_-} d\omega(\mu^+ + \mu^-)} \cdot \frac{6}{12 - 2 - 6} \\
&\quad - \frac{6(12[12 + 12 + 4] - 48)}{4 \cdot 144} \langle T_z \rangle \\
&= (14 - n) \frac{\int_{j_+} d\omega(\mu^+ - \mu^-) - [3/2] \int_{j_-} d\omega(\mu^+ - \mu^-)}{\frac{3}{2} \int_{j_+ + j_-} d\omega(\mu^+ + \mu^-)} \cdot \frac{3}{2} - \frac{1728}{576} \langle T_z \rangle \\
&= (14 - n) \frac{\int_{j_+} d\omega(\mu^+ - \mu^-) - [3/2] \int_{j_-} d\omega(\mu^+ - \mu^-)}{\int_{j_+ + j_-} d\omega(\mu^+ + \mu^-)} - 3 \langle T_z \rangle \tag{A.6}
\end{aligned}$$

Calculating $\langle L_z \rangle$ for the 4f transitions as follows:

$$\begin{aligned}
\langle L_z \rangle &= (14 - n) \frac{\int_{j_+ + j_-} d\omega(\mu^+ - \mu^-)}{\frac{3}{2} \int_{j_+ + j_-} d\omega(\mu^+ + \mu^-)} \cdot \frac{6(4)}{3(4) + 2 - 2(3)} \\
&= (14 - n) \frac{\int_{j_+ + j_-} d\omega(\mu^+ - \mu^-)}{\frac{3}{2} \int_{j_+ + j_-} d\omega(\mu^+ + \mu^-)} \cdot \frac{24}{8} \\
&= (14 - n) \cdot 2 \frac{\int_{j_+ + j_-} d\omega(\mu^+ - \mu^-)}{\int_{j_+ + j_-} d\omega(\mu^+ + \mu^-)} \tag{A.7}
\end{aligned}$$

With neglecting the $\langle T_z \rangle$ the term is usually called the effective spin $\langle S_z^{\text{eff}} \rangle$. When neglecting the $\langle L_z \rangle$, and calculate the effective spin moment $\langle S_z^{\text{eff}} \rangle$, you can see that the non-magnetic XAS part $\int_{j_+ + j_-} d\omega(\mu^+ + \mu^-)$ and the number of electrons in the shell n are in both equations. Which means that you can calculate the orbital to effective spin moment only with the XMCD spectra.

B. Preparation by focussed ion beam

In this part of the appendices, the focussed ion beam (FIB) process is used and described in chapter 5 is described in more detail. The bulk sample material had to be cut to prepare the samples for the experiment at the Swiss Light Source (SLS). During the (FIB) preparation process, these additionally needed to be placed on a SiN membrane. In figure B.1 this process is described in more detail because due to the restriction of movement of the machine, it was not as straightforward as first thought.

Before cutting out the sample from the bulk material, a small Pt stripe is applied on the SiN membrane for later guidance in the experiment. The Pt stripe is applied in such a way that it points toward the middle of the membrane (as can be seen in figure 5.4b)). In image 1 the sample is shown from two directions, from the side (left), and from the top (right). The sample is glued to the sample holder with double-sided C tape. The sample is about 50 μm thick and polished at the surface. The FIB cuts are shown in blue. In step 2 the front of the sample is flattened with the Ga ion beam, to have a clean front surface to work with. In the third step, a FIB cut is introduced from the side. It should leave as much sample material below the surface, as one intends the cutout sample to be thick. The cut from the side should be also deep enough so that the next step can be performed without any issues. In step 4 a template will be used for the main disc shape. It is important that a small bridge stays connected with the main sample material, so the cutout sample disc does not fall. In the next step, the manipulator (indicated in the sketch as a red arrow) will be soldered with Pt to the sample. In step 6 the bridge between the main sample material and the cutout disc will be separated. In the next step, the bottom of the sample can be brought in flattened if this is necessary. The sample will be moved close to the SiN and soldered with a little bit of Pt to the membrane surface (as can be seen in figure 5.4c)). In the last step, the connection between the manipulator and the disc is cut by the Ga ion beam. Due to the angle restrictions of the FIB machine, this will cut a small hole into the membrane, which is not of concern.

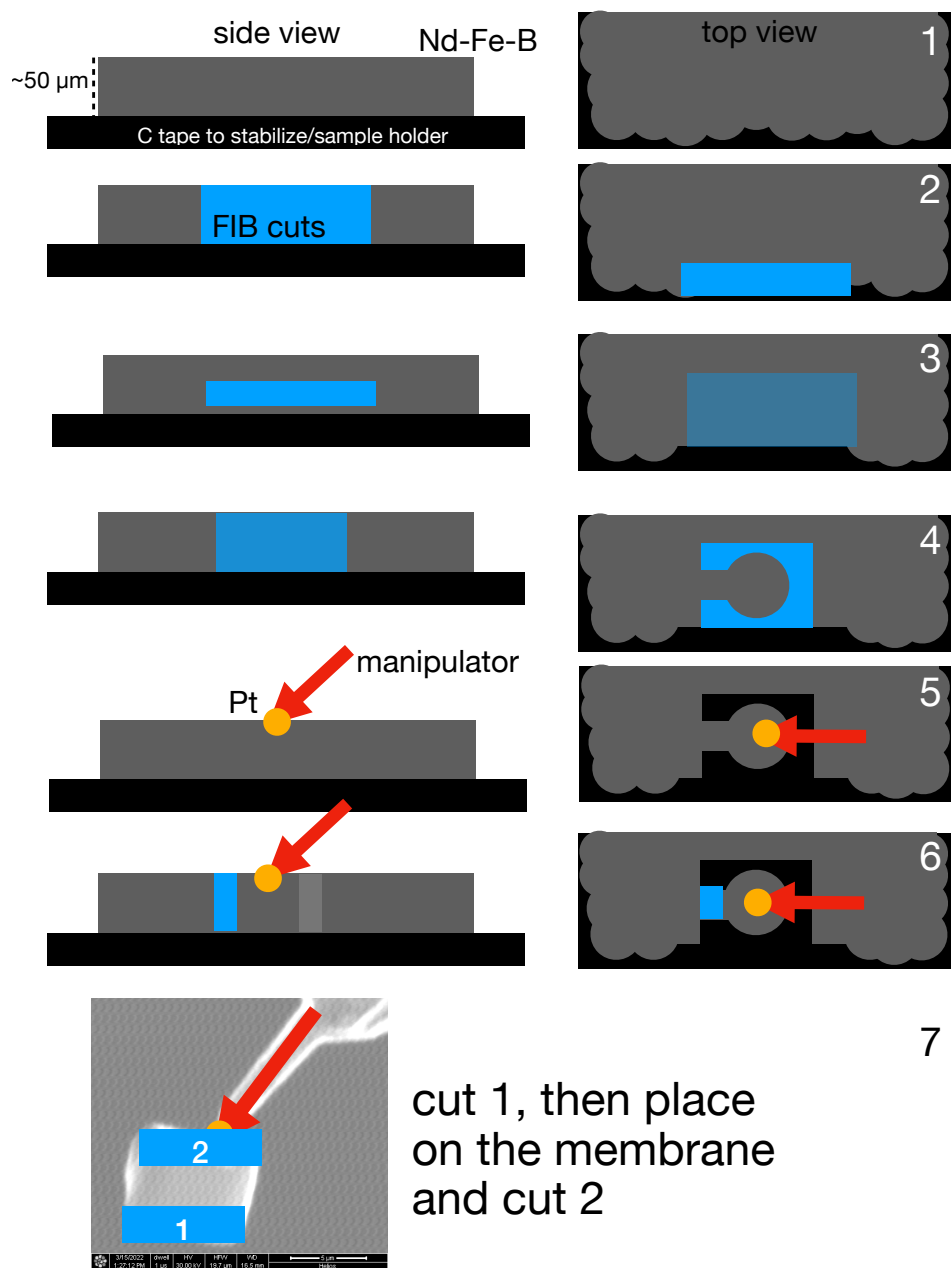


Figure B.1.: Schematics of sample preparation by FIB. Numbers not to scale. Step-by-step description in the text.

Bibliography

- [1] Pavel, Lacal-Arántegui, Marmier, Schüler, Tzimas, Buchert, Jenseit, and Blagoeva. Substitution strategies for reducing the use of rare earths in wind turbines. *Resources Policy*, 52:349–357, 2017. [cited on page 1]
- [2] Langkau and Erdmann. Environmental impacts of the future supply of rare earths for magnet applications. *Journal of Industrial Ecology*, 25(4):1034–1050, 2021. [cited on page 1]
- [3] Zapp, Schreiber, Marx, and Kuckshinrichs. Environmental impacts of rare earth production. *MRS Bulletin*, 47(3):267–275, 2022. [cited on page 1]
- [4] European Raw Materials Alliance ‘Rare Earth Magnets and Motors : A European Call for Action’. 2021. [cited on page 1]
- [5] Skokov and Gutfleisch. Heavy rare earth free, free rare earth and rare earth free magnets - Vision and reality. *Scripta Materialia*, 154:289–294, 2018. [cited on pages 1 and 10]
- [6] Eggert, Çakır, Günzing, Josten, Scheibel, Brand, Farle, Acet, Wende, and Ollefs. Formation of precipitates in off-stoichiometric Ni–Mn–Sn Heusler alloys probed through the induced Sn-moment. *RSC Advances*, 13(27):18217–18222, 2023. [cited on page 2]
- [7] Siebert, Juelsholt, Günzing, Wende, Ollefs, and Birkel. Towards a mechanistic understanding of the sol–gel syntheses of ternary carbides. *Inorganic Chemistry Frontiers*, 9(7):1565–1574, 2022. [cited on page 2]
- [8] Skokov, Karpenkov, Karpenkov, Radulov, Günzing, Eggert, Rogalev, Wilhelm, Liu, Shao, Ollefs, Gruner, Wende, and Gutfleisch. A multi-stage, first-order phase transition in LaFe_{11.8}Si_{1.2}: Interplay between the structural, magnetic, and electronic degrees of freedom. *Applied Physics Reviews*, 10(3), 2023. [cited on page 2]
- [9] Schäfer, Günzing, Jiang, Karabas, Arzumanov, Motta-Meira, Ollefs, Komissinskiy, Major, Arnold, Pietralla, Wende, Molina-Luna, Lützenkirchen-Hecht, and Alff. Role of kinetic energy on Nb₃Sn thin films by low-temperature co-sputtering. *Journal of Applied Physics*, 134(4), 2023. [cited on pages 2 and 19]
- [10] Keithley. *The Story of Electrical and Magnetic Measurements: From 500 BC to the 1940s*. Wiley, 1999. [cited on page 5]
- [11] Coey. Perspective and Prospects for Rare Earth Permanent Magnets. *Engineering*, 6(2):119–131, 2020. [cited on page 7]

- [12] Coey. *Magnetism and Magnetic Materials*. Cambridge University Press, Cambridge, 2010. [cited on pages 7, 8, 10, 12, 14, and 29]
- [13] Liu, Sellmyer, and Shindo. Handbook of Advanced Magnetic Materials: Vol 1. Nanostructural Effects. Vol 2. Characterization and Simulation. Vol 3. Fabrication and Processing. Vol 4. Properties and Applications. 2008. [cited on pages 7 and 10]
- [14] Krishnan. *Fundamentals and applications of magnetic materials*. Oxford University Press, 2016. [cited on pages 7 and 13]
- [15] Chikazumi and Graham. *Physics of ferromagnetism*. Oxford university press, 1997. [cited on pages 8 and 11]
- [16] Van Dyck, Schwinberg, and Dehmelt. Electron magnetic moment from geonium spectra: Early experiments and background concepts. *Physical Review D*, 34(3):722–736, 1986. [cited on page 8]
- [17] Van Vleck. On the anisotropy of cubic ferromagnetic crystals. *Physical Review*, 52(11):1178, 1937. [cited on page 9]
- [18] Bruno. Tight-binding approach to the orbital magnetic moment and magnetocrystalline anisotropy of transition-metal monolayers. *Physical Review B*, 39(1):865–868, 1989. [cited on page 9]
- [19] Sepehri-Amin, Tamazawa, Kambayashi, Saito, Takahashi, Ogawa, Ohkubo, Hirosawa, Doi, Shima, and Hono. Achievement of high coercivity in Sm(Fe_{0.8}Co_{0.2})₁₂ anisotropic magnetic thin film by boron doping. *Acta Materialia*, 194:337–342, 2020. [cited on page 9]
- [20] Coey. *Rare-earth Iron Permanent Magnets*. Clarendon Press, 1996. [cited on pages 9 and 29]
- [21] Skomski and Sellmyer. Anisotropy of rare-earth magnets. *Journal of Rare Earths*, 27(4):675–679, 2009. [cited on page 9]
- [22] Rinehart and Long. Exploiting single-ion anisotropy in the design of f-element single-molecule magnets. *Chemical Science*, 2(11):2078–2085, 2011. [cited on page 9]
- [23] Cullity and Graham. *Introduction to magnetic materials*. John Wiley & Sons, 2011. [cited on page 10]
- [24] Coey and Parkin. *Handbook of Magnetism and Magnetic Materials*. Springer International Publishing AG, 2022. [cited on pages 10, 29, and 38]
- [25] Li, Tang, Sepehri-Amin, Ohkubo, Hioki, Hattori, and Hono. On the temperature-dependent coercivities of anisotropic Nd-Fe-B magnet. *Acta Materialia*, 199:288–296, 2020. [cited on page 10]
- [26] Dennis, Borges, Buda-Prejbeanu, Ebels, Gregg, Hehn, Jouguelet, Ounadjela, Petej, Prejbeanu, and Thornton. The defining length scales of mesomagnetism: A review. *J. Phys.: Condens. Matter*, 14:1175–1262, 2002. [cited on page 11]

-
- [27] O’handley. *Modern magnetic materials: principles and applications*. Wiley, 2000. [cited on page 12]
- [28] Kronmuller and Kronmüller. *Micromagnetism and the microstructure of ferromagnetic solids*. Cambridge university press, 2003. [cited on page 12]
- [29] Brown. Virtues and Weaknesses of the Domain Concept. *Reviews of Modern Physics*, 17(1):15–19, 1945. [cited on pages 12 and 14]
- [30] Zhao, Zhao, Lim, Feng, and Ong. From nucleation to coercivity. *Applied Physics Letters*, 87(16), 2005. [cited on page 12]
- [31] Zhao and Wang. Nucleation, pinning, and coercivity in magnetic nanosystems: An analytical micromagnetic approach. *Physical Review B*, 74(1):012409, 2006. [cited on page 12]
- [32] Kronmüller and Goll. Micromagnetic analysis of nucleation-hardened nanocrystalline PrFeB magnets. *Scripta Materialia*, 47(8):551–556, 2002. [cited on page 12]
- [33] Kronmüller and Goll. Micromagnetic analysis of pinning-hardened nanostructured, nanocrystalline Sm₂Co₁₇ based alloys. *Scripta Materialia*, 47(8):545–550, 2002. [cited on page 12]
- [34] Buschow. *Handbook of magnetic materials. 17*. North-Holland, Amsterdam [u.a, 1. edition, 2008. [cited on page 12]
- [35] Zhao, Zhang, Feng, Yang, and Huang. Nucleation or pinning: Dominant coercivity mechanism in exchange-coupled permanent/composite magnets. *Computational Materials Science*, 44(1):122–126, 2008. [cited on page 12]
- [36] Aharoni. Reduction in Coercive Force Caused by a Certain Type of Imperfection. *Physical Review*, 119(1):127–131, 1960. [cited on page 12]
- [37] Aharoni. *Introduction to the Theory of Ferromagnetism*. Oxford University Press, 2000. [cited on page 12]
- [38] Koch. *Handbook on Synchrotron Radiation*. North Holland, 1983. [cited on page 15]
- [39] De Groot and Kotani. *Core Level Spectroscopy of Solids*. Taylor & Francis Group, 2008. [cited on page 15]
- [40] Willmott. *An introduction to synchrotron radiation: techniques and applications*. John Wiley & Sons, 2019. [cited on pages 15 and 17]
- [41] Van Bokhoven and Lamberti. *X-Ray Absorption and X-Ray Emission Spectroscopy: Theory and Applications*. Wiley, 2016. [cited on page 15]
- [42] Bunker. *Introduction to XAFS: A Practical Guide to X-ray Absorption Fine Structure Spectroscopy*. Cambridge University Press, 2010. [cited on pages 15 and 17]

- [43] Sayers, Stern, and Lytle. New Technique for Investigating Noncrystalline Structures: Fourier Analysis of the Extended X-Ray—Absorption Fine Structure. *Physical Review Letters*, 27(18):1204–1207, 1971. [cited on page 17]
- [44] Fornasini, Monti, and Sanson. On the cumulant analysis of EXAFS in crystalline solids. *Journal of Synchrotron Radiation*, 8(6):1214–1220, 2001. [cited on page 18]
- [45] Rehr, Kas, Vila, Prange, and Jorissen. Parameter-free calculations of X-ray spectra with FEFF9. *Physical Chemistry Chemical Physics*, 12(21):5503–5513, 2010. [cited on pages 18 and 48]
- [46] Newville. IFEFFIT : interactive XAFS analysis and FEFF fitting. *Journal of Synchrotron Radiation*, 8(2):322–324, 2001. [cited on page 18]
- [47] Newville. Larch: An Analysis Package for XAFS and Related Spectroscopies. *Journal of Physics: Conference Series*, 430(1):012007, 2013. [cited on pages 18 and 48]
- [48] Erskine and Stern. Calculation of the M_{23} magneto-optical absorption spectrum of ferromagnetic nickel. *Physical Review B*, 12(11):5016–5024, 1975. [cited on page 19]
- [49] Schütz, Wagner, Wilhelm, Kienle, Zeller, Frahm, and Materlik. Absorption of circularly polarized x rays in iron. *Physical review letters*, 58(7):737, 1987. [cited on page 19]
- [50] Schütz. Spin Dependence of the Absorption of X-rays. *Physica Scripta*, 1989(T29):172, 1989. [cited on page 19]
- [51] Stöhr and Siegmann. *Magnetism*, volume 5 of *Solid-State Sciences*. Springer, Berlin, Heidelberg. 2006. [cited on page 20]
- [52] Thole, Carra, Sette, and Van Der Laan. X-ray circular dichroism as a probe of orbital magnetization. *Physical Review Letters*, 68(12):1943–1946, 1992. [cited on pages 21 and 87]
- [53] Carra, König, Thole, and Altarelli. Magnetic x-ray dichroism: General features of dipolar and quadrupolar spectra. *Physica B: Condensed Matter*, 192(1-2):182–190, 1993. [cited on pages 21 and 87]
- [54] Carra, Thole, Altarelli, and Wang. X-ray circular dichroism and local magnetic fields. *Phys Rev Lett*, 70(5):694–697, 1993. [cited on pages 21 and 87]
- [55] Chen, Idzerda, Lin, Smith, Meigs, Chaban, Ho, Pellegrin, and Sette. Experimental Confirmation of the X-Ray Magnetic Circular Dichroism Sum Rules for Iron and Cobalt. *Physical Review Letters*, 75(1):152–155, 1995. [cited on page 21]
- [56] Ankudinov and Rehr. Sum rules for polarization-dependent x-ray absorption. *Physical Review B*, 51(2):1282–1285, 1995. [cited on page 21]

-
- [57] Stöhr. Exploring the microscopic origin of magnetic anisotropies with X-ray magnetic circular dichroism (XMCD) spectroscopy. *Journal of Magnetism and Magnetic Materials*, 200(1):470–497, 1999. [cited on page 21]
- [58] Schütz, Goering, and Stoll. *Synchrotron Radiation Techniques Based on X-ray Magnetic Circular Dichroism*, volume 3. John Wiley and Sons, Ltd, 2007. [cited on page 21]
- [59] Van Der Laan. Sum rule practice. *Journal of Synchrotron Radiation*, 6(3):694–695, 1999. [cited on pages 21 and 40]
- [60] Vaz, Moutafis, Quitmann, and Raabe. Luminescence-based magnetic imaging with scanning x-ray transmission microscopy. *Applied Physics Letters*, 101(8):083114, 2012. [cited on page 21]
- [61] Kallmayer, Schneider, Jakob, Elmers, Balke, and Cramm. Interface magnetization of ultrathin epitaxial Co₂FeSi(110)/Al₂O₃films. *Journal of Physics D: Applied Physics*, 40(6):1552–1557, 2007. [cited on page 21]
- [62] Piamonteze, Windsor, Avula, Kirk, and Staub. Soft X-ray absorption of thin films detected using substrate luminescence: a performance analysis. *Journal of Synchrotron Radiation*, 27(5):1289–1296, 2020. [cited on page 21]
- [63] Elango. Hot holes in irradiated ionic solids. *Radiation Effects and Defects in Solids*, 128(1-2):1–13, 1994. [cited on page 22]
- [64] Vaz, Moutafis, Buzzi, and Raabe. X-ray excited optical luminescence of metal oxide single crystals. *Journal of Electron Spectroscopy and Related Phenomena*, 189:1–4, 2013. [cited on page 22]
- [65] Makhov, Lushchik, Lushchik, Kirm, Vasil’chenko, Vielhauer, Harutunyan, and Aleksanyan. Luminescence and radiation defects in electron-irradiated Al₂O₃ and Al₂O₃:Cr. *Nuclear Instruments and Methods in Physics Research Section B: Beam Interactions with Materials and Atoms*, 266(12):2949–2952, 2008. [cited on page 22]
- [66] Holler, Odstrcil, Guizar-Sicairos, Lebugle, Müller, Finizio, Tinti, David, Zusan, Unglaub, Bunk, Raabe, Levi, and Aeppli. Three-dimensional imaging of integrated circuits with macro- to nanoscale zoom. *Nature Electronics*, 2(10):464–470, 2019. [cited on page 22]
- [67] Holler, Odstrcil, Guizar-Sicairos, Lebugle, Frommherz, Lachat, Bunk, Raabe, and Aeppli. LamNI - an instrument for X-ray scanning microscopy in laminography geometry. *Journal of Synchrotron Radiation*, 27(3):730–736, 2020. [cited on pages 22 and 62]
- [68] Helfen, Myagotin, Mikulík, Pernot, Voropaev, Elyyan, Michiel, Baruchel, and Baumbach. On the implementation of computed laminography using synchrotron radiation. *Review of Scientific Instruments*, 82(6):063702, 2011. [cited on pages 22 and 24]

- [69] Witte, Späth, Finizio, Donnelly, Watts, Sarafimov, Odstrcil, Guizar-Sicairos, Holler, and Fink. From 2D STXM to 3D imaging: soft x-ray laminography of thin specimens. *Nano letters*, 20(2):1305–1314, 2020. [cited on pages 22 and 51]
- [70] Donnelly, Finizio, Gliga, Holler, Hrabec, Odstrčil, Mayr, Scagnoli, Heyderman, and Guizar-Sicairos. Time-resolved imaging of three-dimensional nanoscale magnetization dynamics. *Nature nanotechnology*, 15(5):356–360, 2020. [cited on pages 22 and 51]
- [71] Pfeiffer. X-ray ptychography. *Nature Photonics*, 12(1):9–17, 2018. [cited on pages 22 and 24]
- [72] Donnelly. *Hard X-ray Tomography of Three Dimensional Magnetic Structures*. Thesis, 2017. [cited on pages 22 and 62]
- [73] Rodenburg, Hurst, Cullis, Dobson, Pfeiffer, Bunk, David, Jefimovs, and Johnson. Hard-X-Ray Lensless Imaging of Extended Objects. *Physical Review Letters*, 98(3):034801, 2007. [cited on page 23]
- [74] Braun and Hauck. Tomographic reconstruction of vector fields. *IEEE Transactions on Signal Processing*, 39(2):464–471, 1991. [cited on pages 24 and 27]
- [75] Donnelly, Gliga, Scagnoli, Holler, Raabe, Heyderman, and Guizar-Sicairos. Tomographic reconstruction of a three-dimensional magnetization vector field. *New Journal of Physics*, 20(8):083009, 2018. [cited on pages 24 and 51]
- [76] Greg. X-ray computed tomography. *Physics Education*, 36(6):442, 2001. [cited on page 26]
- [77] Prince. Tomographic reconstruction of 3-d vector fields. In *1993 IEEE International Conference on Acoustics, Speech, and Signal Processing*, volume 5, pages 483–486 vol.5, prince93. [cited on page 27]
- [78] Prince. Tomographic reconstruction of 3-D vector fields using inner product probes. *IEEE Transactions on Image Processing*, 3(2):216–219, 1994. [cited on page 27]
- [79] Van Heel and Schatz. Fourier shell correlation threshold criteria. *Journal of Structural Biology*, 151(3):250–262, 2005. [cited on page 27]
- [80] Nieuwenhuizen, Lidke, Bates, Puig, Grünwald, Stallinga, and Rieger. Measuring image resolution in optical nanoscopy. *Nature Methods*, 10(6):557–562, 2013. [cited on page 27]
- [81] Sepehri-Amin, Thielsch, Fischbacher, Ohkubo, Schrefl, Gutfleisch, and Hono. Correlation of microchemistry of cell boundary phase and interface structure to the coercivity of $\text{Sm}(\text{Co}_{0.784}\text{Fe}_{0.100}\text{Cu}_{0.088}\text{Zr}_{0.028})_{7.19}$ sintered magnets. *Acta Materialia*, 126:1–10, 2017. [cited on page 29]
- [82] Strnat, Hoffer, Olson, Ostertag, and Becker. A Family of New Cobalt-Base Permanent Magnet Materials. *Journal of Applied Physics*, 38(3):1001–1002, 1967. [cited on page 29]

-
- [83] Strnat. *Chapter 2 Rare earth-cobalt permanent magnets*, volume 4, pages 131–209. Elsevier, 1988. [cited on page 29]
- [84] Gutfleisch, Willard, Brück, Chen, Sankar, and Liu. Magnetic materials and devices for the 21st century: stronger, lighter, and more energy efficient. *Advanced materials*, 23(7):821–842, 2011. [cited on page 29]
- [85] Sharma, Zintler, Günzing, Lill, Meira, Eilhardt, Singh, Xie, Gkouzia, Major, Radulov, Komissinskiy, Zhang, Skokov, Wende, Takahashi, Ollefs, Molina-Luna, and Alff. Epitaxy Induced Highly Ordered Sm₂Co₁₇–SmCo₅ Nanoscale Thin-Film Magnets. *ACS Applied Materials & Interfaces*, 13(27):32415–32423, 2021. [cited on pages 31, 34, 35, and 36]
- [86] Dhesi, Bencok, Brookes, Laan, and Galéra. X-ray magnetic circular dichroism study of SmAl₂ using the M_{4,5} x-ray absorption edges. *Journal of Applied Physics*, 93(10):8337–8339, 2003. [cited on page 31]
- [87] Heald. Optics upgrades at the APS beamline 20-BM. *Nuclear Instruments and Methods in Physics Research Section A: Accelerators, Spectrometers, Detectors and Associated Equipment*, 649(1):128–130, 2011. [cited on page 31]
- [88] Momma and Izumi. VESTA: a three-dimensional visualization system for electronic and structural analysis. *Journal of Applied Crystallography*, 41(3):653–658, 2008. [cited on page 32]
- [89] Ravel. Path degeneracy and EXAFS analysis of disordered materials. *J Synchrotron Radiat*, 21(Pt 6):1269–74, 2014. [cited on page 32]
- [90] Xu, Song, Lu, Seyring, and Rettenmayr. Nanoscale thermodynamic study on phase transformation in the nanocrystalline Sm₂Co₁₇ alloy. *Nanoscale*, 1(2):238–244, 2009. [cited on page 32]
- [91] Jennings and Chipman. High Temperature X-Ray Studies of SmCo₅. *AIP Conference Proceedings*, 18(1):1187–1191, 1974. [cited on page 32]
- [92] Kelly, Hesterberg, and Ravel. *Analysis of Soils and Minerals Using X-ray Absorption Spectroscopy*, pages 387–463. 2008. [cited on page 33]
- [93] Yan, Bollero, Gutfleisch, and Müller. Microstructure and magnetization reversal in nanocomposite SmCo₅/Sm₂Co₁₇ magnets. *Journal of Applied Physics*, 91(4):2192–2196, 2002. [cited on page 35]
- [94] Gkouzia, Günzing, Xie, Weßels, Kovács, N’diaye, Major, Palakkal, Dunin-Borkowski, Wende, Zhang, Ollefs, and Alff. Element-Specific Study of Magnetic Anisotropy and Hardening in SmCo₅–xCu_x Thin Films. *Inorganic Chemistry*, 2023. [cited on pages 35, 36, and 37]
- [95] Nukaga, Ohtake, Kirino, and Futamoto. Effects of Co/Sm Composition on the Ordered Phase Formation in Sm-Co Thin Films Grown on Cu (111) Single-Crystal Underlayers. *IEEE Transactions on Magnetics*, 44(11):2891–2894, 2008. [cited on page 35]

- [96] Ohtake, Nukaga, Kirino, and Futamoto. Epitaxial growth of Sm (Co, Cu) 5 thin film on Al₂O₃ (0 0 0 1) single-crystal substrate. *Journal of crystal growth*, 311(8):2251–2254, 2009. [cited on page 35]
- [97] Feng, Chen, Guo, Yu, and Li. Twinning structure in Sm(Co,Fe,Cu,Zr)_z permanent magnet. *Intermetallics*, 18(5):1067–1071, 2010. [cited on page 38]
- [98] Nachimuthu, Underwood, Kemp, Gullikson, Lindle, Shuh, and Perera. Performance Characteristics of Beamline 6.3.1 from 200 eV to 2000 eV at the Advanced Light Source. *AIP Conference Proceedings*, 705(1):454–457, 2004. [cited on page 38]
- [99] Günzing. Xaspy. <https://github.com/gnzng/xaspy>. [cited on page 38]
- [100] Coulthard, Freeland, Winarski, Ederer, Jiang, Inomata, Bader, and Callcott. Soft x-ray absorption of a buried SmCo film utilizing substrate fluorescence detection. *Applied physics letters*, 74(25):3806–3808, 1999. [Not cited.]
- [101] Itza-Ortiz, Ederer, Schuler, Ruzycki, Jiang, and Bader. Model study of soft x-ray spectroscopy techniques for observing magnetic circular dichroism in buried SmCo magnetic films. *Journal of Applied Physics*, 93(4):2002–2008, 2003. [Not cited.]
- [102] Lectard, Allibert, and Ballou. Saturation magnetization and anisotropy fields in the Sm(Co_{1-x}Cu_x)₅ phases. *Journal of Applied Physics*, 75(10):6277–6279, 1994. [cited on page 40]
- [103] Prados and Hadjipanayis. Sm(Co, Cu, Ni) thin films with giant coercivity. *Applied Physics Letters*, 74(3):430–432, 1999. [cited on page 40]
- [104] Cheng, Zhao, Cheng, and Miao. Magnetic moments in SmCo₅ and SmCo_{5-x}Cu_x films. *Journal of superconductivity and novel magnetism*, 25(6):1947–1950, 2012. [cited on page 40]
- [105] Cheng, Dai, Hu, Cheng, and Miao. Effect of Cu substitution on the magnetic properties of SmCo₅ film with perpendicular magnetic anisotropy. *Journal of electronic materials*, 41(8):2178–2183, 2012. [cited on page 40]
- [106] Teramura, Tanaka, Thole, and Jo. Effect of Coulomb Interaction on the X-Ray Magnetic Circular Dichroism Spin Sum Rule in Rare Earths. *Journal of the Physical Society of Japan*, 65:3056, 1996. [cited on pages 40 and 42]
- [107] Goedkoop, Brookes, Van Veenendaal, and Thole. Soft X-ray fluorescence yield XMCD sum rules. *Journal of Electron Spectroscopy and Related Phenomena*, 86(1):143–150, 1997. [cited on page 40]
- [108] Qiao, Kimura, Adachi, Kambe, Yoshikawa, Yaji, Hirai, Sato, Takeda, Namatame, Taniguchi, Tanaka, Muro, Imada, and Suga. Spin and orbital electronic states of Sm 4f electrons in (Sm, Gd)Al₂. *Physica B: Condensed Matter*, 351(3):333–337, 2004. [cited on page 40]

-
- [109] Piamonteze, Miedema, and De Groot. Accuracy of the spin sum rule in XMCD for the transition-metal L edges from manganese to copper. *Physical Review B*, 80(18):184410, 2009. [cited on pages 40 and 41]
- [110] Ueno, Hashimoto, Takeichi, and Ono. Quantitative magnetic-moment mapping of a permanent-magnet material by X-ray magnetic circular dichroism nano-spectroscopy. *AIP Advances*, 7(5):056804, 2017. [cited on page 40]
- [111] Kohlmann, Hansen, and Nassif. Magnetic Structure of SmCo₅ from 5 K to the Curie Temperature. *Inorganic Chemistry*, 57(4):1702–1704, 2018. [cited on page 42]
- [112] Patrick and Staunton. Temperature-dependent magnetocrystalline anisotropy of rare earth/transition metal permanent magnets from first principles: The light $R\text{Co}_5$ ($R = \text{Y, La-Gd}$) intermetallics. *Physical Review Materials*, 3(10):101401, 2019. [cited on page 42]
- [113] Samant, Stöhr, Parkin, Held, Hermsmeier, Herman, Van Schilfgaarde, Duda, Mancini, and Wassdahl. Induced spin polarization in Cu spacer layers in Co/Cu multilayers. *Physical review letters*, 72(7):1112, 1994. [cited on page 43]
- [114] Kukreja, Bonetti, Chen, Backes, Acremann, Katine, Kent, Dürr, Ohldag, and Stöhr. X-ray Detection of Transient Magnetic Moments Induced by a Spin Current in Cu. *Physical Review Letters*, 115(9):096601, 2015. [cited on page 43]
- [115] Haskin, Haskin, Frey, and Wildeman. *Relative and absolute terrestrial abundances of the rare earths*, pages 889–912. Elsevier, 1968. [cited on page 45]
- [116] Galler, Ener, Maccari, Dirba, Skokov, Gutfleisch, Biermann, and Pourovskii. Intrinsically weak magnetic anisotropy of cerium in potential hard-magnetic intermetallics. *npj Quantum Materials*, 6(1):2, 2021. [cited on page 45]
- [117] Bianconi, Marcelli, Dexpert, Karnatak, Kotani, Jo, and Petiau. Specific intermediate-valence state of insulating 4f compounds detected by L_3 x-ray absorption. *Physical Review B*, 35(2):806–812, 1987. [cited on page 45]
- [118] Soldatov, Ivanchenko, Della Longa, Kotani, Iwamoto, and Bianconi. Crystal-structure effects in the Ce L_3 -edge x-ray-absorption spectrum of CeO₂: Multiple-scattering resonances and many-body final states. *Physical Review B*, 50(8):5074–5080, 1994. [cited on page 45]
- [119] Xie and Zhang. Mixed valence nature of the Ce 4f state in CeCo₅ based on spin-polarized DFT+DMFT calculations. *Physical Review B*, 106(22):224411, 2022. [cited on page 45]
- [120] Neifeld, Croft, Mihalisin, Segre, Madigan, Torikachvili, Maple, and Delong. Chemical environment and Ce valence: Global trends in transition-metal compounds. *Physical Review B*, 32(10):6928–6931, 1985. [cited on pages 45 and 46]
- [121] Wohlleben and Röhler. The valence of cerium in metals (invited). *Journal of Applied Physics*, 55(6):1904–1909, 1984. [cited on page 45]

- [122] Nordström, Eriksson, Brooks, and Johansson. Theory of ferromagnetism in CeCo₅. *Physical Review B*, 41(13):9111–9120, 1990. [cited on page 45]
- [123] Kappler, Herr, Schmerber, Derory, Parlebas, Jaouen, Wilhelm, and Rogalev. Low-temperature properties of the Ce(Pd_{1-x}Ni_x)₃ system. *European Physical Journal B - EUR PHYS J B*, 37:163–167, 2004. [cited on page 45]
- [124] Wang, Liang, Zhang, Yano, Terashima, Kada, Kato, Kadono, Imada, Nakamura, and Hirano. Mixed-valence state of Ce and its individual atomic moments in Ce₂Fe₁₄B studied by soft X-ray magnetic circular dichroism. *Intermetallics*, 69:42–46, 2016. [cited on page 45]
- [125] Giorgetti, Pizzini, Dartyge, Fontaine, Baudalet, Brouder, Bauer, Krill, Miraglia, Fruchart, and Kappler. Magnetic circular x-ray dichroism in Ce intermetallic compounds. *Physical Review B*, 48(17):12732–12742, 1993. [cited on page 46]
- [126] Kachel. The PM3 beamline at BESSY II. *Journal of large-scale research facilities JLSRF*, 2:A48–A48, 2016. [cited on page 46]
- [127] Heald, Cross, Brewes, and Gordon. The PNC/XOR X-ray microprobe station at APS sector 20. *Nuclear Instruments and Methods in Physics Research Section A: Accelerators, Spectrometers, Detectors and Associated Equipment*, 582(1):215–217, 2007. [cited on page 46]
- [128] Lu, Höppner, Gunnarsson, and Haverkort. Efficient real-frequency solver for dynamical mean-field theory. *Physical Review B*, 90(8):085102, 2014. [cited on page 46]
- [129] Paidi, Brewes, Freeland, Roberts, and Van Lierop. Role of Ce 4*f* hybridization in the origin of magnetism in nanoceria. *Physical Review B*, 99(18):180403, 2019. [cited on page 46]
- [130] Alam and Johnson. Mixed valency and site-preference chemistry for cerium and its compounds: A predictive density-functional theory study. *Physical Review B*, 89(23):235126, 2014. [cited on page 47]
- [131] Scheinost, Claussner, Exner, Feig, Findeisen, Hennig, Kvashnina, Naudet, Prieur, Rossberg, Schmidt, Qiu, Colomp, Cohen, Dettona, Dyadkin, and Stumpf. ROBL-II at ESRF: a synchrotron toolbox for actinide research. *Journal of Synchrotron Radiation*, 28(1):333–349, 2021. [cited on page 49]
- [132] Kvashnina, Butorin, and Glatzel. Direct study of the f-electron configuration in lanthanide systems. *Journal of Analytical Atomic Spectrometry*, 26(6):1265–1272, 2011. [cited on page 50]
- [133] Folks, Street, and Woodward. Domain structures of die-upset melt-spun Nd-FeB. *Applied Physics Letters*, 65(7):910–912, 1994. [cited on pages 51 and 53]
- [134] Crew, McCormick, and Street. An investigation of reversible magnetization in NdFeB. *Journal of Applied Physics*, 86(6):3278–3284, 1999. [cited on pages 51 and 53]

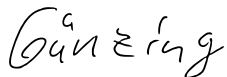
-
- [135] Crew, Lewis, and Panchanathan. Multiscale magnetic domains observed in die-upset melt-spun magnets using magnetic force microscopy. *Journal of Magnetism and Magnetic Materials*, 231(1):57–64, 2001. [cited on pages 51 and 53]
- [136] Craik and Isaac. Magnetic Interaction Domains. *Proceedings of the Physical Society*, 76(1):160–162, 1960. [cited on pages 51 and 53]
- [137] Khlopkov, Gutfleisch, Hinz, Müller, and Schultz. Evolution of interaction domains in textured fine-grained Nd₂Fe₁₄B magnets. *Journal of Applied Physics*, 102(2):023912, 2007. [cited on pages 51 and 54]
- [138] Khlopkov, Gutfleisch, Schäfer, Hinz, Müller, and Schultz. Interaction domains in die-upset NdFeB magnets in dependence on the degree of deformation. *Journal of Magnetism and Magnetic Materials*, 272:E1937–E1939, 2004. [cited on pages 51, 53, and 59]
- [139] Woodcock, Khlopkov, Walther, Dempsey, Givord, Schultz, and Gutfleisch. Interaction domains in high-performance NdFeB thick films. *Scripta Materialia*, 60(9):826–829, 2009. [cited on pages 51 and 54]
- [140] Thielsch, Stopfel, Wolff, Neu, Woodcock, Güth, Schultz, and Gutfleisch. In situ magnetic force microscope studies of magnetization reversal of interaction domains in hot deformed Nd-Fe-B magnets. *Journal of Applied Physics*, 111(10):103901, 2012. [cited on pages 51, 54, 66, 68, and 73]
- [141] Hioki. High performance hot-deformed Nd-Fe-B magnets (Review). *Science and Technology of Advanced Materials*, 22(1):72–84, 2021. [cited on pages 51, 55, and 60]
- [142] Gutfleisch, Müller, Khlopkov, Wolf, Yan, Schäfer, Gemming, and Schultz. Evolution of magnetic domain structures and coercivity in high-performance SmCo_{2:17}-type permanent magnets. *Acta Materialia*, 54(4):997–1008, 2006. [cited on page 51]
- [143] Ono, Araki, Yano, Miyamoto, Shoji, Kato, Manabe, Nozaki, Kaneko, and Raabe. Element-Specific Magnetic Domain Imaging of (Nd, Dy)-Fe-B Sintered Magnets Using Scanning Transmission X-Ray Microscopy. *IEEE Transactions on Magnetics*, 47(10):2672–2675, 2011. [cited on page 51]
- [144] Suzuki, Yasui, Kotani, Tsuji, Nakamura, and Hirosawa. Magnetic domain evolution in Nd-Fe-B:Cu sintered magnet visualized by scanning hard X-ray microprobe. *Acta Materialia*, 106:155–161, 2016. [cited on page 51]
- [145] Billington, Toyoki, Okazaki, Kotani, Fukagawa, Nishiuchi, Hirosawa, and Nakamura. Unmasking the interior magnetic domain structure and evolution in Nd-Fe-B sintered magnets through high-field magnetic imaging of the fractured surface. *Physical Review Materials*, 2(10):104413, 2018. [cited on page 51]

- [146] Donnelly, Guizar-Sicairos, Scagnoli, Holler, Huthwelker, Menzel, Vartiainen, Muller, Kirk, Gliga, Raabe, and Heyderman. Element-specific X-ray phase tomography of 3D structures at the nanoscale. *Phys Rev Lett*, 114(11):115501, 2015. [cited on page 51]
- [147] Donnelly, Scagnoli, Guizar-Sicairos, Holler, Wilhelm, Guillou, Rogalev, Detlefs, Menzel, Raabe, and Heyderman. High-resolution hard x-ray magnetic imaging with dichroic ptychography. *Physical Review B*, 94(6):064421, 2016. [cited on page 51]
- [148] Donnelly, Guizar-Sicairos, Scagnoli, Gliga, Holler, Raabe, and Heyderman. Three-dimensional magnetization structures revealed with X-ray vector nanotomography. *Nature*, 547(7663):328–331, 2017. [cited on page 51]
- [149] Rana, Liao, Iacocca, Zou, Pham, Lu, Subramanian, Lo, Ryan, Bevis, Karl, Glead, Rable, Mahale, Hirst, Ostler, Liu, O’leary, Yu, Bustillo, Ohldag, Shapiro, Yazdi, Mallouk, Osher, Kapteyn, Crespi, Badding, Tserkovnyak, Murnane, and Miao. Three-dimensional topological magnetic monopoles and their interactions in a ferromagnetic meta-lattice. *Nature Nanotechnology*, 18(3):227–232, 2023. [cited on page 51]
- [150] Suzuki, Yumoto, Koyama, Yamazaki, Takeuchi, Kawamura, Mizumaki, Osawa, Kondo, Ariake, Yasui, Kotani, Tsuji, Nakamura, Hirosawa, Yamada, Kim, Kim, Ishibashi, Ono, and Ohashi. Magnetic Microscopy Using a Circularly Polarized Hard-X-ray Nanoprobe at SPring-8. *Synchrotron Radiation News*, 33(2):4–11, 2020. [cited on pages 52 and 73]
- [151] Takeuchi, Suzuki, Kobayashi, Kotani, Nakamura, Kikuchi, Bolyachkin, Sepehri-Amin, Ohkubo, Hono, Une, and Okamoto. Real picture of magnetic domain dynamics along the magnetic hysteresis curve inside an advanced permanent magnet. *NPG Asia Materials*, 14(1):70, 2022. [cited on page 52]
- [152] Skomski and Coey. *Permanent magnetism*. Studies in condensed matter physics. Inst. of Physics Publ., Bristol [u.a, 1999. [cited on page 52]
- [153] Givord, Li, and Moreau. Magnetic properties and crystal structure of Nd₂Fe₁₄B. *Solid State Communications*, 50(6):497–499, 1984. [cited on page 52]
- [154] Menushenkov, Ivanov, Shchetinin, Zhukov, Menushenkov, Rudnev, Ivanov, Wilhelm, Rogalev, and Savchenko. XMCD study of the local magnetic and structural properties of microcrystalline NdFeB-based alloys. *JETP letters*, 105(1):38–42, 2017. [cited on pages 53, 63, and 74]
- [155] Jiang, Pearson, Liu, Kabius, Trasobares, Miller, Bader, Lee, Haskel, Srajer, and Liu. A new approach for improving exchange-spring magnets. *Journal of Applied Physics*, 97(10):10K311, 2005. [cited on page 54]
- [156] Newnham, Jakubovics, and Daykin. Domain structure of thin NdFeB foils. *Journal of Magnetism and Magnetic Materials*, 157-158:39–40, 1996. [cited on page 54]

-
- [157] Lloyd, Loudon, and Midgley. Measurement of magnetic domain wall width using energy-filtered Fresnel images. *Journal of Microscopy*, 207(2):118–128, 2002. [cited on page 54]
- [158] Gutfleisch. Controlling the properties of high energy density permanent magnetic materials by different processing routes. *Journal of Physics D: Applied Physics*, 33(17):R157, 2000. [cited on page 57]
- [159] Hasenkamp. Radiographic laminography. Report, 1973-11-01 1973. [cited on page 61]
- [160] Helfen, Baumbach, Mikulík, Kiel, Pernot, Cloetens, and Baruchel. High-resolution three-dimensional imaging of flat objects by synchrotron-radiation computed laminography. *Applied Physics Letters*, 86(7):071915, 2005. [cited on page 61]
- [161] Helfen, Baumbach, Cloetens, and Baruchel. Phase-contrast and holographic computed laminography. *Applied Physics Letters*, 94(10):104103, 2009. [cited on page 61]
- [162] Scagnoli, Mazzoli, Detlefs, Bernard, Fondacaro, Paolasini, Fabrizi, and De Bergevin. Linear polarization scans for resonant X-ray diffraction with a double-phase-plate configuration. *Journal of Synchrotron Radiation*, 16(6):778–787, 2009. [cited on page 62]
- [163] Guizar-Sicairos and Thibault. Ptychography: A solution to the phase problem. *Physics Today*, 74(9):42–48, 2021. [cited on page 64]
- [164] Thibault, Dierolf, Menzel, Bunk, David, and Pfeiffer. High-Resolution Scanning X-ray Diffraction Microscopy. *Science*, 321(5887):379–382, 2008. [cited on page 64]
- [165] Thibault and Guizar-Sicairos. Maximum-likelihood refinement for coherent diffractive imaging. *New Journal of Physics*, 14(6):063004, 2012. [cited on page 64]
- [166] Wakonig, Stadler, Odstreil, Tsai, Diaz, Holler, Usov, Raabe, Menzel, and Guizar-Sicairos. PtychoShelves, a versatile high-level framework for high-performance analysis of ptychographic data This article will form part of a virtual special issue of the journal on ptychography software and technical developments. *Journal of Applied Crystallography*, 53(2):574–586, 2020. [cited on page 64]
- [167] Klassen. Masters thesis: 3D-imaging of the magnetic structure of a Nd-Fe-B bulk magnet. *Universität Duisburg-Essen*, 2023. [cited on page 67]
- [168] Givord, Li, and Tasset. Polarized neutron study of the compounds Y₂Fe₁₄B and Nd₂Fe₁₄B. *Journal of Applied Physics*, 57(8):4100–4102, 1985. [cited on page 74]
- [169] Haskel, Lang, Islam, Cady, Srajer, Van Veenendaal, and Canfield. Atomic Origin of Magnetocrystalline Anisotropy in Nd₂Fe₁₄B. *Physical Review Letters*, 95(21):217207, 2005. [cited on page 74]

Selbständigkeitserklärung

Hiermit versichere ich, dass ich diese Arbeit selbständig verfasst, keine anderen als die angegebenen Quellen und Hilfsmittel benutzt, sowie Zitate kenntlich gemacht habe.



Duisburg, den December 20, 2023

Damian Günzing

DuEPublico

Duisburg-Essen Publications online

UNIVERSITÄT
DUISBURG
ESSEN

Offen im Denken

ub | universitäts
bibliothek

Diese Dissertation wird via DuEPublico, dem Dokumenten- und Publikationsserver der Universität Duisburg-Essen, zur Verfügung gestellt und liegt auch als Print-Version vor.

DOI: 10.17185/duepublico/81384

URN: urn:nbn:de:hbz:465-20240112-080250-7

Alle Rechte vorbehalten.